TRANSFORMATION OF WAVE ENERGY ACROSS THE FRINGING REEF OF IPAN, GUAM

A DISSERTATION SUBMITTED TO
THE GRADUATE DIVISION OF THE UNIVERSITY OF HAWAI‘I AT MĀNOA IN PARTIAL FULFILLMENT OF THE REQUIREMENTS FOR THE DEGREE OF

DOCTOR OF PHILOSOPHY

IN

OCEANOGRAPHY

AUGUST 2012

By
Anne-Christine Péquignet

Dissertation Committee:

Janet M. Becker, Chairperson
Mark A. Merrifield
Douglas S. Luther
Eugene R. Pawlak
Charles H. Fletcher III

Acknowledgements

First I would like to thank Mark Merrifield for giving me the opportunity to conduct this PhD. I appreciate both the direction and the independence that Mark gave me to conduct my research and build my career. I would like to thank Janet Becker for the time and effort she has invested in me. I hope my writing has improved thanks to the countless hours of careful reading that Janet had to go through. I thank Geno Pawlak for helpful comments and questions and forcing me to see my research in different ways. I was very privileged to have Doug Luther in my committee and although I did not nearly tap into Doug's vast knowledge as much as I should have, I feel that often, just having Doug in my committee made me be more careful with my research and answer questions that I thought Doug were going to ask.

My gratitude is also extended to Neil Frazer and Charles (Chip) Fletcher who both served as external members of my committee. Neil often modestly down played the role he had in my committee, but I politely disagree with you Neil, and instead I think you provided me with the help and support that an external member should provide, when I needed it. I fully appreciated your diverse scientific knowledge and your experience as an educator. Chip's enthusiasm for my research at various stages of my degree was very encouraging and I am grateful for his participation in my dissertation defence at a less than convenient time.

This work was very much a group effort, and I would like to thank my lab and field mates (Chris Kontoes, Oliver Vetter, Yvonne Firing, Jerome Aucan, Kimball Millikan, Tyson Hilmer, Carly Quisenberry, Allan Fetherhoff, Paul Lethaby, Bryan Rahter, Jeanette Clark, Anna Merrifield, and Derek Young) for their help and cheerful enthusiasm. The staff at the Marine Lab of the University of Guam was instrumental in the collection of the data used in this work, in particular Jason Miller and Suzanne Wilkins.

The present work would not have been the same without my past experience at Dalhousie University and from my time in Halifax, I would like to thank Drs Bowen, Thomson, Hay, Karin Bryan, Phil Macaulay and David Walsh. Here at UH, I was fortunate to have had many insightful discussions with Volker Roeber, Assaf Azouri, Marion Chavanne and Jerome Aucan. Ryan Lowe from the U. of Western Australia kept me motivated through the end of my degree with the prospect of a job and new exciting research, I am very grateful for his encouragement and confidence in me. Many thanks to the administrative staff in the oceanography department in particular to Nancy Koike and Kristin Uyemura Momohara for their help in keeping up with the UH forms, requirements and deadlines.

During this PhD program, I became a mother, and in the process of learning to be a working mother, I had the support and examples of many of the SOEST mothers, and in particular I would like to acknowledge the compassion of Marion Chavanne, Laurie Menviel, Benedicte Doucet and Kathleen Ruttenberg. I have received a lot of help, support, encouragement and entertainment from my family and friends. Without them, my PhD years would have been pretty unpleasant. In particular I would like to thank Hank and Jean, Alli, Rachel, Jackie, Paulo, Laurie, Matthieu, Marcia, Vanessa, Lyndsey, Audrey. My quest for this degree was a selfish endeavor and I need to thank and apologize to my parents, husband Paul and daughter Maile for all the sacrifices I asked from them. I hope I will make all these efforts worthwhile.

The research for this dissertation was supported by the US Army Corps of Engineers, and salary was also provided by the University of Hawaii Sea Grant program.

Abstract

Measurements from a cross-shore array of pressure sensors and current-meters, deployed on the fringing reef of Ipan, Guam as part of the PILOT (Pacific Island Land-Ocean Typhoon) experiment, were analyzed to understand the processes driving the large water level oscillations observed at the shore during energetic wave events. Offshore, sea and swell (SS: 3 to 20 seconds period) energy is dominant, while on the reef flat, energetic oscillations are observed with periods in the infragravity (IG: 20 to 200 seconds) and far infragravity (fIG 200 to 1000 seconds) bands. The nonlinear processes that contribute to this low-pass transformation of wave energy across the reef are analyzed in terms of the energetics of the wave field in each frequency band. Wave transformation across the fringing reef is characterized by the strong breaking and dissipation of the incident SS energy which provides a driving force for the waves at lower frequencies. The SS energy on the reef flat is shown to be strongly dependent on the total reef flat water level that includes wave induced setup. The non linear transfer of energy between the SS and low frequency (LF: IG and fIG) bands is responsible for both the forcing and the loss of low frequency energy at the reef crest. In IG band, the low frequency oscillations resulting from the breaking SS envelope work against the incident bound waves and energy is transferred to the SS band similar to the nonlinear transfer observed on sandy beaches. The SS envelope oscillations at fIG frequencies force free fIG waves across the surfzone. Across the reef flat, low frequency oscillations at normal mode frequencies are preferentially excited. The development of standing waves on the reef flat is controlled

by the strong depth dependent frictional dissipation of the LF waves reflected at the shoreline. During tropical storm Man-Yi, resonant standing modes in the fIG band were excited when a large increase in water level over the reef occurred due to wave setup that both reduced the effects of friction and the period of the fundamental mode.

Table of contents

Chapter 3

Chapter 4

Chapter 5

List of Figures

Chapter 1

Chapter 2

Chapter 3

Chapter 4

.

List of tables

Chapter 2

Chapter 1

Introduction

1.1 Background

1.1.1 General context

With more than 40% of the world population (more than 50% in the US) living in coastal areas (Martinez *et al*. 2007) along with a general trend for an increase in coastal populations, the environmental issues faced by coastal areas are becoming increasingly important (Duxbury and Dickinson 2007). The range of spatial and temporal scales of processes observed in the oceans also is observed in coastal areas where the seas or oceans meet the land. Long period waves such as Rossby waves or tidal oscillations are important at scales of oceans basins or continental shelves, but for the dynamics of short waves considered in the littoral zone they represent a slowly varying sea level and slowly varying currents. In the shallow waters of the nearshore zone, shorter waves such as tsunami or ocean swell usually experience significant transformation and dissipation (Figure 1.1). Wave action may significantly affect nearshore morphology.

1.1.2 Nearshore dynamics

A typical spectrum of wave energy in the nearshore is composed of a large peak at periods typically ranging from 3 to 20s from wind generated waves: sea and swell energy

(SS: 0.05 to 0.3 Hz) (Fig. 1.2). Sea and swell peaks often are distinct and seas, that tend to be locally generated, have a broad peak of higher frequencies while swells that are generated remotely and are well sorted have a narrower peak with lower frequencies. The frequency band below the wind wave band and above the tides is called infragravity (IG: 0.005 to 0.05 Hz) and usually is observed to be much less energetic than the SS band in deep water (Elgar *et al*. 1992), but becomes significant in shallow water where SS energy is rapidly dissipated (e.g. Guza and Thornton 1985, Ruessink 1998a, van Dongeren *et al*. 2007). Because energy in this frequency band typically is highly correlated with swell energy (Elgar *et al*. 1992) and is associated with the SS group structure, this IG energy was initially named "surf beat" (Munk 1949, Tucker 1950). Weak non-linear interactions among SS waves force low frequency oscillations with difference frequencies that fall in the IG band and are out of phase with the wave group (Hasselmann 1962, Longuet-Higgins and Stewart 1962). The resulting second-order bound waves may be released when the SS waves break and propagate as free waves. Part of the free infragravity energy observed in the nearshore does not appear to originate from bound waves (Herbers *et al*. 1995) and this is particularly true for the very low part of the IG band sometimes referred to as far IG (fIG: 0.001 to 0.005 Hz). Some alongshore propagating oscillations in this frequency band have been identified as shear waves, or shear instability of the longshore currents (Oltman-Shay *et al*. 1989). Suggestions have been made that free IG waves may result from seaward propagating low frequency oscillations generated by variable breakpoint forcing (Symonds *et al*. 1982, Ruessink 1998b). The transformation of waves in the nearshore strongly depends on frequency. As waves enter shallow water, SS waves shoal to an unstable wave height at which point

they break and most of their energy is dissipated. In contrast, long IG waves typically are not steep enough to break and significant IG energy reaches the shore.

In the nearshore, the momentum due to wave motion drives the circulation. The excess momentum flux resulting from the breaking of SS waves forces a steady elevation of the sea level shoreward of the breakpoint called setup (Bowen *et al*. 1968, Guza and Thornton 1981). The shoreward mass transport of water is balanced by a seaward return flow, which may take the form of a diffuse undertow, or narrow cross-shore jets called rip currents (Bowen 1969). The oblique incidence of SS waves is responsible for a net flux of momentum along the shore, which drives the longshore currents that are responsible for significant transport of sediment along sandy beaches (Inman and Bagnold 1963).

1.1.3 Reef hydrodynamics

In recent years, after events such as Hurricane Katrina in 2005, efforts have been made to understand wave transformation on substrates other than sand such as mud (e. g., Elgar and Raubenheimer 2008, Sheremet *et al*. 2011), or through vegetation (e.g. Mei *et al*. 2011, Riffe *et al*. 2011, Suzuki *et al*. 2012) but to date, a large part of the work on wave transformation has focused on unconsolidated environments. This is in part due to the motivation for managing sediment transport and shoreline protection. Historically, shoreline protection strategies often have involved solid structures such as jetties, groins and breakwaters (Pilkey and Dixon 1996). Following this practice, reefs offer a natural

and efficient defense against ocean waves (Munk and Sargent 1954) and studies of wave transformation over reefs often have focused on understanding the circulation in reef systems (e.g. Gourlay and Colleter 2005, Symonds *et al*. 1995, Taebi *et al*. 2011) and its importance for coral colonies (e.g. Atkinson and Bilger 1992, Falter *et al*. 2004). Although coral reefs are only one of the many types of reefs (e.g. rocky reefs, temperate shore platforms, stromatolite reef), the present discussion will focus on coral reefs as they are the dominant type of reef in the tropics and on tropical islands in particular. However several dynamical concepts related to coral reefs may also apply to other types of reefs (Symonds *et al*. 2011). The increasing vulnerability of low lying island nations to rising sea level (Minura 1999) now is motivating a better understanding of the processes that result in inundation of reef-fringed shorelines.

Reefs are different from sandy shores in many ways and accordingly we expect wave transformations to differ. Sandy shores tend to have smooth topographies that can be characterized by a small range of beach slopes, and possibly the presence of sand bars. Reefs often have a large range of slopes with steep fore reefs and near flat sections of lagoon or reef flat. The range of bottom slopes also is coupled with a variety of substrates, with different reef builders occupying areas with a range of energy levels and in turn contributing differently to the transformations of waves. The roughness of corals and reef builders in general is larger than unconsolidated sediments (Nelson 1996, Nunes et Pawlak 2008, Jaramillo and Pawlak 2011) and results in a large range of values of friction factors on reefs (Rosman and Hench 2011), up to 100 times the values observed for sandy shores.

Sandy beaches adjust to changing conditions with cross-shore and longshore sediment transport (e.g. Bruun 1954, Dean 1977 and 1990, Greenwood and Mittler 1984) over time scales of days to years. Reefs instead, result from the long time scale equilibrium between the physical forcing (sea level, waves energy, nutrients input, light, temperature) and the biological activity of the reef builders (Munk and Sargent 1954, Kennedy and Woodroffe 2002, Storlazzi *et al*. 2003, Storlazzi *et al*. 2005, Kench and Brander 2006). The distribution of reef builders across a reef is directly linked to the hydrodynamics (Hearn *et al*. 2001, Storlazzi *et al*. 2005, Madin and Connolly 2006) and the topography of a given reef represents the equilibrium with the prevailing wave conditions.

In recent years, due to both technological advances of sensors and increasing interest in reef hydrodynamics, more laboratory and field hydrodynamic data have been collected (Hearn 2011) in an effort to better understand physical processes on reefs. Hydrodynamics of coral reefs involve flows at scales ranging from the size of an individual coral colony (e.g. Falter *et al*. 2005, Monismith 2007, Lowe *et al*. 2007) to the size of atolls (Wolanski and Bennett 1983). This dissertation is concerned with waves at scales of tens to thousands of meters. The general understanding of wave-driven flow on reefs is that SS waves break at the reef crest and the gradient of wave momentum flux through the breaking zone forces water onto the reef flat. This-wave driven setup (Bowen *et al*. 1968, Gourlay 1996a, b, Vetter *et al*. 2010) forces flow across or along the reef (Symonds *et al*. 1995, Gourlay and Colleter 2006, Hearn 1999). As pointed out by Sheremet *et al*. (2011), the transformation of waves on reefs is similar to that on beaches but the localization and the intensity of the processes are different. Reefs tend to have a

strongly localized and narrow surf zone. The transformation of waves from deep to shallow water typically occurs over a limited horizontal extent for reefs and this results in large shoaling and dissipation rates. With waves breaking often far from the shore, the swash zone of a reef environment may be less energetic than the sandy shore equivalent. However, similar to the sandy shore swash zone, reef flats and reef-fringed shorelines often are dominated by low frequency oscillations (Nakaza and Hino 1988, Lugo-Fernandez *et al*. 1998), which are the focus of this dissertation.

1.1.4 Open questions

The forcing and dissipation of low frequency oscillations in the nearshore in general are still not well understood. In particular, the work of Henderson *et al*. (2006) and Thomson *et al*. (2006) have highlighted how the nonlinear processes responsible for the forcing of IG waves also may be responsible for the loss of low frequency energy in the surfzone. On reefs, understanding the low frequency oscillations that dominate most reef flats also requires a better understanding of the transformation of the short waves that provide the driving force particularly during large wave events when very few observations are available. Because reefs evolve from the balance between coral growth and the physical forcing of the prevailing wave conditions (Storlazzi *et al*. 2003) they may not dissipate wave energy during extreme conditions observed during storms or cyclones as efficiently as during prevailing conditions. Technological advances of the last decade have helped capture the complex topography of reefs and high resolution bathymetric data now are available for numerical models of reef hydrodynamics (Hearn 2011). The highly

nonlinear physics involved in the transformation of wave on reefs still is not well understood and numerical models are often validated using simplified laboratory data (Demirbilek and Nwogu 2007, Sheremet *et al*. 2011).

The Pacific Islands Land-Ocean Typhoon Experiment (PILOT) was aimed at better defining the physics of coastal inundation and flooding along reef fringed island shorelines due to storm waves and elevated sea levels associated with typhoons. This dissertation presents the field observations collected in an effort to improve the ability to predict the effects of these processes. This work presents the Guam deployment of this project. Guam was chosen for the typical moderate trade wind wave climate with the occasional typhoon (Chan and Shi 1996) wave conditions (Figure 1.3). In comparison Hawaiian reefs are subject to more energetic winter swell conditions than Guam.

1.2 Purpose and outline of dissertation

The purpose of this dissertation is to present field measurements of wave energy across a fringing reef during large wave conditions, and analyze these data to understand and quantify the processes involved in the transformation of wave energy across Ipan reef, Guam. The specific goals are to describe the spectral distribution of wave energy and quantify the fluxes of wave energy across the reef. The source of the low frequency oscillations will be assessed, and the processes involved in the dissipation of sea and

swell and infragravity energy will be identified and quantified. Finally the amount of energy reaching the shore will be related to incident wave conditions.

In chapter 2, this dissertation first explores the dissipation across the reef of the energy that dominates the incoming offshore spectrum: sea and swell (SS). As SS energy is dissipated across the reef, the low frequency energy becomes dominant on the reef flat. In particular, during the largest event observed in Ipan, energetic oscillations at fIG frequencies were recorded and are described in chapter 3. The mechanisms of forcing and dissipation of the low frequency energy then are detailed for a number of large wave events in Chapter 4. After a brief summary of this work, general conclusions are drawn and perspectives for future work are presented.

Each chapter of the thesis represents a stand-alone article that has been published in a peer-reviewed journal (chapter 2 and 3), or that is in preparation for submission (chapter 4). Co-authors contributed to these articles; however, I am the lead author on each paper and am primarily responsible for their intellectual content.

References

Atkinson M. J., R. W. Bilger (1992), Effects of Water Velocity on Phosphate-Uptake in Coral Reef-Flat Communities. *Limnol. Oceanogr.* 37: 273-9

Bowen A. J., D. L. Inman, V. P. Simmons (1968), Wave set-down and wave set-up, *J. Geophys. Res.* 73(8):2569-2577.

Bowen A. J. (1969), Rip Currents 1. Theoretical Investigations, *J. Geophys. Res.* 74, (23): 5467-5478, doi:10.1029/JC074i023p05467.

Bruun, P. (1954), Coast Erosion and the Development of beach profiles. Technical Memorandum No. 44, Beach Erosion Board, US Army Corps of Engineers.

Chan, J. C. L., and J. Shi (1996), Long-term trends and interannual variability in tropical cyclone activity over the western North Pacific, *Geophys. Res. Lett.*, 23(20), 2765–2767, doi:10.1029/96GL02637.

Dean, R.G. (1977), Equilibrium beach profiles: US Atlantic and Gulf coasts, Department of Civil Engineering, Ocean Engineering Report No. 12, University of Delaware, Newark, DE.

Dean, R.G. (1990), Equilibrium beach profiles: characteristics and applications. Report UFL/COEL-90/001, Coastal and Oceanographic Department, University of Florida, Gainesville, FL.

Duxbury J. and S. Dickinson (2007), Principles for sustainable governance of the coastal zone: In the context of coastal disasters, Ecological Economics 63(2-3), 319-330.

Elgar S., T. H. C. Herbers, M. Okihiro, J. Oltman-Shay, and R. T. Guza. (1992) Observations of infragravity waves, *J. Geophys. Res*., 97(C10), 15573– 15577.

Elgar S,. and B. Raubenheimer (2008), Wave dissipation by muddy seafloors, *Geophys. Res. Let.* 35(7), L07611 doi: 10.1029/2008GL033245.

Falter J. L., M. J. Atkinson, and M. A. Merrifield (2004), Mass-transfer limitation of nutrient uptake by a wave-dominated reef flat community, *Limnol. Oceanogr.* 49, 1820-31.

Gourlay M. R. (1996a), Wave set-up on coral reefs.1. Set-up and wave generated flow on an idealized two dimensional horizontal reef, *Coast. Eng.* 27(3-4),161–193.

Gourlay M. R. (1996b), Wave set-up on coral reefs. 2. Set-up on reefs with various profiles. *Coast. Eng.* 28(1-4), 17–55.

Gourlay M.R., and G. Colleter (2005), Wave-generated flow on coral reefs analysis for two-dimensional horizontal reef-tops with steep faces. *Coast. Eng* 52(4), 353–387.

Greenwood B. and P.R. Mittler (1984), Sediment flux and equilibrium slopes in a barred nearshore. *Mar. Geol*., 60, 79-98.

Guza R.T. and E. B. Thornton (1985), Observations of surf beat, *J. Geophys. Res*.,90 (C2) 3161-3172 DOI: 10.1029/JC090iC02p03161.

Guza R. T., and E. Thornton (1981), Wave Set Up on a Natural Beach, *J. Geophys. Res*., 86, C5, doi:10.1029/JC086iC05p04133.

Hardisty J. (1986), A morphodynamic model for beach gradients. *Earth Surface Processes and Landforms*, 11, 327-333.

Hasselmann K. (1962), On the non-linear energy transfer in a gravity-wave spectrum, 1, general theory. *J. Fluid Mech*., 12, 481–500.

Hearn C. J. (2011), Perspectives in coral reef hydrodynamics. *Coral Reefs*, 30(1), 1-9, doi: 10.1007/s00338-011-0752-4.

Hearn CJ; M. J. Atkinson and J. L. Falter (2001), A physical derivation of nutrient-uptake rates in coral reefs: effects of roughness and waves, Coral Reefs, 20(4), 347-356.

Henderson S. M., R. T. Guza, S. Elgar, T. H. C. Herbers, and A. J. Bowen (2006), Nonlinear generation and loss of infragravity wave energy, *J. Geophys. Res.*, 111(C12007).

Herbers T. H. C., S. Elgar, and R. T. Guza (1995), Infragravity-frequency (0.005- 0.05 Hz) motions on the shelf. part ii : Free waves, *J. Phys. Oceanogr*., 25, 1063-1079.

Inman, D.L., Bagnold, R.A., (1963), Littoral processes. In: Hill, M.N. (Ed.), The Sea, Vol. 3. Wiley-Interscience, New York, pp. 529-553.

Jaramillo S. and G. Pawlak, (2011), Coral reef hydrodynamics: AUV-based bed-roughness mapping over a tropical reef, *Coral Reefs*, doi:10.1007/s00338-011-0731-9.

Kennedy D. M. and C. D. Woodroffe (2002), Fringing reef growth and morphology: a review, *Earth Sc. Rev.,* vol. 57, 255-277.

Longuet-Higgins M. S. and R. W. Stewart, (1962), Radiation stress and mass transport in gravity waves, with application to ”surf beats”. *J. Fluid Mech*., 13, 481–504.

Lowe R. J. , J. L. Falter, J. R. Koseff, S. G. Monismith, and M. J. Atkinson (2007), Spectral wave flow attenuation within submerged canopies: Implications for wave energy dissipation, *J. Geophys. Res*., 112, C05018, doi:10.1029/2006JC003605.

Madin J. S., S. R. Connolly (2006), Ecological consequences of major hydrodynamic disturbances on coral reefs, *Nature* , 444 (7118), 477-480 doi: 10.1038/nature05328.

Martinez M. L., A. Intralawan, G. Vázquez, O. Pérez-Maqueo, P. Sutton and R. Landgrave (2007), The coasts of our world: Ecological, Economic and Social Importance, . *Ecological Economics*, 63**,** 254–272.

Mei, C.C., I. C. Chan, P. L. F. Liu, Z. H. Huang, W. B. Zhang (2011), Long waves through emergent coastal vegetation, *J. Fluid Mech*., 687,461-491 doi: 10.1017/jfm.2011.373.

Minura N. (1999) Vulnerability of island countries in the South Pacific to sea level rise and climate change, Climate Res. 12 137-143.

Monismith S. (2007), Hydrodynamics of coral reefs. *Annu Rev Fluid Mech* 39, 37–55.

Munk W. H. (1949) Surf beat. Eos Trans. AGU, 30:849–854.

Nelson, R.C. (1996), Hydraulic roughness of coral reef platforms. *Appl. Ocean Res.,* 18, 265–274.

Nunes, V. and G. Pawlak (2008), Observations of bed roughness of a coral reef. *J. Coast. Res.,* 24(2B), 39–50.

Oltman-Shay J., P. Howd, and W. Birkemeier (1989), Shear Instabilities of the Mean Longshore Current 2. Field Observations, *J. Geophys. Res*., 94(C12), doi:10.1029/JC094iC12p18031.

Pilkey O. H. and K. L. Dixon (1996), The Corps and the shore, Island Press, Washington DC.

Riffe, K. C., S. M. Henderson, and J. C. Mullarney (2011), Wave dissipation by flexible vegetation *Geophys. Res. Lett.*, 38 (L18607), doi: 10.1029/2011GL048773.

Rosman, J. H. and J. L. Hench (2011), A framework for understanding drag parameterizations for coral reefs, *J. Geophys. Res.*, doi:10.1029/2010JC006892.

Ruessink B. G. (1998a), Bound and free infragravity waves in the nearshore zone under breaking and nonbreaking conditions. *J. Geophys. Res*., 103(C6), 12,795–12,805.

Ruessink B. G. (1998b), The temporal and spatial variability of infragravity energy in a barred nearshore zone. *Cont. Shelf Res*., 18, 585–605.

Ruessink, B.G. (1998c), Infragravity waves in a dissipative multiple bar system, PhD dissertation, Institute for Marine and Atmospheric research Utrecht (IMAU), Utrecht University , Utrecht, Netherlands.

Sheremet, A., S. Jaramillo, S. F. Su, M. A. Allison, K. T. Holland (2011), Wave-mud interaction over the muddy Atchafalaya subaqueous clinoform, Louisiana, United States: Wave processes, *J. Geophys. Res*. 116 (C06005), doi: 10.1029/2010JC006644.

Storlazzi, C.D., J. B. Logan, and M. E. Field (2003), Quantitative morphology of a fringing reef tract from high-resolution laser bathymetry: Southern Molokai, Hawaii. *Geological Society of America Bulletin*, 115(11), 1344-1355.

Storlazzi, C.D., M. E. Field, K. Rogers, P. L. Jokiel, E. Brown, and J. D. Dykes (2005), A model for wave control on coral breakage and species distribution in the Hawaiian islands, *Coral Reefs*, v. 24, pp. 43-55.

Suzuki, T., M. Zijlema , B. Burger, M. C. Meijer , and S. Narayan (2012), Wave dissipation by vegetation with layer schematization in SWAN, *Coast. Eng*. 59(1), 64-71, doi: 10.1016/j.coastaleng.2011.07.006.

Symonds G., D. A. Huntley, and A. J. Bowen (1982) Two-dimensional surf beat: long wave generation by a time-varying breakpoint. *J. Geophys. Res*., 87(C1):492–498.

Symonds G., K. Black, and I. Young (1995), Wave-driven flow over shallow reefs, *J. Geophys. Res.,* 100, C2, doi:10.1029/94JC02736

Taebi S., R. J. Lowe, C. B. Pattiaratchi, G. N. Ivey, G. Symonds, and R. Brinkman (2011), Nearshore circulation in a tropical fringing reef system, *J. Geophys. Res*., 116, C02016, doi:10.1029/2010JC006439.

Symonds G., L. Zhong, and N. A. Mortimer (2011), Effects of wave exposure on circulation in a temperate reef environment, *J. Geophys. Res*., 116, C09010, doi:10.1029/2010JC006658.

Thomson J., S. Elgar, B. Raubenheimer, T. H. C. Herbers, and R. T. Guza (2006), Tidal modulation of infragravity waves via nonlinear energy losses in the surfzone. *Geophys. Res. Lett*., 33(L05601).

Tucker M. J. (1950), Surf beats: sea waves of 1 to 5 min. period. *Proc. Roy. Soc. London Ser. A*, 214, 79–98.

Vetter O. J., J. M. Becker, M. A. Merrifield, A. C. Péquignet, J. Aucan, S. J. Boc, C. E. Pollock (2010), Wave setup over a pacific island fringing reef. *J . Geophys. Res*., 115, C12066, doi:10.1029/2010JC006455.

Figure 1.1: Example of short wave dissipation in the nearshore: Japan tsunami March 2011, Images courtesy of Xinhua Press/Corbis (top) and Waimea shore break (bottom).

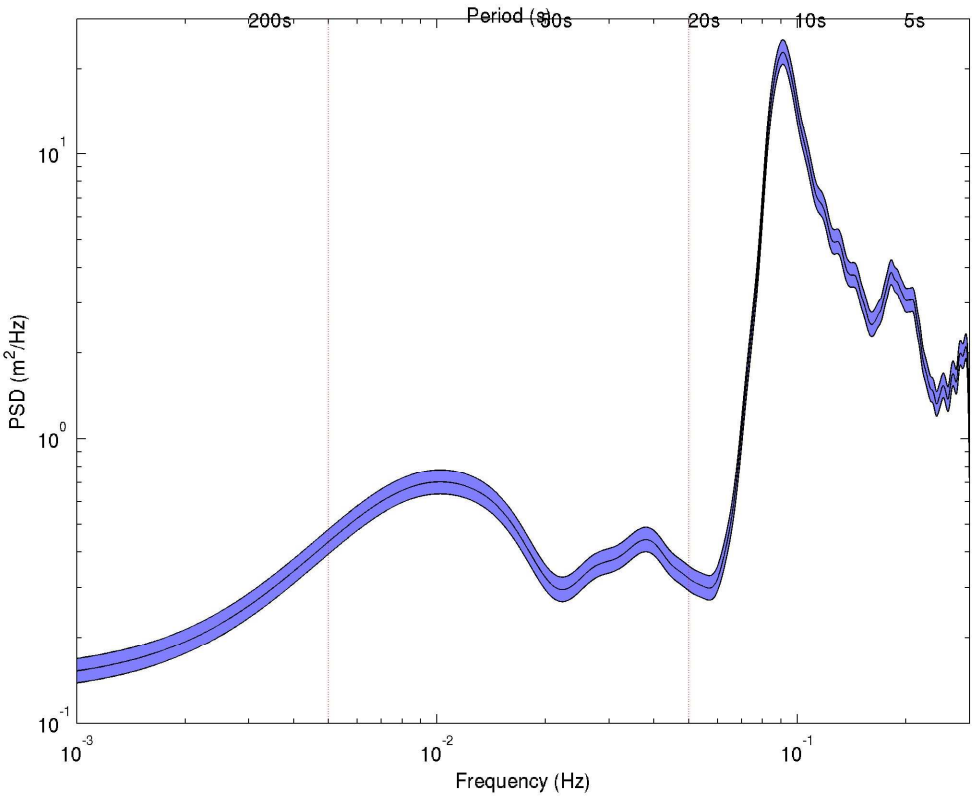

Figure 1.2: Typical energy spectrum observed at Guam in 8m of water. Blue shaded area shows the 95% confidence interval.

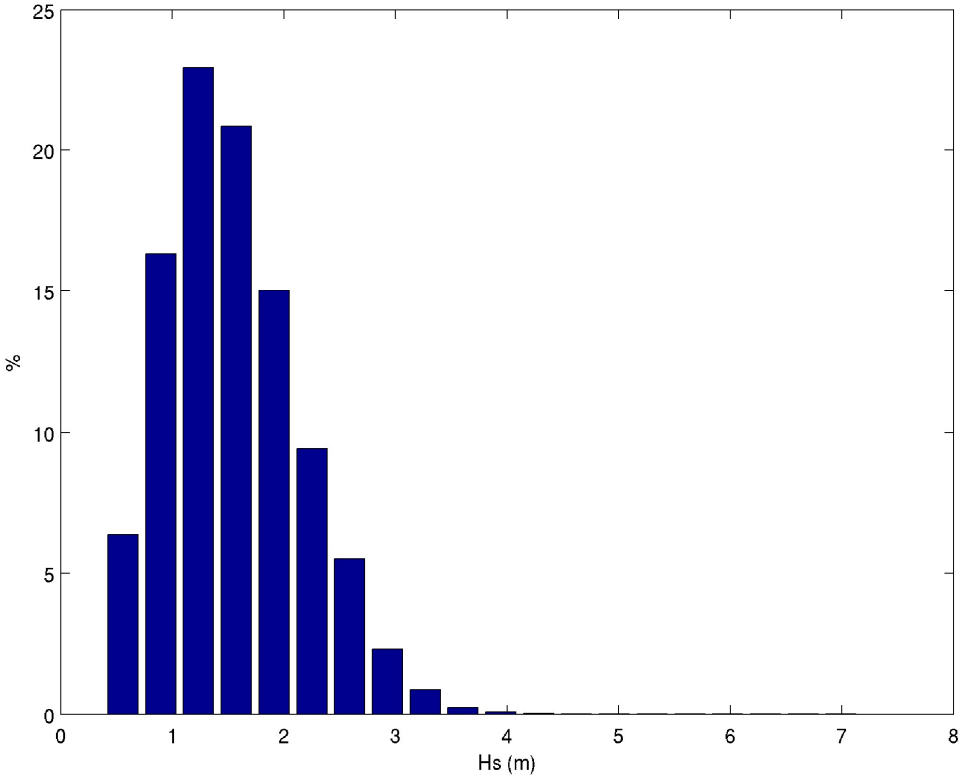

Figure 1.3: Histogram of 30 minute wave height distribution at the Guam offshore buoy located 2.4 km southeast of Ipan (13° 21'15"N, 144° 47'18"E) in 200 m depth between 2005 and 2011. The prevailing trade wind wave conditions with wave height between 1 and 2 m represent more than 58% of the waves observed.

Chapter 2

The dissipation of wind wave energy across a fringing reef at Ipan, Guam

This chapter is adapted from:

Péquignet A. C., Becker J. M., Merrifield M. A., Boc S. J. (2011) The dissipation of wind wave energy across a fringing reef at Ipan, Guam. *Coral Reefs- Coral reef hydrodynamics special series* 30, 71-82, doi: 10.1007/s00338-011-0719-5.

2.1 Introduction

Wave transformation processes on various reef geometries have been the focus of field and laboratory studies (e.g., Tait 1972, Gerritsen 1981, Young 1989, Hardy and Young 1996, Kench 1998, Lowe *et al*. 2005, Gourlay and Colleter 2005, Kench and Brander 2006). Monismith (2007) and Hearn (2010) provide two excellent overviews of reef hydrodynamics. Wave breaking over shallow reef topography tends to account for the majority of energy dissipation in the sea and swell (SS) frequency band (0.06 to 0.3 Hz) (Young 1989, Hardy and Young 1996, Massel and Gourlay 2000). As the incident waves propagate into shallow water on the reef flat, frictional effects become increasingly important. On some barrier reefs, friction has been shown to be the dominant dissipative process (Lowe *et al*. 2005). As incident waves break at the reef

face, radiation stress gradients forces the setup of the sea surface shoreward of the break zone (Munk and Sargent 1948, Bowen *et al*. 1968, Gourlay 1996a, 1996b). The nearshore region of shallow reefs tends to be dominated by long waves at infragravity (IG) frequencies (e.g., Young 1989, Lugo-Fernandez *et al*. 1998b), similar to the swash zone of dissipative sandy beaches (Raubenheimer and Guza 1996, Ruggiero *et al*. 2004).

The transmission of SS energy toward shore is affected by water level over reefs, with increasing wave energy on reef flats observed for increasing tidal level (Young 1989, Hardy and Young 1996, Lugo-Fernandez *et al*. 1998a, Brander *et al*. 2004). During large wave events, wave setup may exceed the highest tidal range (Péquignet *et al*. 2009). Estimates of wave transformation and dissipation on reefs have been evaluated primarily using laboratory data (e.g., Gourlay 1996a, 1996b, Gourlay and Colleter 2005, Massel and Gourlay 2000). Most observational studies to date have captured only moderate wave events and limited sea level ranges, hence, open questions remain regarding the reef flat SS energy budget during large wave events that generate significant setup and conditions that may allow significant SS energy to reach the shore.

The goal of this paper is to analyze field observations of waves across a shore-attached fringing reef to account for the amount of SS energy that reaches the shore as a function of incident wave conditions, water level over the reef, and position on the reef flat. We first detail the field experiments at Ipan and the data analysis methods. The observations then are used to analyze wave dissipation on the fore reef and reef flat. The dissipation estimates are incorporated in the one dimensional integration of the SS energy

flux balance across the reef to examine the effects of varying wave height and water level on reef flat wave heights. We conclude with an assessment of the effects of reef flat water level on shoreline wave energy.

2.2 Field experiment and methods

2.2.1 Site and sensors

Data used in this study were collected as part of the Pacific Island Land-Ocean Typhoon (PILOT) project which is aimed at assessing coastal inundation at reef-fringed islands during large wave events.

The study site at Ipan (Figure 2.1), on the south shore of Guam (13^{o} 22'20"N, 144^{o} 46'30"E), is composed of a steep (4° slope) fore reef with irregular and rough topography of ~ 100 m wavelength, ~5m amplitude spur-and-groove coral structures extending from approximately 15 m depth (Figure 2.2a) to the shallow crest at the reef edge (Figure 2.2b). The reef crest is porous and covered by macro and coralline algae (Figure 2.2c). The shallow 450 m wide reef flat is a carbonate pavement covered by macro algae (Figure 2.2d) extending from the reef crest to a narrow sandy beach (Burbick 2005). The tides in Guam are mixed with a mean range of 0.5 m and spring tide range of 0.7 m. The reef flat is mostly exposed at low tide. The eastern side of Guam is subject to trade winds and occasional tropical storms and typhoons (Lobban and Schefter 1997), which have been responsible for significant wave overwash along the south shore of Guam (Jaffe and Richmond 1993).

Offshore wave conditions were obtained from a Datawell directional wave buoy operated by the Scripps Institution of Oceanography Coastal Data Information Program (CDIP) located 2.4 km southeast of the reef array (13° 21'15"N, 144° 47'18"E) in 200 m depth. CDIP provides time series of significant wave height, dominant wave direction, and wave period over 30 minute intervals. An array of Seabird SBE 26Plus wave and water level recorders and Nortek Aquadopp Acoustic Doppler Profilers (ADP) was deployed across the reef, with two instruments on the fore reef and the remainder on the reef flat (Figure 2.1). Deployments of 3 to 6 months of varying number of instruments and sampling schemes were carried out from August 2005 to April 2010. The 2 subsets of data used in this study were collected during June and July 2007 (deployment G) and from September to November 2009 (deployment N). These subsets are the most complete sets of data needed for the present study and included a number of representative large wave events. The ADPs sampled at 1 Hz in bursts of 2 hours every 3 hours during N, and every 4 hours during G. All sensors sampled at 1 Hz and sampling details and sensor locations are summarized in Table 2.1.

Pressure measurements were corrected for atmospheric pressure variations using a SBE 26Plus deployed on land (sensor atm P Figure 2.1). Using linear wave theory, sea surface elevations and surface velocities were estimated from bottom pressure and mid-column velocity by applying a frequency depend correction to account for depth attenuation. Changes in water temperature on the reef account for uncertainties of less than 0.2% in the estimation of sea surface elevation from the bottom pressure. At

exceptionally low tides, the reef flat sensors were exposed and these sections of data are not used in the analysis.

Spectral properties were estimated based on Fourier transforms of two hour detrended and detided pressure data segments and band averaged using a Parzen spectral window, yielding approximately 22 degrees of freedom. Significant wave heights were estimated over 15 minute intervals from the variance of sea surface elevation in the SS band ($0.06 \text{ Hz} < f < 0.3 \text{ Hz}$). Following Vetter *et al.* (2010), setup on the reef flat was estimated at reef flat sensors by taking the difference of the 15-minute mean water level between the given sensor and sensor 10, with linear trends removed to account for sensor related drifts in pressure that are unrelated to wave height. A linear trend was removed from all sensors for consistency, but the results are similar with or without the trend removal. An offset was specified so that setup is zero when incident wave heights at sensor 10 are zero.

During deployment N, typical trade wind conditions were observed with incident wind wave height in the 1-2 m range, and some energetic events reaching 4m (Figure 2.3e). Peak wave periods ranged from 5 to 15 seconds (Figure 2.3f). The trade wind waves generally propagated from the ENE to ESE directions (Figure 2.3c). Calm summer conditions during deployment G preceded tropical storm (later upgraded to typhoon) Man-Yi (9 July 2007), which passed 200 nm south of Guam. Man-Yi resulted in offshore wave heights of nearly 8 m, peak period of 11 seconds, and wave arrivals from the SE (Figure 2.3 a, b, c). The large waves during this event led to high setup on

the reef (Péquignet *et al*. 2009), and inundation along some parts of the south shore of Guam. Observations of large wave events (> 2m) were made at different phases of the tide (Figure 2.3d, h). For both deployments, wave heights at the fore reef in 8m depth tended to be weaker than wave heights at the wave buoy (Figure 2.3a, e). This decrease in wave height depended on wave direction and in particular during Man-Yi when the waves came from the south, wave heights were 30% smaller at the fore reef than at the offshore buoy, presumably due to refraction effects.

2.2.2 Energy analysis

We evaluate the effects of wave dissipation in the context of changes in the cross-shore component of the energy flux, which is computed spectrally as

$$F_x(f) = 12 c_g(f) \rho f) \; _{\eta\eta}(f) \qquad (2.1)$$

where ρ is the water density, g is the acceleration due to gravity, $c_g(f)$ is the group velocity, and $S_{\eta\eta}(f)$ is the auto-spectra of η. The angle of incidence at the most offshore current-meter location (Figure 2.3d and h), was always within 15^o of shore normal due to wave refraction and we assume that the energy flux is predominantly in the cross-shore direction. Comparison of computations of the vector energy flux at the ADPs with (1) supports the assumption that the flux is in the onshore direction.

With the assumption of normal incidence, and neglecting time-dependent changes in energy, the cross-shore component of the energy flux divergence in the SS band over a 1D bathymetry may be written as

$$\frac{dF_{SS}}{dx} = < \varepsilon_b > + < \varepsilon_f > + < N > \qquad (2.2)$$

where the SS energy flux F_{SS} is estimated by integrating (2.1) over the SS frequency band, and $<\varepsilon_b>$ and $<\varepsilon_f>$ are the average rates of dissipation per unit area due to wave breaking and bottom friction respectively. $<N>$ is the non-linear transfer of SS energy to other frequency bands,

which has been observed previously on a reef during small wave conditions (Hardy and Young 1996).

Parameterizations of the energy loss due to wave breaking for sandy beaches have been applied to reef settings (Young 1989, Massel and Gourlay 2000). Here, we evaluate dissipation due to breaking following of Thornton and Guza (1983). For a saturated wave field, the assumption that $H_b/h=O(1)$ near breaking (Baldock *et al*. 1998) reduces the average rate of dissipation to a quadratic function of breaking wave height H_b (Battjes and Janssen 1978)

$$< \varepsilon_b > \approx B_r \rho g \overline{f} H_b^2 \qquad (2.3)$$

where $\overline{f}$ is the representative frequency of the random wave field and B_r is an empirical coefficient representing the fraction of foam on the wave face.

In addition, the parameterization of frictional dissipation also follows Thornton and Guza (1983)

$$< \varepsilon_f >= \rho C_f \frac{1}{16\sqrt{\pi}} \left(\frac{2\pi \overline{f}}{\sinh kh} \right)^3 H_{rms}^3 \qquad (2.4)$$

where h is the water depth, k is the wave number associated with $\overline{f}$ and h, and $H_{rms} = 1/\sqrt{2} H_s$ is the root mean square wave height. The ratio of H_{rms} / H_s results from the wave height following a Rayleigh distribution. This assumption of Rayleigh distributed wave heights is valid on the fore reef and the reef flat. In the surf zone (sensors 6 and 7), the wave height distribution departs slightly from Rayleigh and this ratio may be slightly underestimated (Massel 1996).

2.3 Results

2.3.1 Observations

The typical example of the power spectral density of sea surface elevation (Figure 2.4) illustrates the change from short waves to long waves shoreward across the reef. On the fore reef (sensor 10), the wave field is dominated by SS oscillations with a peak

frequency between 0.08-0.1 Hz. On the reef flat, less than 10m from the reef crest (sensor 7), the SS wave energy has decreased by nearly an order of magnitude, although the SS peak is still evident. At sensor 5, 57 m inshore of sensor 7, the SS energy is attenuated further, particularly at the incident spectral peak. Near the shoreline (sensor 2), the SS energy peak is absent. At IG frequencies (< 0.06 Hz), energy levels at the fore reef (sensor 10) and outer reef (sensors 7 and 5) are comparable. At the shoreline (sensor 2), IG energy is lower than the outer reef and fore reef at frequencies > 0.01 Hz, and higher at frequencies < 0.01 Hz. In addition, the spectrum at sensor 2 exhibits a peak between 0.02-0.06 Hz, although the energy in this band still is significantly lower than farther offshore. The increasing relative importance of IG compared to SS oscillations with decreasing distance from the shore has been reported for other reefs (Hardy and Young 1996, Lugo-Fernandez *et al*. 1998a). The peak energy at 0.02-0.06 Hz may be associated with long incident SS waves, or subharmonics of the incident peak over the reef. For this analysis, we will consider that energy as part of the IG band, which will be examined in a future study.

Mean water level near the shore (Figure 2.5a) exhibits setup variations that scale with SS significant wave height on the fore reef (Figure 2.5b). During large wave events, the setup exceeds the tidal range. Significant wave heights at the reef crest (sensor 6), mid-reef (sensor 4) and near the shore (sensor 2) show the nearly order of magnitude decrease in wave energy between the fore reef and reef crest, as well as the further dissipation of energy between the reef crest and the shore. The modulation of wave height with water depth is observed for all sensors on the reef flat. Depth-limited breaking at the reef edge

appears to influence significantly the transmission of SS wave energy on to the reef. The SS wave height is reduced by 90% between sensors 10 and 2 during high tide, 99% during low tide, and 97% averaged over all water depths.

Following Sheremet *et al*. (2002), we estimate that less than 5% of the incident SS wave energy flux is reflected at the fore reef (sensors 9 and 10) during deployment N. Of the incoming energy flux measured at 8m depth on the fore reef, 83% of this energy flux remains at sensor 9, 2% at 6, and 0.1% at sensor 2 (Figure 2.6). The region between sensors 9 and 7 corresponds to the location of a narrow breaker zone based on visual observations. These reductions in SS energy are consistent with previous studies (e.g., Young 1989, Kench 1998, Lugo-Fernandez *et al*. 1998a, Massel and Gourlay 2000, Brander *et al*. 2004).

The transformation of low frequency IG waves will be discussed in a separate paper, but estimates of the cross-shore components of IG and SS energy flux divergence are compared here to assess the possible importance of non linear energy transfer (<N>) in the SS energy balance (2.2). IG energy fluxes are estimated at the ADP sensors following Sheremet *et al*. (2002) and are integrated over the IG band (0.005 to 0.06 Hz). On the reef flat, inshore of the break point, (from sensor 6 to sensor 2) the IG energy flux decays at a similar rate as the SS band, which we attribute to decay due to bottom friction. Offshore of sensor 6, the decrease of SS energy flux is an order of magnitude larger than the estimated changes in IG energy flux. While $<N>$ is important in the IG energy balance, it is negligible in the SS energy balance (2.2).

We next compare the cross-shore energy flux divergence in the SS band with parameterizations of dissipation based on significant wave height (equations 2.3 and 2.4). On the fore reef and the reef flat the dependence of the SS energy flux divergence dF_{SS}/dx with significant wave height is approximately cubic (Figure 2.7 **a** and **c**), while near the reef crest the dependence is quadratic (Figure 2.7 b). For deployment G, the dependence of energy flux divergence on H_{rms}^3 on the reef flat (between sensors 5 to 2) is similar to that for deployment N on the reef flat (between sensors 4 and 2) (Figure 2.7c). On the reef crest, between sensors 9 and 6, the observed quadratic dependence of the energy flux divergence with incident wave height (Figure 2.7b) suggests dissipation due to breaking following the model of a saturated surf zone (2.3). We estimate the breaking parameter B_r by assuming that dissipation due to bottom friction between sensors 9 and 6 is negligible compared to the dissipation due to wave breaking. A least squares fit of equation (2.3) to the data in Figure 2.7b gives a value of $B_r = 0.05$ (± 0.005, 95% confidence interval estimated from independent data separated by 8 hours) which is equivalent to the value used by Young (1989). This breaking parameterization does not account for steepness of the fore reef (Massel and Gourlay 2000) and the porous nature of the bottom near the reef edge. The value of B_r may implicitly incorporate these topographic and permeability effects. At Ipan where breaking is confined to a narrow section around the reef crest, a constant value of B_r independent of bottom characteristics is reasonable. B_r may however vary with wave conditions and this may explain the scatter of the points in Figure 2.7b**.**

The reef flat and fore reef divergences are best fit with cubic wave height dependence (Figure 2.7 a and c). Estimation of the friction coefficient by least squares fit

of equation (2.4) to the data in Figure 2.7 (a and c), yields a value of C_f =0.06 (±0.02, 95% confidence interval) on the reef flat and C_f =0.2 (± 0.05) on the fore reef. The present estimates of C_f agree with values of f_w (=2 C_f) determined for other reefs (e.g., f_w= 0.1 to 0.7, Ala Moana (Gerritsen 1981); f_w= 0.1-0.7, Ningaloo (Hearn 1999); f_w= 0.07 to 0.22, John Brewer reef (Nelson 1996); C_f =0.03 to 0.1, Kaneohe (Hearn 1999)).

The spatial variability of the friction factor is related to the spatial variability of roughness length across the reef (Hearn 2010). The friction factor f_w has been related to bed hydraulic roughness or equivalent Nikuradse roughness height, r, (Swart 1974, Mirfenderesk and Young 2003). For a fully rough turbulent flow, Swart (1974) provides the following explicit formulation for f_w,

$$f_w = \exp\left(5.213 \left(\frac{r}{a} \right)^{0.194} - 5.977 \right) \tag{2.5}$$

where a is the wave orbital diameter at the bed. Equation (2.5) suggests that the friction factor is a function of the wave conditions through the orbital amplitude. Here, using the constant values estimated above, we compute the range of roughness that results from equation (2.5). On the fore reef equation (2.5) yields a value of r between 1 and 4 m. On the reef flat, r ranges from 0.10 to 0.40 m. A roughness scale of order of meters is reasonable based on visual observations of the spur and groove structure on the reef face (Figure 2.2). On the reef flat, roughness of tens of centimeters is reasonable for Ipan and comparable to roughness estimates on similar reefs (Nelson 1996, Nunes and Pawlak 2008).

2.3.2 Estimation of energy flux transformation

Reef flat SS wave heights scale with incident wave height and with water depth over the reef (Figure 2.5). Because water depth on the reef also is correlated with incident wave height due to wave setup, it is unclear to what extent the wave energy on the reef is tidally-limited. To examine this issue as well as to consider reef flat wave heights for a greater range of conditions than observed, the friction (2.4) and wave breaking (2.3) energy loss parameterizations are used in a straight forward numerical integration of SS momentum and energy flux equations across the reef (from sensor 10 to sensor 2). The use of the 1D integration of the wave energy flux balance is intended as a tool to interpret the observations in the context of the simplest dynamics that governs the transformation. The equations are discretized using an explicit forward scheme. Inputs for the calculation are the bottom topography (Figure 2.1) the 15-minute mean tidal level d, incident significant wave height, H_s, and peak period, T_p, at sensor 10. The parameters and input variables used for each estimate are summarized in Table 2.2. The energy flux balance (2.2) is integrated with the bottom friction term $<\varepsilon_f>$ specified at every cross-shore grid point, the breaking term ε_b included in regions where the breaking criterion is met ($H_s \geq \gamma_b h$, γ_b=1.15), and the non linear term neglected everywhere yielding,

$$\frac{dF_{SS}}{dx} = \rho C_f \frac{1}{16\sqrt{\pi}} \left(\frac{2\pi \overline{f}}{\sinh kh} \right)^3 H_{rms}^3 + \mathrm{H}(H_s - \gamma_b h) B_r \rho g \overline{f} H_b^2 \qquad (2.6)$$

where H is the Heaviside step function and H_b is the breaking wave height equal to the local wave height if the breaking criterion is met. At each spatial increment (dx=1 m), the

total depth is given by $h = d + \overline{\eta}$, where d is the tidally varying water level, assumed spatially constant across the reef, and $\overline{\eta}$ is the wave setup, which varies across the reef. Setup is computed using a 4th-order Runge-Kutta scheme to solve the mean momentum equation

$$\frac{d\overline{\eta}}{dx} = -\frac{1}{\rho g(\overline{\eta} + d)}\frac{dS_{xx}}{dx} \qquad (2.7)$$

where S_{xx} is the cross-shore component of the radiation stress tensor (Longuet-Higgins and Stewart 1964). The radiation stress represents the excess of momentum flux due to the presence of waves. While wave bottom dissipation is included in the SS energy flux balance, the momentum contribution resulting from dissipation due to the current boundary layer is neglected in the setup balance (Longuet-Higgins 2005). Vetter *et al*. (2010) demonstrate that the effects of dissipation are small in the setup dynamics on the reef flat for Ipan. At each time and space iteration, the cross-shore SS energy flux F_{SS} is used to compute the total SS energy E_{SS}, the significant wave height H_s and the cross-shore radiation stress S_{xx} following

$$F_{SS} = c_g E_{SS} = \frac{1}{16} c_g \rho g H_s^2 \qquad (2.8)$$

$$S_{xx} = E_{SS}\left(2\frac{c_g}{c} - \frac{1}{2}\right) \qquad (2.9)$$

where c_g and c are the local group velocity and phase speed, at the peak SS frequency.

The choice of breaking criteria with respect to significant wave height $\gamma_b = 1.15$ is taken from the reported range of 0.4 to 1.8 (for a range of slope of 0.02 to 0.12) (Bowen *et al*. 1968, Tait 1972, Raubenheimer *et al*. 1996, Vetter *et al*. 2010), given the average reef face slope at Ipan of 0.07. This value of γ_b is consistent with the ratio of significant wave height to depth observed inshore of the break point at sensor 7 (H_s/h=1.4) and with the values estimated by Vetter *et al*. (2010) for the same reef, with a single breakpoint model. We use $C_f = 0.2$ on the reef face and crest, and 0.06 on the reef flat.

The estimated cross-shore transformation of SS energy is in reasonable agreement with observed energy levels during energetic wave events (Figure 2.8a). In particular, the sharp drop in energy through the surf zone (between sensors 9 and 6) is reproduced by the breaking parameterization, and the dissipation on the reef flat is accounted for by bottom friction. The correlation of observed and modeled H_{s2} ($\overline{\eta_2}$) is 0.89 (0.98) for deployment N and 0.97 (0.98) for deployment G. The simple dynamics of the 1D energy balance is in reasonable agreement with for the wave setup and the wave height transformation across the reef (Figure 2.8b, c). During Man-Yi, the numerical estimates underestimates the observed shoreline setup by about 30% (*Figure 2.8*), possibly due to currents and non-wave related sea level changes caused by winds during the storm. This underestimate of the water level may account partly for the overestimate of the wave height on the reef.

We next investigate the effect of independently changing incident wave height (H_{s10}), and tidal level (d) on the shoreline significant wave height H_{s2} and setup $\overline{\eta_2}$

(Figure 2.9) using the integration of equation (2.6) to (2.9). With all the other input variables remaining constant (see Table 2.2 "Indep. Increase" for values), the water level is linearly increased from 0 to 3 m for runs 1 to 300. The incident wave height is increased from 0 to 8 m for runs 301 to 600, and the incident wave period is increased from 5 to 20 s for runs 601 to 900. For a fixed incident wave height and period, wave height at the shoreline scales with water depth to the 1.38 power (Figure 2.9, runs 1 to 300). The increase in H_{s2} occurs with a moderate decrease in setup associated with a reduction of the radiation stress gradient as more energy propagates on to the reef. For a fixed tidal height and wave period, the wave height on the reef flat increases with incident wave height (Figure 2.9, middle panel). This increase is in part due to the increase in water depth on the reef from a nearly linear increase in wave setup (Figure 2.9e). The increase of wave height on the reef with incident wave height and water depth has been reported previously (Young 1989, Hardy and Young 1996, Lugo-Fernandez *et al*. 1998c) for barrier reefs under moderate wave conditions. Changing the incident wave period within the range of observed values (5 to 15 seconds), while fixing tidal level and incident wave height, results in only small increases for both H_{s2} and $\overline{\eta_2}$ (Figure 2.9, right panel).

We next focus on estimates of nearshore wave height for co-varying tidal level and incident wave height (Table 2.2 "co-varying"). The wave height near the shore is nearly constant for a given water depth on the reef regardless of whether the submergence is due to tides or wave setup (Figure 2.10a). Over a minimum incident wave height threshold for a given water depth on the reef, the wave height at the shore is nearly

independent of the incident wave height (Figure 2.10 b). For a reef configuration such as Ipan, where wave breaking is confined to a narrow zone around the reef crest, the threshold value is related to the shallowest depth observed at the reef crest. For waves smaller than γ_b times this depth, no breaking occurs and the wave height on the reef flat scales with incident wave height; for waves larger than γ_b times this depth, reef flat energy also increases with incident wave height, but this is a result of setup increasing with wave height.

Wave heights just shore-side of the surf zone (roughly sensor 6) are determined by total water level; however, additional decay occurs across the reef due to wave friction (Figure 2.5) so that narrower reef flats allow more energy to reach the shore. The wave height on the reef flat decreases nearly inversely with distance from the breaker zone. We find that for a 1D cross-shore model, reef width (defined as distance from the shore to the reef crest) does not affect setup significantly as previously observed in the laboratory by Seelig (1983).

2.4 Conclusion

Wave data collected for a range of incident conditions are used to analyze the strong dissipation of SS wave energy across Ipan reef, Guam, which results in ~ 97% reduction of the incident wave height over ~500 m. Less than 5% of the incident energy flux is reflected at the fore reef. Of the remaining SS energy that propagates toward shore, >80% is dissipated due to wave breaking, 18% by bottom friction on the rough

fore reef substrate (C_f = 0.2), and 2% by bottom friction on the wide reef flat (C_f = 0.06). These values of the friction factor are one and two orders of magnitude larger than the values observed on sandy beaches (Smyth and Hay 2002), but similar to value reported for other reefs (e.g., Gerritsen 1981, Nelson 1996, Hearn 1999).

As a result of the frictional dissipation, the decrease in wave height near the shore is inversely proportional to the width. Wave setup appears to be independent of reef width. This suggests that variation in coastal inundation along a shoreline with variable reef width and fixed incident wave height may be due to variable swash (e.g., inundation reports for the south shore of Guam during Typhoon Russ by Jaffe and Richmond 1993). Previous attempts to model wave dissipation across a proto-typical Guam fringing reef based on parameterizations developed using laboratory data (Massel and Gourlay 2000) produce qualitatively similar results to those presented here, with the majority of dissipation occurring in the surf zone. Water depth on the reef strongly controls the amount of SS energy that reaches the shore, consistent with wave dissipation being dominated by a depth-limited breaking process. Our observations show that the increase in reef flat wave heights with increasing incident wave height is primarily due to the linear increase in reef flat water depth due to wave setup. The water level on the reef, whether due to tides or setup, determines the reef flat wave height. This holds when the breaker zone is a limited region near the reef edge, as is the case for our observations. Based on the model results at the peak of Man-Yi and photographs taken during tropical storm conditions, we speculate that the breaker zone may extend across the reef flat for extreme typhoon conditions, in which case nearshore wave heights may well exceed

levels predicted here (i.e., larger than Figure 2.10 would indicate).

This paper emphasizes the importance of water level on the reef flat for coastal inundation. The potential effect of sea level rise on wave transformation over Ipan reef (assuming no change in topography) would be twofold: higher reef flat water levels would allow more sea and swell energy to reach the shore, but also would result in a moderate decrease in wave setup (Figure 2.9, left panel). The projected impact on coastal wave energy must take into account both of these effects. For example, an increase in sea level of 0.5 m over a range of incident wave height of 1 to 5 m yields an increase of SS wave height near the shore of 25 cm despite a 6 cm decrease of wave setup.

References

Baldock T. E., P. Holmes, S. Bunker, P. van Weert (1998), Cross-shore hydrodynamics within an unsaturated surf zone. *Coast. Eng.* 34, 173–196.

Battjes J.A., J. P. F. M. Janssen (1978), Energy loss and set-up due to breaking of random waves. Proceedings of the 16th international conference on coastal engineering conference, American Society of Civil Engineers, pp 569–587.

Bowen A. J., D. L. Inman, V. P. Simmons (1968), Wave set-down and wave set-up, J. Geophys. Res.73(8), 2569–2577.

Brander R. W., P. S. Kench, D. Hart (2004), Spatial and temporal variations in wave characteristics across a reef platform, Warraber Island, Torres Strait, *Australia. Mar. Geol.* 207(1–4), 169–184.

Burbick D. R, (2005), Guam coastal atlas. Report 114, University of Guam Marine Laboratory, Mangilao

Gerritsen F. (1981), Wave attenuation and wave set-up on a coastal reef. Technical report. Look Lab, Univ. Hawaii, Honolulu.

Gourlay M. R. (1996a), Wave set-up on coral reefs.1. Set-up and wave generated flow on an idealized two dimensional horizontal reef, *Coast. Eng.* 27(3-4),161–193.

Gourlay M. R. (1996b), Wave set-up on coral reefs. 2. Set-up on reefs with various profiles. *Coast. Eng.* 28(1-4), 17–55.

Gourlay M.R., and G. Colleter (2005), Wave-generated flow on coral reefs analysis for two-dimensional horizontal reef-tops with steep faces. *Coast. Eng* 52(4), 353–387.

Hardy T. A., and I. R. Young (1996), Field study of wave attenuation on an offshore coral reef*, J. Geophys. Res.*101(C6), 14,311–14,326.

Hearn C. J. (1999), Wave-breaking hydrodynamics within coral reef systems and the effect of changing relative sea level, *J. Geophys. Res*.104(C12), 30007–30019.

Hearn C. J. (2011), Hydrodynamics of coral reef systems. In: Hopley D (ed) Encyclopedia of Modern Corals. Springer.

Jaffe B. E., B. M. Richmond (1993), Overwash variability on the shoreline of Guam during Typhoon Russ. *Proc 7th Int Coral Reef Symp* 1, 257–264.

Kench P. S. (1998), Physical processes in an Indian Ocean atoll, *J. Coast. Res.* 17(2), 155–168.

Kench P. S., R. W. Brander (2006), Wave processes on coral reef flats: Implications for reef geomorphology using Australian case studies. *J. Coast. Res.,* 22(1), 209–223.

Lobban C. S., M. Schefter (1994), Tropical pacific island environments, 2nd edn. University of Guam Press, Guam

Longuet-Higgins M. S. (2005), On wave set-up in shoaling water with rough sea bed. *J Fluid Mech* 527, 217–234

Longuet-Higgins M. S., R. W. Stewart (1964), Radiation stress in water waves, a physical discussion with applications. *Deep-Sea Res* 11, 529–563

Lowe R. J., Falter J. L., Bandet M. D., Pawlak G., Atkinson M. J, Monismith S. G., Koseff J. R. (2005), Spectral wave dissipation over a barrier reef, *J. Geophys. Res*.110(C04001). doi:10.1029/2004JC002711.

Lugo-Fernandez A, Roberts HH, Wiseman WJ (1998a), Tide effects on wave attenuation and wave set-up on a caribbean coral reef. *Estuar. Coast. Shelf Sci.* 47(4), 385–393.

Lugo-Fernandez A, Roberts HH, Suhayda JN (1998b), Wave transformations across a Caribbean fringing-barrier coral reef. *Cont. Shelf Res.*18(10), 1099–1124.

Lugo-Fernandez A, Roberts HH, Wiseman WJ, Carter BL (1998c), Water level and currents of tidal and infragravity periods at Tague Reef, St. Croix (USVI), *Coral Reefs* 17(4), 343–349.

Massel S. R. (1996), Ocean surface waves: their physics and prediction. *Advanced series on ocean engineering* V. 11. World Scientific.

Massel S. R., M. R. Gourlay (2000), On the modelling of wave breaking and set-up on coral reefs. *Coast. Eng.* 39, 1–27.

Mirfenderesk H., I. R. Young (2003), Direct measurements of the bottom friction factor beneath surface gravity waves. *Appl Ocean Res* 25, 269–287.

Monismith S. (2007), Hydrodynamics of coral reefs. *Annu Rev Fluid Mech* 39, 37–55.

Munk W. H., and M. C. Sargent (1948), Adjustment of Bikini atoll to ocean waves. *Trans Am Geophys Union* 29, 855–860.

Nelson R. C. (1996), Hydraulic roughness of coral reef platforms. *Appl. Ocean Res.* 18, 265–274.

Nunes V, Pawlak G (2008) Observations of bed roughness of a coral reef. *J. Coast. Res.,* 24(2B):39–50

Péquignet A. C. N., J. M. Becker, M. A. Merrifield, and J. Aucan (2009), Forcing of resonant modes on a fringing reef during tropical storm Man-Yi. *Geophys. Res. Lett.* 36. doi:10.1029/2008GL036259.

Raubenheimer B., and R. T. Guza RT (1996), Observations and predictions of run-up, *J. Geophys. Res.*101(C11), 25575–25587.

Raubenheimer B., R. T. Guza, S. Elgar (1996), Wave transformation across the inner surf zone, *J. Geophys. Res.*101(C10) 25,589–25,597.

Ruggiero P., R. Holman, and R. Beach (2004), Wave run-up on a high energy dissipative beach, *J. Geophys. Res.*109. doi:10.1029/2003JC002160.

Seelig W. N, (1983), Laboratory study of reef-lagoon system hydraulics. *J. Waterw. Port Coastal Ocean Eng* ASCE 109:380–391.

Sheremet A., R. T. Guza, S. Elgar, and T. H. C. Herbers (2002), Observations of nearshore infragravity waves: Seaward and shoreward propagating components*, J. Geophys. Res*.107. doi:10:1029/2001JC000970.

Smyth C, A. E. Hay (2002), Wave friction factors in the nearshore sands, *J. Phys. Oceanogr*. 32(12), 3490-3498.

Swart D. (1974), Offshore sediment transport and equilibrium beach profiles. Technical report 131, Delft Hydraulic Laboratory, Netherlands.

Symonds G., K. P. Black, and I. R. Young (1995), Wave-driven flow over shallow reefs, *J. Geophys. Res*.100(C2), 2639–2648.

Tait R. J. (1972) Wave setup on coral reefs, *J. Geophys. Res*.77(C10), 2207–2211.

Thornton E. B., R. T. Guza (1983), Transformation of wave height distribution*, J. Geophys. Res*.88(C10), 5925–5938.

Vetter O. J., J. M. Becker, M. A. Merrifield, A. C. Péquignet, J. Aucan, S. J. Boc, and C. E. Pollock (2010), Wave setup over a pacific island fringing reef, *J. Geophys. Res*., 115, C12066, doi:10.1029/2010JC006455.

Young I. R., (1989), Wave transformations on coral reefs, *J. Geophys. Res*. 94(C7), 9779-9789.

Sensor number	Distance from shore	depth	G burst	G velocity	N burst	N velocity
1-atm		0 m	P: 43180s/12hrs		P: 43180s/12hrs	
2	30 m	0.3 m	P: 43180s/12hrs		PUV: 10800s/4hrs	0.2:0.1 m
3	195 m	0.4 m			P: 43180s/12hrs	
4	277 m	0.6 m			PUV: 10800s/4hrs	0.2:0.1 m
5	359 m	0.6 m	P: 43180s/12hrs			
6	399 m	0.6 m	PUV: 7200s/4hrs	0.3:0.1 m	PUV: 10800s/4hrs	0.2:0.1 m
7	416 m	0.3 m	P: 43180s/12hrs		P: 43180s/12hrs	
9	475 m	5.7 m	PUV: 7200s/4hrs	1:1 m	PUV: 10800s/4hrs	1:1 m
10	530 m	7.9 m	P: 43180s/12hrs		PUV: 10800s/4hrs	1:1 m

Table 2.1: Sensor location and sampling schemes for deployment G and N. P indicates a Seabird pressure sensor while PUV indicates an Aquadopp velocity and pressure sensor. Length and frequency of bursts are indicated as length/frequency. Velocities measurements are specified by cell size: blanking distance.

	G	N	Indep. increase	co-varying	Var. L	Var. Cf
Figure	2.9	2.9	2.10	2.11	Not shown	Not shown
B_r	0.075	0.075	0.075	0.075	0.075	0.075
γ_b	1.15	1.15	1.15	1.15	1.15	1.15
C_f slope	0.2	0.2	0.2	0.2	0.2	0-0.8
C_f flat	0.06	0.06	0.06	0.06	0.06	0-0.24
bathy	Ipan	Ipan	Ipan	Ipan	Modified Ipan	Ipan
d_2	15-min tide	15-min tide	0-3 m	0-2 m	0-2 m	0-2 m
H_{10}	15-min H_s	15-min H_s	0-8 m	0-6 m	0-5 m	0-5 m
T_{10}	15-min T_p	15-min T_p	5-15s	10 s	10 s	10 s

Table 2.2: Summary of parameters and input variables used for the different cases tested with the integration of the energy flux equation.

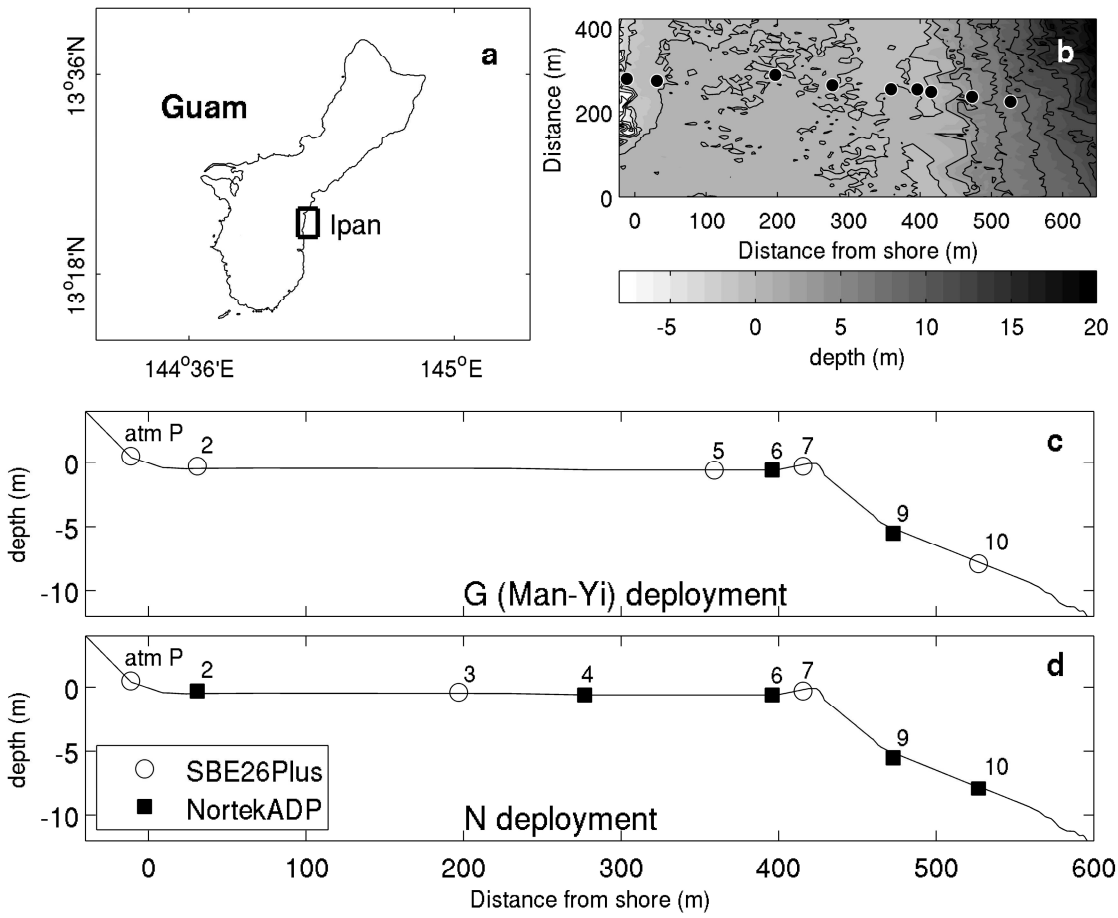

Figure 2.1: a) Location of Ipan reef, Guam. b**)** Bathymetry of Ipan reef from SHOALS data with locations of sensors. Cross-shore profile of Ipan reef with locations of sensors for deployments c) G (June- July 2007) and d) N (September-November 2009). Black squares indicate collocated pressure sensors and current-meters (Nortek ADP) and the white circles indicate single pressure sensors (SBE26plus). The sensor labeled 'atm P' is a SBE26plus deployed above sea level to measure atmospheric pressure.

Figure 2.2: Photos of the substrate for four locations across the reef: a) on the fore reef near sensor 9 in 5 meters of water, b) at the reef crest near sensor 7 (scale: the width of the bottom of the photo spans about 3m), c) on the outer reef flat near sensor 5 (scale: the current-meter shown is 60cm long), and d) on the reef flat near sensor 2 (scale: the yellow ruler is 30cm long).

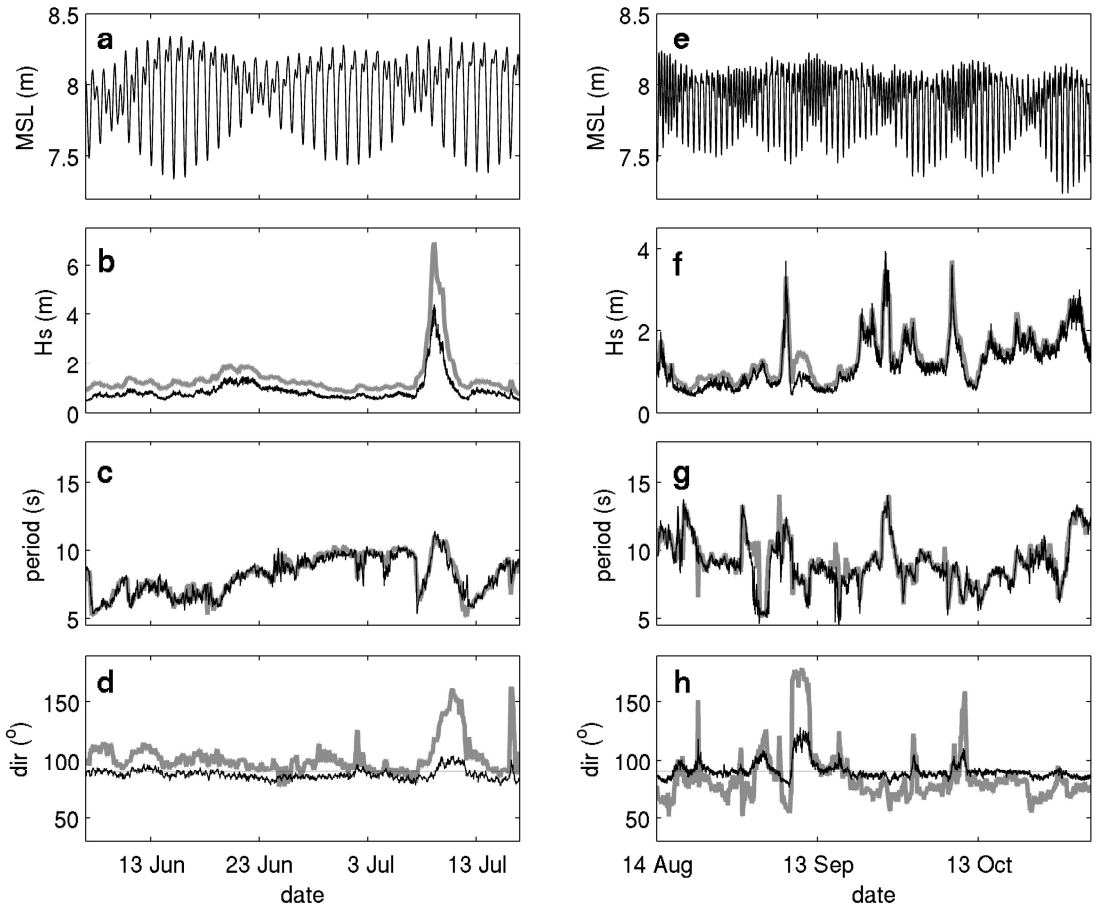

Figure 2.3: Wave and water level conditions at the fore reef during deployment G (left panels, June to July 2007) and deployment N (right panels, August to November 2009), including a) and e) water level, b) and f) sea and swell (SS) band significant wave height, c) and g) the peak SS wave period, and d) and h) the incident SS wave angle (relative to magnetic north) from the most offshore sensor (black line), and from the CDIP wave buoy (thick grey line). The variability of wave direction and period was smoothed by plotting the 6 hour running mean for clarity of the figure.

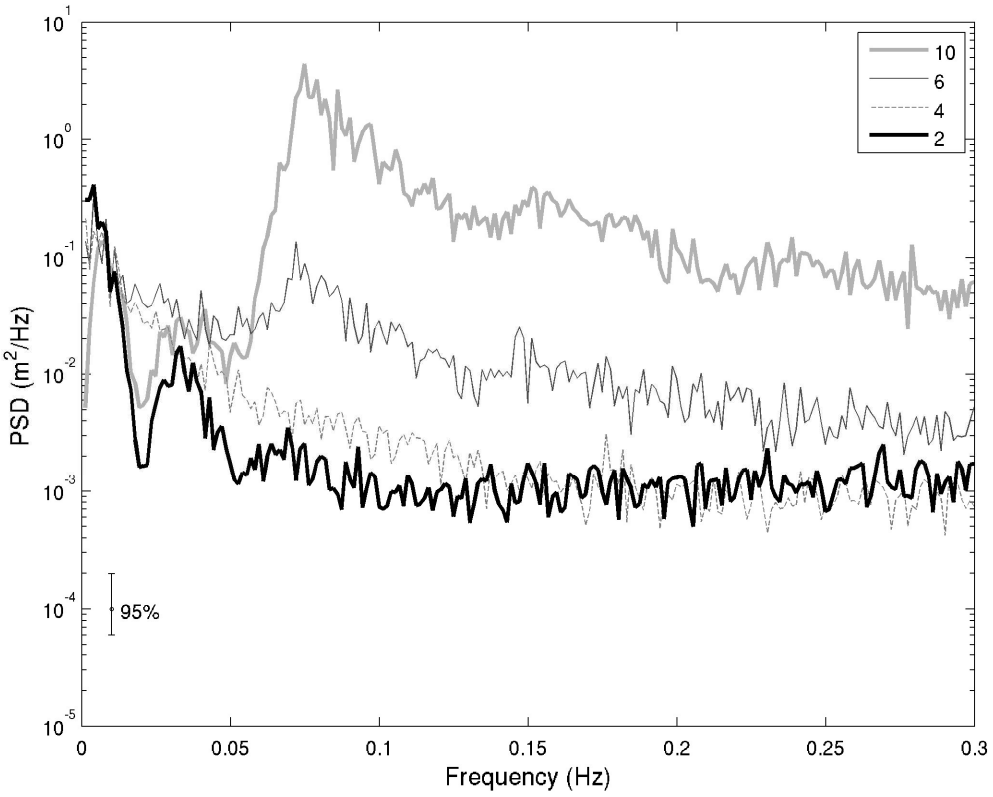

Figure 2.4: Power spectral density of sea surface elevation at the fore reef (sensor 10), the reef crest (sensor 6), the outer reef flat (sensor 4) and the inner reef flat (sensor 2) during largest event of deployment N (02 October 2009 21:00:00 UTM).

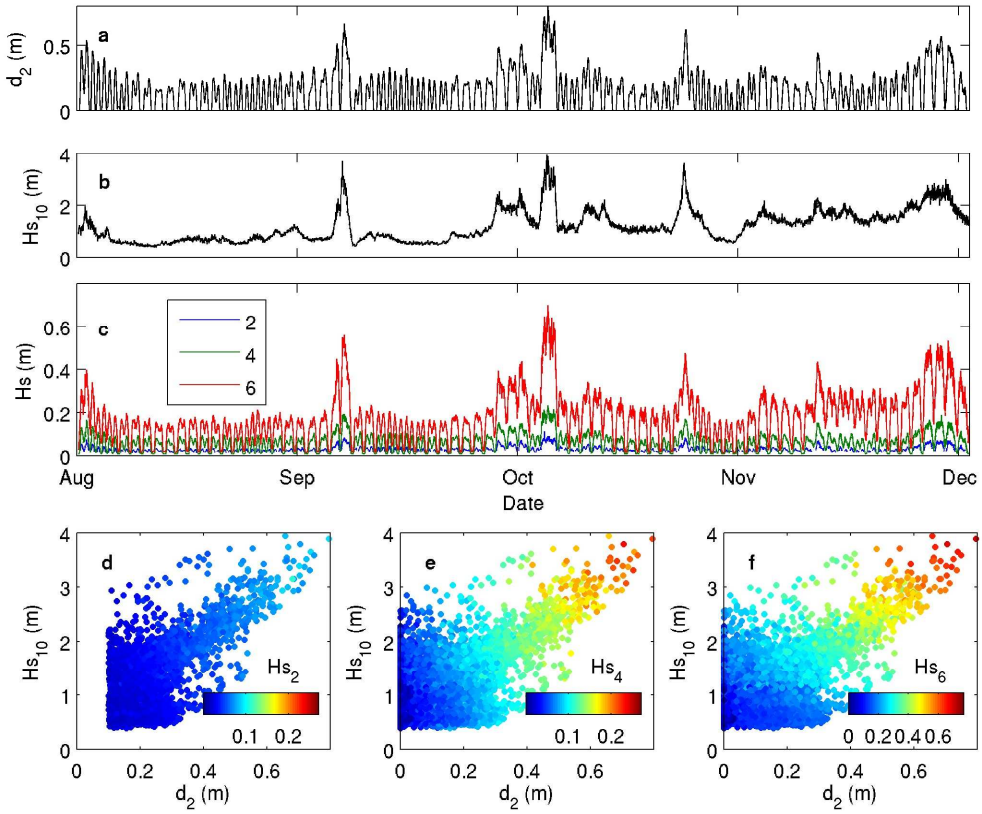

Figure 2.5: Time series during deployment N of a) water depth on the reef at sensor 2, d_2 including both tidal and wave setup components, b) incident significant wave height at sensor 10, Hs_{10} and c) wave heights on the reef flat at sensors 2, 4 and 6. Reef flat wave height plotted as a function of d_2 and Hs_{10} for d) sensor 2, e) sensor 4 and f) sensor 6.

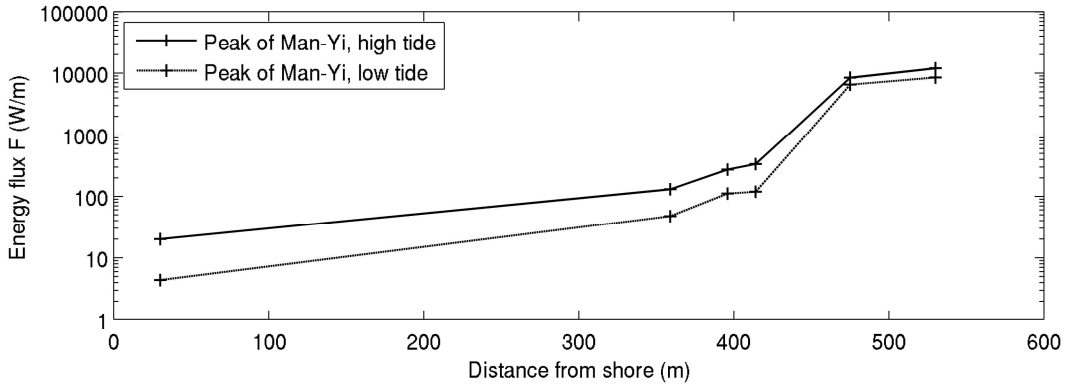

Figure 2.6: Cross-shore SS energy flux profile across the reef for low tide (dash line) and high tide (solid line) at the peak of Man-Yi.

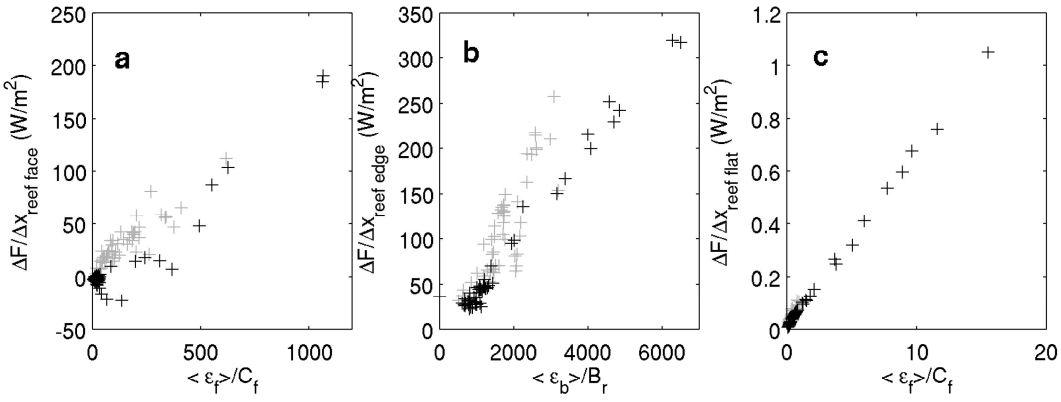

Figure 2.7: Average rate of dissipation per unit area at a) the fore reef (between sensors 10 and 9), b) the reef crest (between sensors 9 and 6), and c) the reef flat (between sensors 5/4 and 2 for deployment G/N) plotted against the best matching parameterization of dissipation, which is $<\varepsilon_f>/C_f$ from equation (2.4) for the fore reef and reef flat, and a wave breaking parameterization $<\varepsilon_b>/B_r$ from equation (2.3) for the reef crest. The breaking coefficient B_r and the friction coefficient C_f are estimated from the least square fit of the rate of dissipation with the best matching parameterization. Deployment N is shown by the grey + and deployment G is shown with the black +.

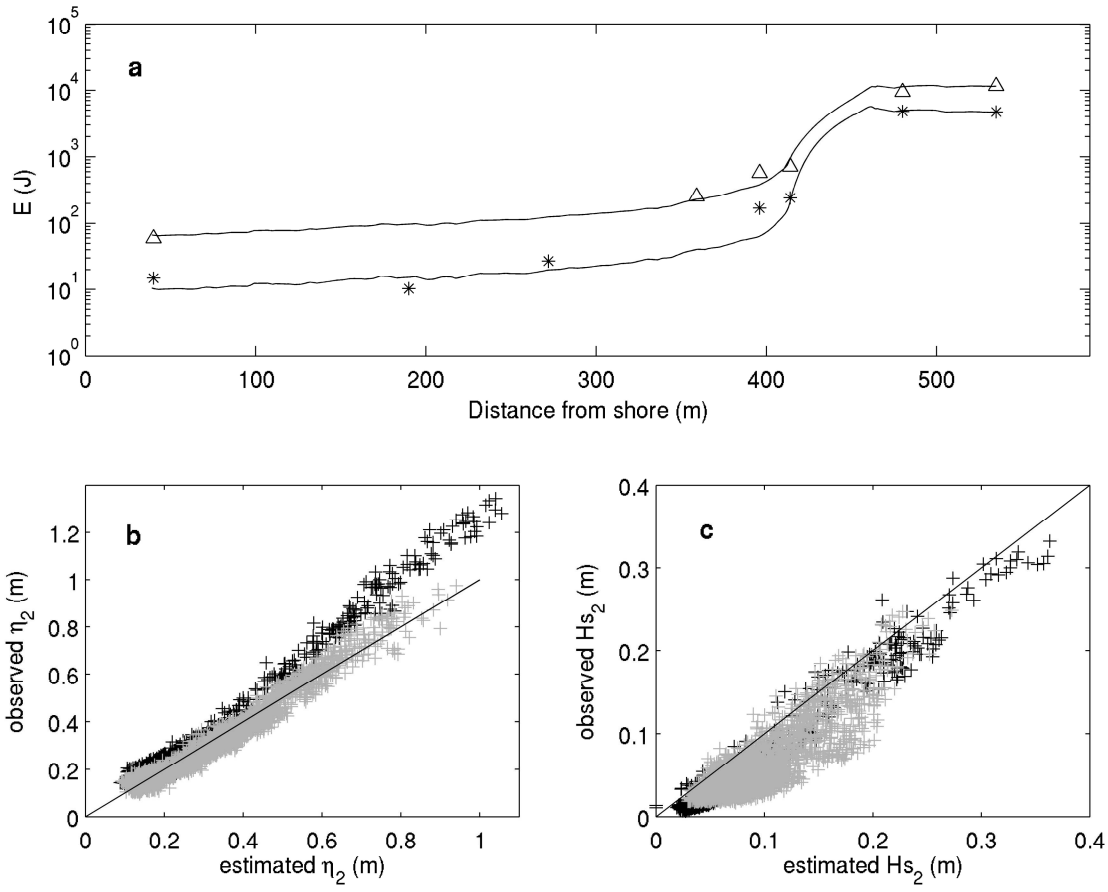

Figure 2.8**:** a) Comparison of total cross-shore SS energy during the peak event of N (*: 2 Oct. 2009, Hs=3.2m) and the peak of Man-Yi (Δ: 9 July 2007, Hs=4.3m). The solid lines are estimated energies computed from equations (2.6) to (2.9) (see Table 2.2- N and G). Comparison of observed and estimated (equations (2.6) to (2.9)) b) wave setup $\overline{\eta_2}$ and c) significant wave height Hs_2 at the inner reef flat (sensor 2) (see parameters and inputs in Table 2.2) for deployments G (black crosses) and N (grey crosses).

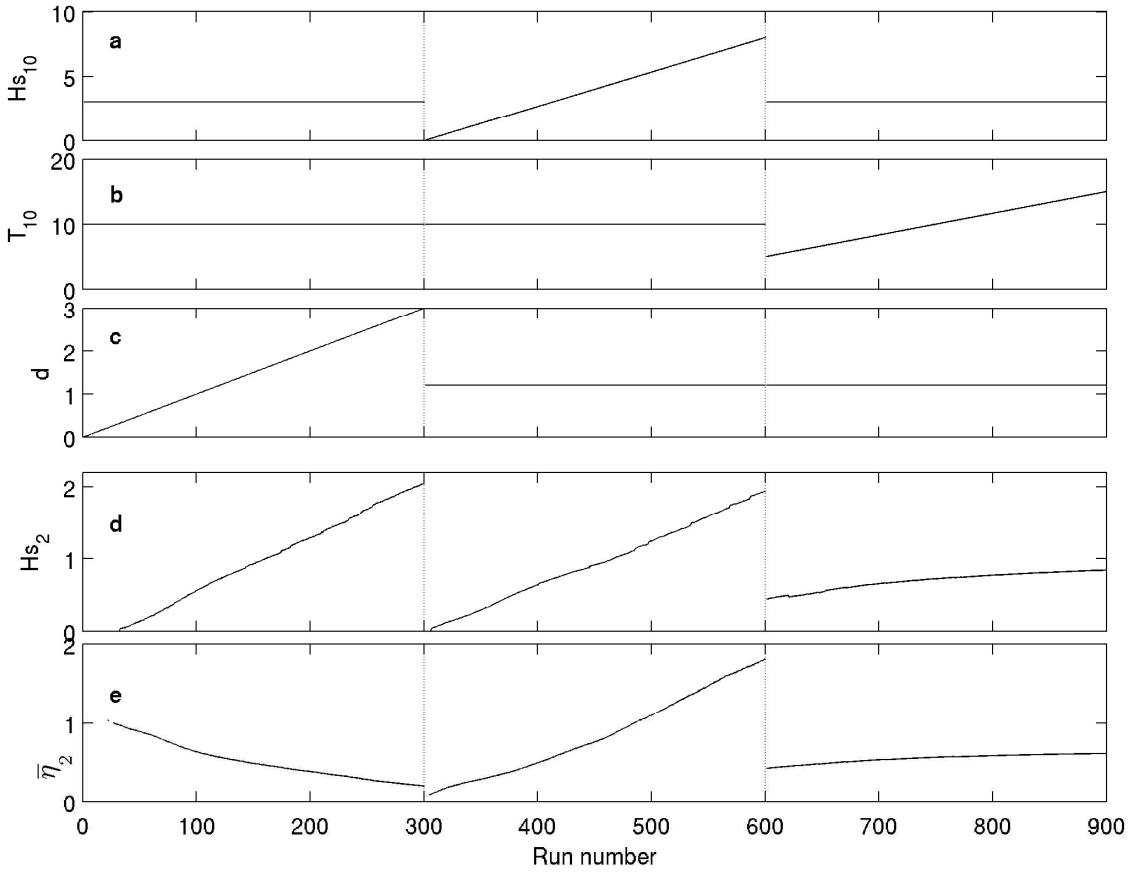

Figure 2.9: Results of the numerical integration of equations (2.6) to (2.9) showing the effect of an independent linear increase in three of the input variables. With all the other input variables remaining constant (values detailed in Table 2.2 "Indep. Increase"), a) incident wave height, b) incident wave period, and c) water level are separately increased as shown and results in changes in d) SS significant wave height H_{s2} and e) setup $\overline{\eta_2}$ at the inner fore reef.

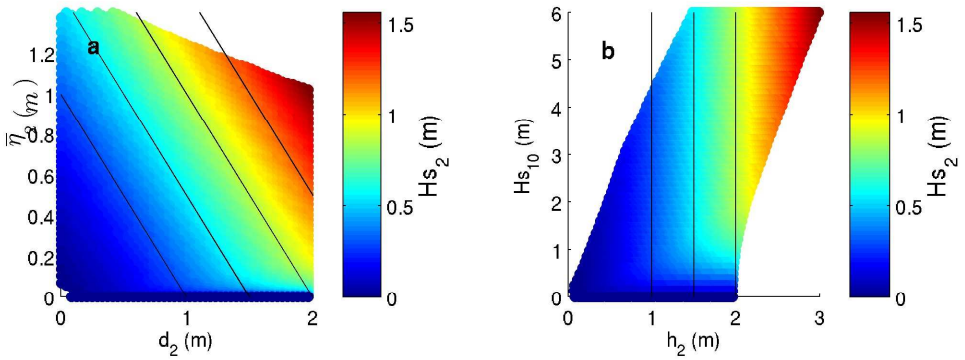

Figure 2.10: Effect of co-varying incident wave height and water level on SS significant wave height near the shore (Hs_2) computed from equations (2.6) to (2.9) using parameters and input variables summarized in Table 2.2 (co-varying). a) Hs_2 as a function of tidal level d and setup $\overline{\eta}_2$ on the reef. b) Hs_2 as a function of total depth on the reef h_2 and incident significant wave height Hs_{10}. Black lines are line of equal water depth on the reef.

Chapter 3

Forcing of resonant modes on a fringing reef during tropical storm Man-Yi

This chapter is adapted from:
Péquignet, A. C. N., J. M. Becker, M A. Merrifield, and J. Aucan (2009), Forcing of resonant modes on a fringing reef during tropical storm Man-Yi, *Geophys. Res. Lett.*, 36, L03607, doi:10.1029/2008GL036259.

3.1 Introduction

Fringing reefs provide natural protection for tropical island shorelines by efficiently dissipating sea and swell energy (Munk and Sargent 1948, Hardy and Young 1996, Hearn 1999). During large wave events, however, significant coastal inundation may occur. For example, large and variable wave overwash during typhoon Russ was reported by Jaffe and Richmond (1993) in Guam. While a variety of field studies have measured wave transformation over fringing reefs during moderate wave conditions (e.g. Young 1989, Hardy and Young 1996), few have captured the response of the reef to large wave events. The focus of the Pacific Island Land-Ocean Typhoon (PILOT) project is to assess the amount of wave energy reaching the shore of reef-fringed islands during large wave events. A cross-shore array of pressure sensors and current meters has been maintained at

Ipan reef, Guam for more than three years, covering a variety of wave conditions. The focus of the present study is the response of the reef to the large wave event associated with tropical storm Man-Yi.

Previous studies of wave transformation on fringing reefs have shown that the energy spectrum on reef flats is dominated by motions at infragravity frequencies (e.g. Young 1989, Hardy and Young 1996, Brander *et al*. 2004). Lugo-Fernández *et al*. (1998) have suggested that part of the low frequency variability observed at Tague Reef, St. Croix, USVI is related to the fundamental (1/4 wavelength) resonant mode. Open basin resonant modes at tidal frequencies have been well documented on coastal shelves (e.g. Huthnance 1980, Giese *et al*. 1990). For typical fringing reef topography (Steers and Stoddard 1977) however, estimates of resonant periods are the order of tens of minutes and fall outside of the energetic part of the wave spectrum. For example, approximating the reef at Ipan as a step shelf with length L=450m and water depth h=0.5m, the fundamental resonant period $T_0 = 4L/\sqrt{gh}$ $T_0 = 4L/\sqrt{gh}$ is approximately 13 minutes. During Man-Yi, however, wave setup increased the water level on the reef to h=2m reducing the resonant period by a factor of two.

We report here field observations of the low frequency, near resonant oscillations that dominated the variance of sea surface elevation at the shoreline of Ipan reef at the peak of tropical storm Man-Yi and analyze the conditions that favored their excitation. In section 3.2, we describe the experimental setting and wave energy on the reef. In section 3.3, we compare the empirical orthogonal modes and the spectral structures of the oscillations

observed on the reef with the theoretical spatial and temporal structure of open basin normal modes. In section 3.4, we demonstrate that the narrow bandedness of the swell generated by Man-Yi provided near resonant forcing for those normal modes. Finally, we summarize our results in section 3.5.

3.2 Field site and data

The study site at Ipan (Figure 3.1a) is composed of a narrow sandy shore connected to a shallow (~0.5m) wide (~450m) fringing reef flat, which typifies the coastal morphology of many Pacific islands (Figure 3.1b). The rugose spur and groove reef face is very steep resulting in wave breaking typically confined to a narrow zone around the reef edge (Figure 3.1d). The deployment presented in this study consists of a bottom-mounted cross-shore array of 4 single pressure sensors and 2 collocated pressure sensors and acoustic current-meters (Figure 3.1b) sampling at 1 Hz, in bursts of 43180 seconds every 12 hours and 7200 seconds every 4 hours respectively. Sea surface elevations are derived from the pressure data and corrected for depth attenuation using linear wave theory. All spectral variables are estimated from two hour segments of de-trended and de-tided (least square fit using 5 dominant tidal constituents) time series, and are band averaged, yielding approximately 22 degrees of freedom and a spectral bandwidth of 0.0016 Hz. The data presented here were collected from June-July 2007 when offshore wave conditions at sensor 10 ranged from calm (significant wave height Hs<1m) to a typical moderate wave event (Hs=1-2m with periods between 7 and 12 seconds, 20-23 June), to an energetic wave event (Hs=4m, 12 second period, 9 July)

when tropical storm (later upgraded to typhoon) Man-Yi passed 200nm south of Guam. Although the direct impact of Man-Yi on Guam was not severe in terms of atmospheric pressure, winds and rain, significant wave-driven coastal inundation was observed along parts of the eastern side of the island. Consistent with in situ reports of inundation, the observed sea surface elevation near the shoreline (sensor 2) peaked at 2.06m (2% exceedance) during the event, which is nearly four times larger than the typical tidal range over the reef. The high water level at the shoreline is partially attributed to a 1.2 m rise in mean sea level caused by wave setup (Gourlay 1996) (Figure 3.2a**)**. This increase in water level across the reef, in turn, is responsible for an increase in low frequency wave energy reaching the shore.

During normal and storm conditions, waves at sea and swell periods (5 to 25 seconds) dominate the offshore energy spectrum, and largely dissipate at the reef face through breaking. Additional dissipation also is achieved on the reef flat through bottom friction (Lowe *et al*. 2005). Similar to dissipative sandy beaches (Guza *et al*. 1984, Ruggiero *et al*. 2004), shoreward of the surf zone at Ipan the water level fluctuations are dominated by low frequency waves (period of 25 to 1000 seconds). The amplitudes of the infragravity (0.005 to 0.04 Hz) and far infragravity (Oltman-Shay *et al*. 1989) (fIG) (0.001 to 0.005Hz) oscillations, although small in moderate wave conditions, increase both with the water level over the reef and the amplitude of the incident swell waves (not shown). During Man-Yi, the average amplitude of waves of periods ranging from minutes to tens of minutes reached approximately half a meter near the shore. While infragravity wave energy on the reef typically decays slightly in amplitude toward shore, presumably

in part due to frictional effects, anomalous amplification of the longest waves (fIG, period 200 to 1000 seconds) is observed during Man-Yi with the largest amplitude occurring at the shore (sensor 2).

3.3 Reflection and resonant modes

Infragravity energy reaching the shore must be either dissipated through breaking at the shoreline and friction or reflected (van Dongeren *et al*. 2007). We assess the reflection of IG waves on the reef flat by assuming normal incidence of shallow water waves and estimating the incoming (F^+) and outgoing (F^-) cross-shore energy fluxes (Sheremet *et al*. 2002) at sensor 6 from the auto-spectra of surface elevation $S_{\eta\eta}$ and of cross-shore velocity *u,* S_{uu}, and from the co-spectrum of η and *u,* $S_{u\eta}$

$$F^{\pm}(f) = \frac{1}{4}\sqrt{gh}[S_{\eta\eta}(f) + (h/g)S_{uu}(f) \pm (2\sqrt{h/g})S_{\eta u}(f)] \qquad (3.1)$$

The frequency dependent reflection coefficient of waves on the reef is defined as F^-/F^+. In general, we find that reflection (not shown) increases with increasing incident swell period and decreasing offshore wave height. fIG reflection is variable during calm to moderate wave conditions, and it reaches 100% during the peak of Man-Yi, indicating the presence of standing waves over the reef.

We next demonstrate that the shallow reef flat at Ipan acts as a bounded open basin that supports resonant modes of oscillations with an antinode of surface elevation at the shore

and a node at the reef edge. The resonant periods for a step shelf (reef) of width L, are given by

$$T_n = \frac{4L}{(2n+1)\sqrt{gh}} \qquad n=0,\ 1,\ 2..... \tag{3.2}$$

where h is the water depth on the shelf (assumed uniform) and g is the gravitational acceleration (Sorensen 2005). The cross-shore structure of the resonant modes of sea surface elevation is given by

$$A_n(x) = \cos\left[(2n+1)\frac{\pi}{2L}x\right] \quad n=0,\ 1,\ 2.... \tag{3.3}$$

where x is the cross-shore distance from the shoreline. Using mean water depth at sensor 2 in equation (3.2), we find the period of the fundamental mode at Ipan reef ranges from more than 1000 seconds to 416 seconds at the peak of the storm.

We perform an Empirical Orthogonal Function (EOF) analysis of the 2 hour segments of band pass filtered sea surface elevation time series across the reef. The band pass filter is designed to examine energy in the first 3 resonant frequencies (periods from 100 to 650 seconds during Man-Yi) as the spacing of the sensors on the reef is insufficient to resolve the spatial structure of higher modes. The cross shore structure of the first two empirical modes matches the structure of theoretical resonant modes (equation (3.3) n=0,1) during the storm (Figure 3.2b). These two EOF modes explain

75% and 23% of the fIG variance on the reef during Man-Yi but we emphasize that resonant modes are not observed during non storm conditions.

We next estimate the coherence spectra between the sea level elevation at sensor 2 and sensor 5 (Figure 3.3a) in the fIG band. In this band, the timing error estimates associated with instrument clock drift and synchronization have a negligible effect on our coherence estimates. The theoretical resonant frequencies (inverse of equation 3.2) of the first 3 modes (n=0, 1, 2) are superimposed on the coherence and co-spectra. Motions at frequencies at or around the theoretical values are highly coherent on the reef. The central frequency of the bands of high coherence closely follows the shift of resonant frequencies associated with rise and fall of the mean water depth on the reef (Figure 3.2d). High coherence is particularly pronounced during the large event when the absolute value of the co-spectrum (Figure 3.3b) between sensor 2 and 5 is high. The co-spectrum is organized in alternating bands of positive and negative values corresponding to phase shifts, from in phase (positive) to out of phase (negative), matching the theoretical phase of the corresponding resonant modes sampled between sensor 2 and sensor 5. The quadrature spectrum (not shown) at the resonant frequencies is near zero suggesting that the phasing between the surface elevation at the sensors is close to 0 or 180^{o}.

3.4 Near resonant forcing

Although motions around the resonant frequencies (equation 3.2) are highly coherent on the reef (Figure 3.3a), they are not necessarily energetic (Figure 3.3b) as forcing at or

near the resonant frequencies is necessary to excite these modes. We next examine the forcing at sensor 10 and its relationship to the reef response.

The excitation of motions at fIG frequencies may occur offshore (Herbers *et al*., 1994, 1995) or in the surf zone by the breaking of modulated short-waves, or wave groups (Symonds *et al.* 1982, Schäffer 1993, Janssen *et al*. 2003). The former mechanism is unlikely as during Man-Yi, the peak fIG energy at a period of 416 seconds (frequency of 0.0024Hz) is present in the spectrum of the inshore sea surface elevation S_{22}, but not in the spectrum of the offshore sea surface elevation $S_{10\text{-}10}$ (Figure 3.4a), and energy in this band is not coherent between the two sensors (Figure 3.4b).

To test that near resonance forcing occurs due to wave groups, we obtain the envelope of the offshore (sensor 10) sea surface elevation $\eta(t)$ by computing the slowly varying (low frequency) envelope function $E(t)$ (Longuet-Higgins 1984) as

$$E(t) = | \eta(t) + i \Gamma\{\eta(t)\} | \tag{3.4}$$

where $\Gamma\{\eta(t)\}$ denotes the Hilbert transform operator and $|\ |$ is the amplitude of the complex function. Figure 3.4a shows the spectrum of swell wave groups S_{env}, with modulation time scales commensurate with the frequencies of the resonant modes on the reef. In addition, a high coherence between the inshore fIG sea surface elevation S_{22} and the offshore swell wave envelope S_{env} exists (Figure 3.4b). We conclude that the fIG oscillations on the reef are driven by the modulation of breaking swell waves at the reef

edge, similar to a time-varying set-up. We also estimate the transfer function between the wave envelope and the inshore sea surface elevation (Figure 3.4c) as the ratio of the amplitude of the cross-spectrum between the two time-series, and the auto-spectra of the wave envelope (Emery and Thomson 1998). This transfer function shows a strong gain of energy near the fundamental resonant frequency, consistent with a near-resonant response on the reef to the envelope forcing.

3.5 Conclusion

The shelf topography of a fringing reef such as Ipan may support open basin normal modes. A cross-spectral analysis between sensors on the reef confirms that motions that match these normal modes retain high coherence and phase structure across the reef at very low wave energy. Forcing at the normal mode frequencies, however, is necessary to obtain resonant excitation and this condition of matching frequencies is rarely met at Ipan. During typical weak and moderate offshore wave conditions, the shallow water depth (~0.5m) on the reef sets the gravest resonant period to >13 minutes, falling in a non-energetic band of the wave spectrum. During the large wave conditions generated by Man-Yi, however, wave setup elevates water levels on the reef, lowering the resonant period by approximately a factor of two. During a four hour period of the deployment, we demonstrate that near resonant forcing of the open basin resonant modes occurs from the envelope of the incident sea and swell waves.

Previous studies have demonstrated that water level on the reef controls the frequency distribution and the amount of energy on the reef flat (e.g. Hardy and Young 1996, Hearn 1999, Brander *et al*. 2004). We find that the water level on the reef also alters the dynamics of wave transformation, allowing here for a resonant response to occur on the reef, which significantly increases the amount of energy that reaches the shoreline. When the water depth at Ipan is within the usual tidal range, we find that the infragravity energy decays slightly shoreward. In contrast, the unusually large water depth observed during Man-Yi from large wave setup over the reef results in the excitation of resonant modes with an antinode (maximum energy) at the shore line.

We conclude that any increase in water level on the reef will increase the resonant frequencies, which potentially will allow a wider range of wave conditions to excite reef resonant modes. With the prospect of sea level rise associated with global climate change (IPCC 2007), we speculate that the excitation of reef resonances may become increasingly important in the dynamics of coral reefs.

References

Brander, R. W., P. S. Kench, and D. Hart (2004), Spatial and temporal variations in wave characteristics across a reef platform, Warraber Island, Torres Strait, Australia, *Mar. Geol. 207*, 169-184.

Emery, W. J., and R. E. Thomson (1998), *Data Analysis Methods in Physical Oceanography*. Pergamon Elsevier Science, 400p.

Giese, G. S., D. C. Chapman, P. G. Black, and J. A. Fornshell (1990), Causation of Large-Amplitude Coastal Seiches on the Caribbean Coast of Puerto Rico, *J. Phys. Oceanogr*., *20***,** 1449–1458.

Gourlay, M. R (1996), Wave set-up on coral reefs. 2. Set-up on reefs with various profiles, *Coast. Eng*., *28*, 17-55.

Guza, R. T., E. B. Thornton, and R. A. Holman (1984), Swash on steep and shallow beaches, *Proc. 19th Coastal Engineering Conference*, Am. Soc. of Civ. Eng. Houston Tex., 708-723.

Hardy, T. A., and I. R. Young (1996), Field study of wave attenuation on an offshore coral reef, *J. Geophys. Res.*, *101*(C6), 14,311-14,326.

Hearn C.J. (1999), Wave-breaking hydrodynamics within coral reef systems and the effect of changing relative sea level*, J. Geophys. Res., 104* (C12): 30007-30019.

Herbers, T. H. C, S. Elgar, and R. T. Guza (1994), Infragravity-frequency (0.005-0.05Hz) motions on the shelf, I, Forced waves, *J. Phys. Oceanogr*., *24***,** 917-927.

Herbers, T. H. C., S. Elgar, R. T. Guza, and W. C. O'Reilly (1995), Infragravity-frequency (0.005-0.05Hz) motions on the shelf, I, Free waves, *J. Phys. Oceanogr*., *25***,** 1063-1079.

Huthnance, J. M. (1980), On shelf "resonance" with application to Brazilian M3 tides, *Deep-Sea Res., 27A***,** 347–366.

IPCC (2007)., Climate Change 2007, Synthesis Report. Contribution of Working Groups I, I, III to the Fourth Assessment Report of the Intergovernmental Panel on Climate [Core writing team, Pachauri R.K. & Reisinger A. (eds.)]. IPCC, Geneva, Switzerland, 104p.

Jaffe, B. E., and B. M. Richmond (1993), Overwash variability on the shoreline of Guam during Typhoon Russ, *Proc Seventh International Coral reef Symposium,* 1, Guam, 257-264.

Janssen, T. T., J. A. Battjes, and A. R. van Dongeren (2003), Long waves induced by short-wave groups over a sloping bottom, *J. Geophys. Res*., *108*, doi: 10:1029/2002JC001515.

Longuet-Higgins, M. S. (1984), Statistical properties of wave groups in a random sea state, *Phil. Trans. R. Soc. Lond.*, *312*.

Lowe, R. J., J. L. Falter, M. D. Bandet, G. Pawlak, M. J. Atkinson, S. G. Monismith, and J. R. Koseff (2005), Spectral wave dissipation over a barrier reef, *J. Geophys. Res.*, *110*, C04001, doi:10.1029/2004JC002711.

Lugo-Fernández, A., H. H. Roberts, W. J. Wiseman, Jr., and B. L. Carter (1998), Water level and currents of tidal and infragravity periods at Tague Reef, St. Croix (USVI), *Coral Reefs*, *17*, doi: 10.1007/s003380050137.

Munk, W. H., and M. C. Sargent (1948), Adjustment of Bikini atoll to ocean waves, *Trans. Am. Geophys. Union, 29*, 855-860

Oltman-Shay, J., P. A. Howd, and W.A. Birkemeier (1989), Shear instabilities of the mean longshore current, 2. Field data, *J. Geophys. Res*., *94*(C12), 18,031-18,042.

Ruggiero, P., R. A. Holman, and R. A. Beach (2004), Wave run-up on a high-energy dissipative beach. *J. Geophys. Res*., *109*, C06025, doi:10.1029/2003JC002160.

Schäffer, H. A. (1993), Infragravity waves induced by short-wave groups, *J. Fluid Mech. 247*, 551-588.

Sheremet, A., R. T. Guza, S. Elgar, and T. H. C. Herbers (2002), Observations of nearshore infragravity waves: Seaward and shoreward propagating components, *J. Geophys. Res*., *107*, doi:10:1029/2001JC000970.

Sorensen, R.M. (2005), *Basic Coastal Engineering* (3rd edition), Springer ISBN 0387233326.

Steers, J.A. and D. R. Stoddart (1977),The origin of fringing reefs, barrier reefs, and atolls, in *Biology and geology of Coral Reefs,* edited by O. A. Jones and R. Enden, pp. 21-57, Academic Press, New York.

Symonds, G., D. A. Huntley, and A. J. Bowen (1982), Two-Dimensional Surf Beat: Long Wave Generation by a Time-Varying Breakpoint, *J. Geophys. Res.*, *87*(C1), 492–498.

van Dongeren, A., J. Battjes, T. Janssen, J. van Noorloos, K. Steenhauer, G. Steenbergen, and A. Reniers (2007), Shoaling and shoreline dissipation of low-frequency waves, *J. Geophys. Res*., *112*, C02011, doi:10.1029/2006JC003701.

Young, I. R. (1989), Wave transformation over coral reefs, *J. Geophys. Res.*, *94*(C7), 9779-9789.

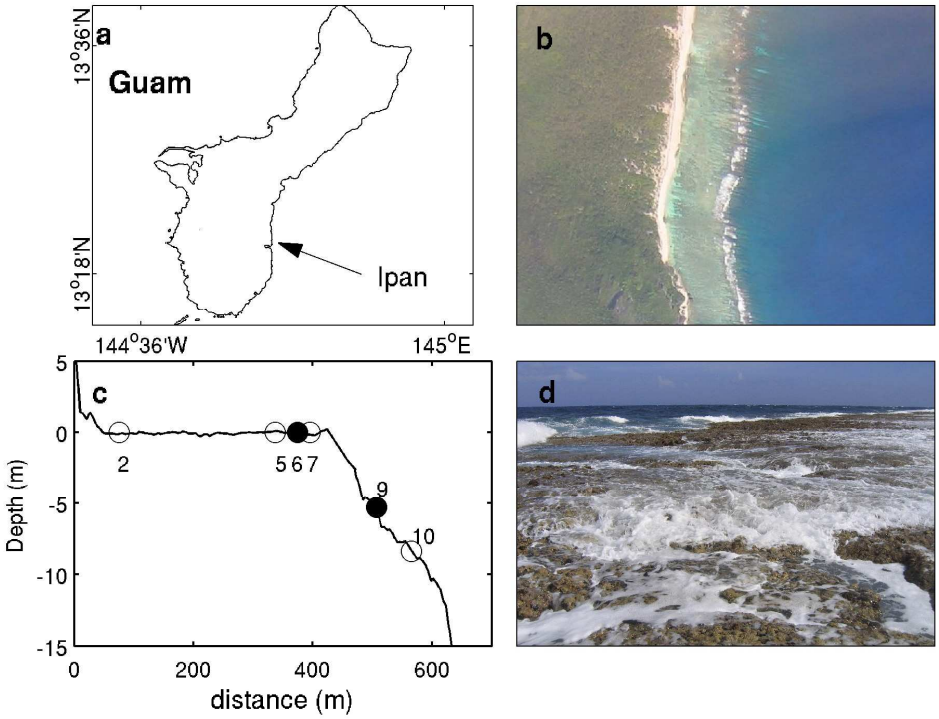

Figure 3.1: a) Location of the study site at Ipan reef on the southeast coast of Guam. b) Ikonos mosaic of Ipan reef, bounded at the shore with a narrow sandy beach and with white water marking the reef edge. c) Topography along the across-shore transect at Ipan reef with the location and number of the pressure (open circles) and collocated pressure and current-meter (solid circle) sensors. d) A view of the reef edge during weak wave and low water level conditions.

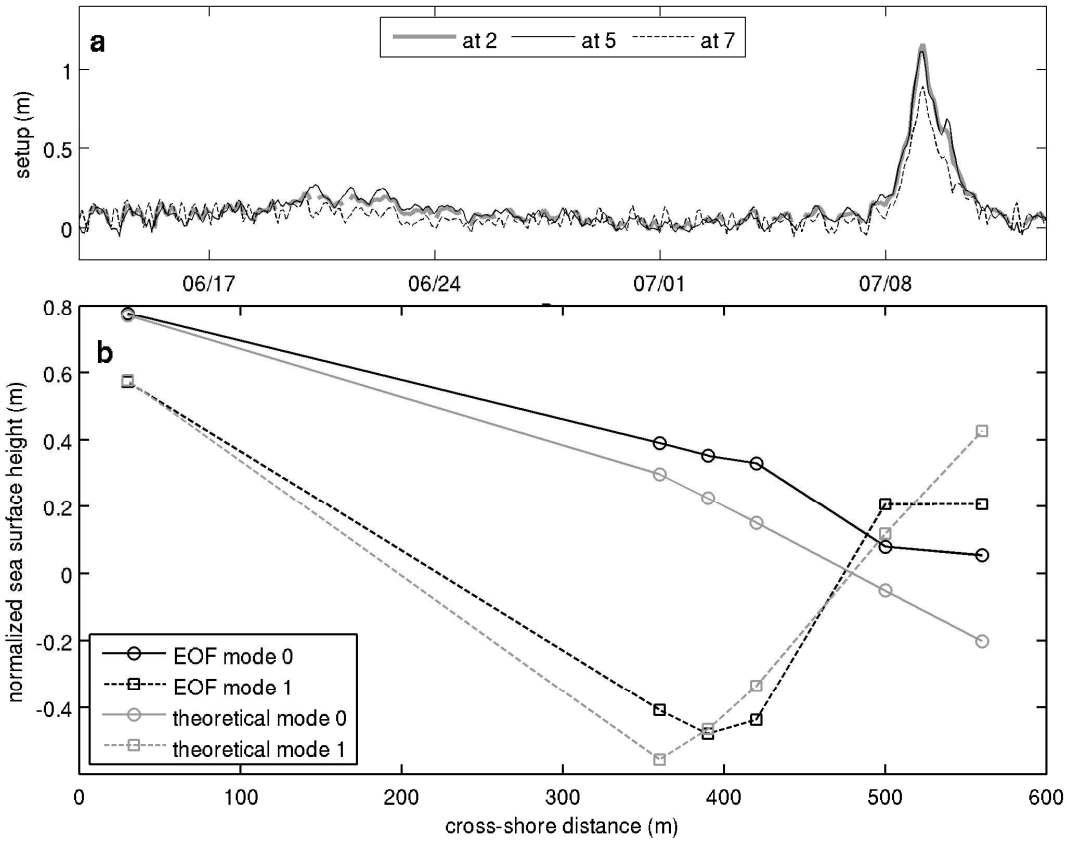

Figure 3.2: Temporal and spatial structure of the sea surface elevation on the reef. a) Setup at sensor 2, 5 and 7 as a function of time (15 minutes average). b) Cross-shore structure of the first two theoretical resonant modes from equation (3.3), with n=0, 1, at the sensor locations (grey). EOF mode of the band pass filtered sea surface elevation across the reef during the peak of Man-Yi (black).

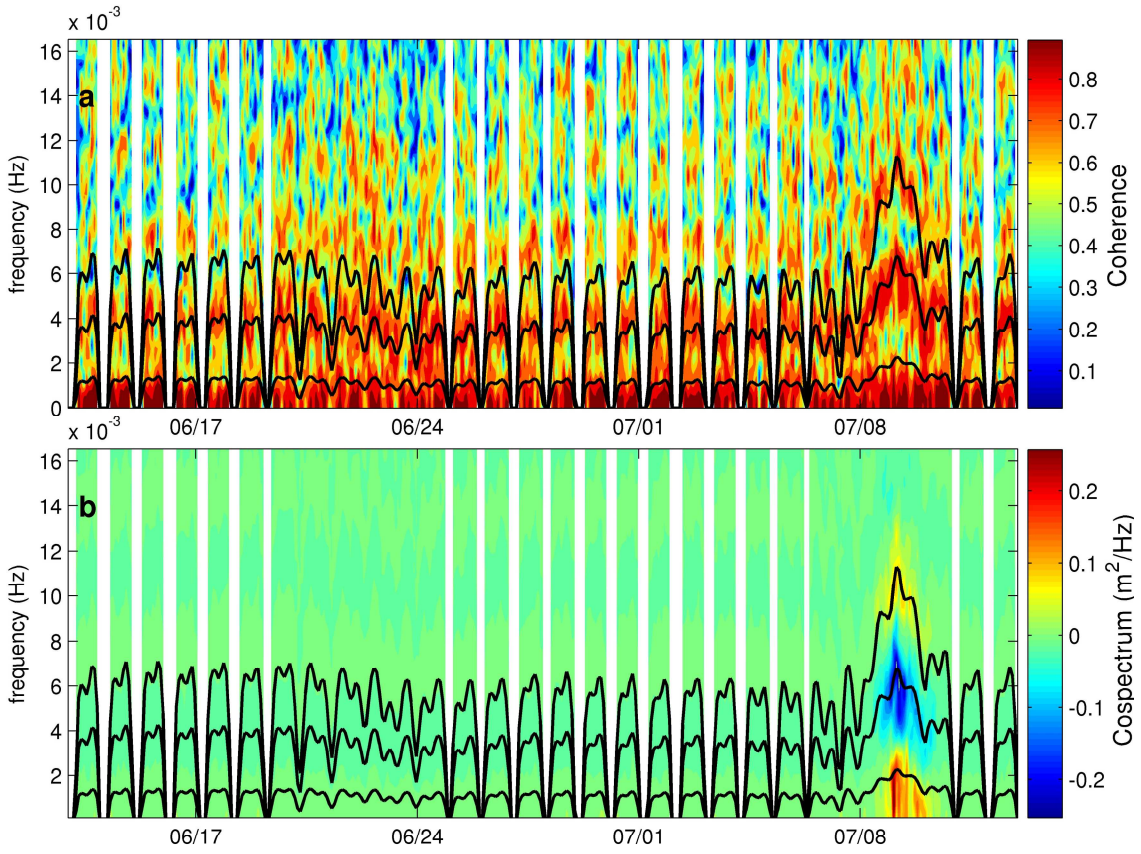

Figure 3.3: The coherence spectrum a) and the co-spectrum b) for sea surface elevation between the sensors closest to shore (2) and near the reef edge (5). Theoretical resonant mode frequencies based on equation (3.2) calculated from the mean water depth at sensor 2 (mode n=0, 1, 2) are overlaid on the spectra.

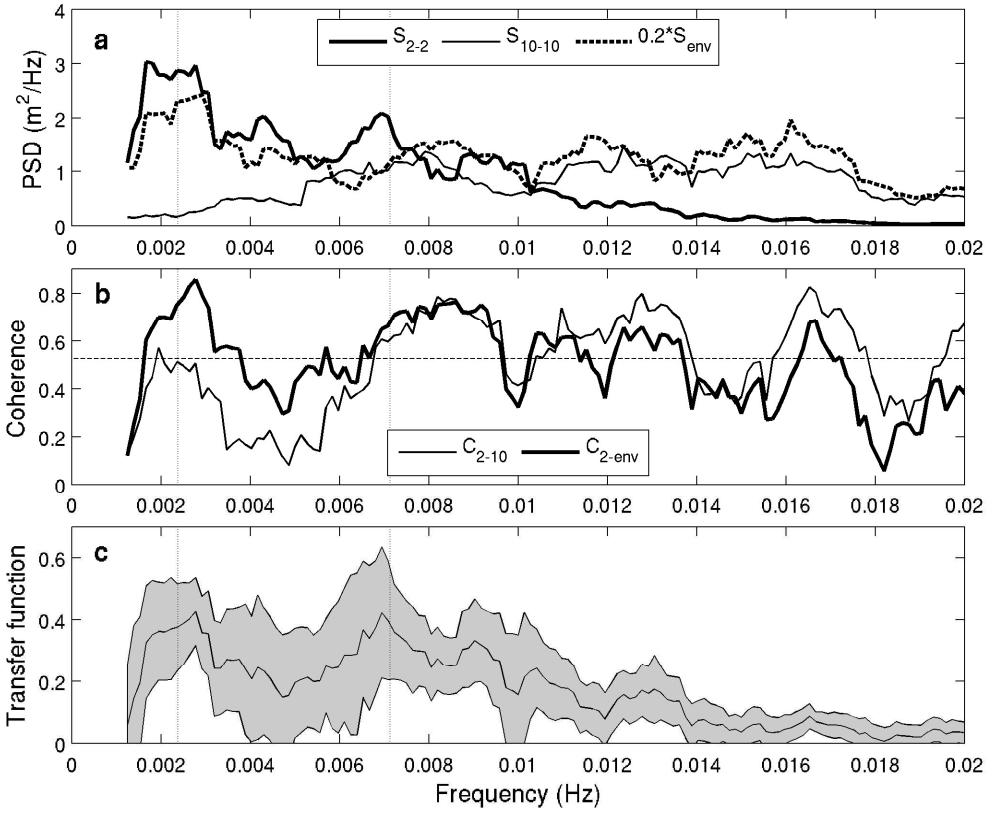

Figure 3.4: A comparison of auto and cross-spectra in the fIG and IG frequency bands during the peak of Man-Yi. (a) Autospectra of sea surface elevation at the most inshore sensor (S_{22}), the most offshore sensor ($S_{10\text{-}10}$) and the envelope of the swell band elevation at sensor 10 (S_{env}, scaled by 0.2). (b) The coherence spectra between the sea surface elevation at sensors 2 and 10 ($C_{2\text{-}10}$), and between the sea surface elevation at sensor 2 and the swell band envelope at sensor 10 ($C_{2\text{-}env}$). The dashed line is the 95% confidence level. (c) Transfer function between the swell band sea surface envelope at the most offshore sensor (env) and the sea surface elevation at the most inshore sensor (2). The vertical dotted lines show the first 2 theoretical resonant frequencies. The spectral resolution is 0.0014Hz. Shaded area shows the 95% confidence interval.

Chapter 4

Forcing of low frequency oscillations on a fringing reef, Ipan Guam

4.1 Introduction

Low frequency (LF) variability commonly occurs in the coastal ocean in the infragravity (IG) ($0.005 < f < 0.05$ Hz) and far infragravity (fIG) ($0.001 < f < 0.005$ Hz) frequency bands. IG waves have been linked to nearshore sediment transport (e.g., Beach and Sternberg 1987, Aagaard and Greenwood 1995, Aagaard and Greenwood 2008), coastal runup (e.g., Guza and Thornton 1982, Raubenheimer and Guza 1996, Ruggiero *et al*. 2004, Stockdon *et al*. 2006), harbor seiche (e.g., Okihiro *et al*. 1993, Harkins and Briggs 1994, Luick and Hinwood 2008), and ice shelf fractures (Bromirski *et al*. 2010). fIG oscillations have been associated with shear flows in the surf zone (Oltman-Shay *et al*. 1989, MacMahan *et al*. 2004), and resonant cross-shore standing waves on a fringing reef (Péquignet *et al*. 2009).

Munk (1949) and Tucker (1950) noted correlations between IG and sea and swell (SS) energy levels at a sandy beach, suggesting that IG fluctuations, or "surf beat", are generated by SS groups. In general, IG energy levels tend to be weaker in the deep ocean (Filloux *et al*. 1991, Uchiyama and McWilliams 2008) than near the coast (Guza and Thornton 1985, Oltman-Shay and Guza 1987, Okihiro *et al*. 1992, Webb *et al*. 1991),

consistent with nearshore generation and radiation to the deep ocean (Uchiyama and McWilliams 2008, Bromirski and Gerstoft 2009).

Two IG forcing mechanisms associated with SS waves have been identified: 1) nonlinear interactions that transfer energy from SS waves to bound and free IG waves, and 2) variable break point forcing in the surf zone. The first mechanism consists of quadratic difference interactions between waves in the SS frequency band (nominally 0.05 Hz < f < 0.5 Hz). Quadratic phase coupling of two SS waves with frequency f_1 and f_2 may result in a nonlinear triad interaction generating a third wave of sum (and difference) frequency $f_3 = f_1 \pm f_2$ and wave number $\kappa_3 = \kappa_1 \pm \kappa_2$. Although the primary waves satisfy the dispersion relationship, the resulting forced wave may not. In deep and intermediate water depths, the forced waves at the difference frequency do not satisfy the local dispersion relationship and the small amplitude forced or bound waves are phase-locked to the primary waves. The radiation stress gradient associated with the SS wave group (Longuet-Higgins and Stewart 1962, reviewed in Appendix A) acts as a forcing term for the forced second-order waves. For unidirectional wave trains, the resulting bound wave is 180° out of phase with the SS wave group (Figure 4.1).

Hasselmann (1962) used bispectral analysis of bottom pressure measurements to obtain a direct estimate of the second-order interactions in wave triads. Herbers *et al*. (1994) estimated bound wave energy levels by integrating bispectra (reviewed in Appendix B) over all wave pairs with difference frequencies in the infragravity band. He showed that the bound wave energy contribution to the IG spectrum increases quadratically with increasing incident SS wave energy.

As SS and forced bound waves propagate into shallow water, their growth rates are related. The one-dimensional, steady state equilibrium solution derived by Longuet-Higgins and Stewart (1962) for the forced bound wave of surface elevation (ς) and angular frequency (ω) on a flat bed of constant depth (h) is

$$\zeta(x,t) \approx -\frac{S_{xx}(x,t)}{\rho\omega^2 h^2} \tag{4.1}$$

where S_{xx} is the SS radiation stress, and ρ is water density. Assuming conservation of SS energy flux and normal incidence, $S_{xx} \sim h^{-1/2}$ and the bound wave solution grows as $\zeta \sim h^{-5/2}$ as $kh \to h^{-1/2}$. This approximation neglects the influence of sloping topography as well as dissipation due to breaking and bottom friction. For comparison, conservative shoaling of free LF waves follows $\zeta \sim h^{-1/4}$ (Green's law, Green 1837). Field observations from Elgar *et al*. (1992) and Ruessink (1998) showed that bound wave shoaling rates depart from the theoretical rate due to directional and finite depth effects but rates significantly greater than the free wave shoaling rate are associated with nonlinear difference interactions. Battjes *et al*. (2004) used laboratory experiments to evaluate IG shoaling rates over variable slopes and showed that this rate is frequency dependent and may be related to a normalized bed slope. Battjes *et al*. (2004) found that the $\varsigma \sim h^{-5/2}$ dependence is an upper limit that is only reached by long waves in the highest frequency range tested in their laboratory experiments; this was also noted by Madsen *et al*. (1997) using analytic solutions.

Janssen *et al*. (2003) (see also Battjes *et al*. 2004) showed that a phase shift away from 180° between the short wave group envelope and the bound forced waves occurs during the shoaling process for unidirectional waves on a sloping bottom with the bound waves lagging behind the incident wave group. This phase shift allows for the transfer of energy between the SS waves and the forced response (Masselink 1995, Janssen *et al*. 2003, van Dongeren *et al*. 2007). Battjes *et al*. (2004) describe both the frequency and spatial variation of the phase shift and show that the phase shift increases shoreward with decreasing depth. This allows for growth of the low frequency waves until breaking where the phase shift reaches 180° and a loss of energy shoreward of the breakpoint. The phase shift is observed to increase with long wave frequency and consequently the shoaling rates increase with frequency.

In shallow water, triad interactions approach resonance and the bound wave contribution to the IG energy spectrum peaks at the onset of wave breaking (Ruessink 1998). In addition, the bound wave now satisfies the shallow water wave dispersion relationship. In the surfzone, the high frequency sum waves are rapidly dissipated, but the difference IG waves often remain and may dominate the spectrum of the swash zone (e.g. Guza and Thornton 1982, Raubenheimer and Guza 1996, Ruggiero *et al*. 2004, Stockdon *et al*. 2006). IG waves may propagate as free waves towards shore (Herbers *et al*. 1995a) where they may reflect and radiate energy back to sea (Suhayda 1974, Guza and Thornton 1985, Elgar *et al*. 1994, Herbers *et al*. 1995a, Sheremet *et al*. 2002). Some low frequency energy also may be topographically trapped by refraction and remain along the shore as free edge waves (Bowen and Guza 1978, Oltman-Shay and Guza 1987, Bryan and Bowen 1996a, Bricker *et al*. 2007).

In addition to nonlinear wave-wave interactions, a second important mechanism for IG wave generation occurs in the surfzone due to the breaking of SS waves with variable amplitude, resulting in a spatially varying breakpoint and strong radiation stress gradient forcing. Solving the equations of motion with an idealized forcing term resulting from a sinusoidally varying breakpoint on plane and barred beaches, Symonds *et al*. (1982) and Symonds and Bowen (1984) demonstrated how a moving breakpoint generates free waves at the group frequency and its harmonics.

In the nearshore, both nonlinearly forced waves and breakpoint generated long waves may contribute to the IG field. Schaffer (1993) averaged the conservation equations for mass and momentum over a short wave period and obtained a forced second-order long wave equation in which the forcing is expressed in terms of the short wave radiation stress. The radiation stress is modeled using two approximations to the wave amplitude through the surfzone. The first assumes a breakpoint moving in response to the group with a wave amplitude decay in the surf zone solely dependent on local depth. This formulation does not allow for the transmission of the SS wave group inshore of the breakpoint. The second model assumes a fixed breakpoint and partial transmission of the SS wave group modulation inshore of the breakpoint. The first model results in breakpoint generated long waves while the second model accounts for the transmission of the bound long waves released at breaking. By solving the forced long wave equations with a combination of both forcing mechanisms, Schaffer (1993) showed that the two forcing mechanisms are the same order of magnitude and may work against each other, i.e., wave breaking may extract energy from incident bound waves. The

present study uses field data on a fringing reef to examine this interaction between the two forcing mechanisms in the generation of long waves on the reef flat.

Significant dissipation of IG waves has been reported in the nearshore both in field measurements (Sheremet *et al*. 2002, Henderson and Bowen 2002) and in laboratory experiments (e.g. Baldock *et al*. 2000, Battjes *et al*. 2004) with the energy loss attributed to both bottom friction and nonlinear transfer to higher frequency (Thomson *et al* 2006, Henderson and Bowen 2006, Baldock 2012). Quadratic bottom friction formulations have been evaluated for long waves (Henderson and Bowen 2002, van Dongeren *et al*. 2007), and the transfer of energy from IG to SS frequencies by triad interactions has been considered by Thomson *et al*. (2006) and Henderson *et al*. (2006). Recently Baldock (2012) argued that bound waves are not released as a result of short wave breaking but instead are dissipated through nonlinear interactions. Laboratory observations of the steepening of long wave fronts due to self-self interactions on a sloping beach and estimation of long wave dissipation using a short wave breaking parameterization suggest that wave breaking also may contribute to shallow water dissipation of IG oscillations at the shoreline (van Dongeren *et al*. 2007).

As a consequence of the strong dissipation of SS energy in the surfzone, swash zone oscillations on sandy beaches often are dominated by IG wave energy (e.g., Ruessink *et al*. 1998, Ruggiero *et al*. 2004, Senechal *et al*. 2010). However, swash oscillations are rarely reported at fIG frequencies in sandy beach surfzones and instead fIG (also referred to as very low frequency, VLF) energy has been associated with vortical motions with little surface elevation expression (i.e., these are not gravity wave motions) resulting from either the instability of longshore currents (Smith and Largier

1995) or rip currents (Haller and Dalrymple 2001). Energy density tends to be weaker at fIG than IG frequencies on sandy shores (e.g., Oltman-Shay *et al*. 1989, MacMahan *et al*. 2004).

Previous studies of wave hydrodynamics over reefs have focused on steady circulation (e.g., Symonds *et al*. 1995, Hearn 1999, Gourlay and Colleter 2005, Taebi *et al*. 2011), wave setup (e.g., Tait 1972, Gourlay 1996a, 1996b, Massel and Gourlay 2000, Vetter *et al*. 2010), and dissipation of wind waves by bottom friction (e.g., Nelson 1996, Lowe *et al*. 2005, Nunes and Pawlak 2008) and by wave breaking (Young 1989, Hardy and Young 1996, Lugo-Fernandez *et al*. 1998c, Hearn 1999, Péquignet *et al*. 2011). Observations of the cross-shore transformation of waves on reefs have shown a shoreward energy shift to low frequency (Hardy and Young 1996, Lugo-Fernandez *et al*. 1998c, Péquignet *et al*. 2011) and wave energy density at IG and fIG frequencies tends to exceed SS energy on reef flats (Lugo-Fernandez *et al*. 1998a, Péquignet *et al*. 2009).

Detailed studies of IG wave transformation across reefs with a steep fore reef attached to a reef flat (i.e., fringing reefs) have been limited to laboratory experiments (Demirbilek *et al*. 2007) and numerical simulations (e.g., Karunarathna and Tanimoto 1995, Nwogu and Demirbilek 2010, Sheremet *et al*. 2011). Laboratory experiments have been conducted for a range of fore reef slope angles (Nakaza and Hino 1991, Karunarathna and Tanimoto 1995, Demirbilek *et al*. 2007). The laboratory experiments show that the transformation of time-varying SS waves across reefs result in forcing on the reef flat of significant LF energy, at frequencies of the SS envelope.

Numerical simulations of long waves on reefs have been compared with laboratory results (Nakaza and Hino 1991, Karunarathna and Tanimoto 1995, Nwogu and

Demirbilek 2010, Sheremet *et al*. 2011). Both physical and numerical models show the spectral shift in wave energy shoreward, with low frequencies dominating the energy spectrum of the reef flat and the shoreline. Frequency selection of normal modes on the reef flat is observed in laboratory simulations and is qualitatively reproduced by numerical models. Analysis of cases with breaking and non breaking conditions highlights the dynamics of both bound wave and breakpoint forcing (Karunarathna and Tanimoto 1995). Earlier models use discretized versions of the conservation equations for mass and momentum, where the forcing of LF waves is provided by the SS radiation stress gradient (e.g. Nakaza and Hino 1991, Karunarathna and Tanimoto 1995). Recent efforts use more sophisticated deterministic (Nwogu and Demirbilek 2010, Sheremet *et al*. 2011) or stochastic models (Sheremet *et al*. 2011). Only one model comparison with field observations of LF waves on reefs has been reported to our knowledge (Roeber and Cheung 2012). The Boussinesq-type of model used by Roeber and Cheung (2012) reproduces reasonably well the shoaling and breaking of SS, and predicts the forcing of the reef normal modes qualitatively. Bottom friction appropriate for reef substrates has been included in various SS wave transformation modeling studies (e.g., Karunarathna and Tanimoto 1995, Demirbilek *et al*. 2007); however, the frictional decay of LF waves has received less attention.

Low frequency waves at IG and fIG frequencies have been observed to dominate the energy spectrum inside of the surfzone of both temperate shore platforms (Ogawa and Kench 2011) and coral reefs (Roberts *et al*. 1992, Kench 1998, Lugo-Fernandez *et al*. 1998, Péquignet *et al*. 2009). At fIG frequencies, standing modes have been observed across the Ipan reef flat during large wave conditions associated with tropical storm Man-

Yi. An increase in water depth due to wave setup promoted the establishment of the normal modes across the reef flat by increasing the fundamental mode frequency. At the peak of the tropical storm, oscillations of the SS wave group at the frequency of the fundamental modes resulted in forcing of fIG oscillations with amplitudes exceeding one meter on the reef flat.

In this chapter, new observations of wave transformation across the fringing reef at Ipan, Guam during energetic SS wave conditions are analyzed to understand the sources of LF energy observed on the reef flat, both in the IG and fIG bands. The availability of current meter and bottom pressure observations allows for direct estimates of the dominant terms in the LF energy conservation equations. The ability to track energy exchange between SS and IG/fIG motions allows for a detailed examination of LF generation and dissipation on a fringing reef. Section 4.2 describes the field experiment and section 4.3 details the methods used to analyze the field observations. The spectral characteristics and the forcing and dissipation of LF wave energy across Ipan reef are discussed in section 4.4. A summary and discussion are presented in section 4.5. Reviews of wave radiation stress and bispectral analysis are presented in appendix 4A and 4B, respectively.

4.2 The field experiment

Data used in this study were collected as part of the Pacific Island Land-Ocean Typhoon (PILOT) project, which is aimed at assessing coastal inundation at reef-fringed islands during large wave events. The study site at Ipan on the south shore of Guam (13 ^{o}

22’20”N, 144^{o} 46’30”E) has a wide (450m), shallow (1m) fringing reef (described in Péquignet *et al.* 2011).

A cross-shore array of wave and water level recorders has been maintained at Ipan since August 2005, with different sensors maintained at different locations across the reef flat and fore reef during the sequential deployments. The data used in this chapter were collected during September-October 2009 (during the N deployment). This section of data was chosen because it includes several energetic SS wave events, and the availability of current measurements across the reef allowed us to compute LF energy flux and energy conversion terms. Although the focus of this chapter is on one deployment, data from other deployments are included to show that the September-October 2009 data are representative of conditions at Ipan.

Nortek Aquadopp Acoustic Doppler Profilers (ADP) and Seabird SBE 26Plus wave and water level recorders were deployed across the reef, with two ADPs offshore of the reef crest and three on the reef flat (Figure 4.2). The ADPs sampled at 1 Hz in bursts of 3 hours every 4 hours. The SBE 26Plus sensors were deployed on the reef flat between the ADPs and one sensor was buried on land to measure atmospheric pressure and potentially, inundation. The Seabird sensors sampled at 1 Hz in bursts of 43,180 seconds every 12 hours. Sensor location and sampling details are summarized in Table 2.1. Pressure measurements are corrected for atmospheric pressure variations using the SBE 26Plus deployed on land (sensor atm P, Figure 4.2). Using linear wave theory, the sea surface elevation (η) is estimated from bottom pressure and the surface cross-shore (u, positive onshore) and longshore (v, positive toward the south) currents are estimated from the velocity measured near the middle of the water column. The estimated velocity noise

level for the 1Hz bin averaged horizontal velocity measurements is between 7.6 and 7.9 cm/s for the range of settings used. Changes in water temperature on the reef account for uncertainties of less than 0.2% in the estimation of sea surface elevation from the pressure observations. Using the pressure data, the times when the reef flat instruments were not submerged were flagged and are not considered in the present analysis. Offshore wave conditions are given by a Datawell directional wave buoy located 2.4 km southeast of the reef array (13^{o} 21'15"N, 144^{o} 47'18"E) at the 200 m isobath.

The incident significant wave height (H_s), peak period (T_p), and dominant wave direction are shown for the offshore buoy (30 minute average) and the most offshore fore reef sensor (15 minute average) in 8 m depth (Figure 4.3). Three energetic wave events (H_s > 3.5 m) occurred during the deployment: 14 September 2009 (maximum Hs=3.7 m with T_p~12 s, dominant direction ~60^{o} TN at the buoy), 2 October 2009 (maximum Hs=3.9 m, T_p~13.6 s, dominant direction~80^{o} TN), and 14 October 2009 (Hs=3.6 m, T_p~8.3 s, dominant direction ~90^{o}) (Figure 4.4). The events are representative of energetic wave events that occur ~4-8 times during the winter along the east coast of Guam. For all three events, the peak in wave height occurred at low tide (Figure 4.3a,e). Due to wave refraction, the incident wave direction at sensor 10 is within ± 10° of the 100° normal incidence for all the wave events (Figure 4.3c). The two first events are unaffected by meteorological conditions, as measured at the NOAA CO-OPS tide gauge station at Pago Bay located (13^{o} 25'4"N, 144^{o} 47'5"E), and incident waves are from a distant swell (Figure 4.3f). The 14 October 2009 event included some local wind forcing (Figure 4.3f), and the peak SS energy is at a higher frequency than the other storms

events (Figure 4.4). However the bandwidth of the SS peak (half power bandwidth ~0.01 Hz) is similar for the three events (Figure 4.3d).

The three events resulted in large wave setup on the reef flat, with setup at the most onshore sensor reaching 0.9 m during the 2 October 2009 event (Figure 4.5). In general, setup on the Ipan reef tends to scale as 0.35 times incident Hs on the fore reef (Vetter *et al*. 2010).

4.3 Methods

We next consider energy balances for IG and fIG variability at different locations across the reef. The energy equation for LF waves has been derived by Schaffer (1993) following Phillips (1977) by assuming a scale separation between energy in the LF and SS frequency bands. Hence, wave motions may be decomposed as $\eta = \eta' + \zeta$, $u = u' + U$ where the prime indicates the short wave component, and $\zeta = \overline{\eta}$ and $U = \overline{u}$ (overline notation denotes time average over a short wave period). The energy equation governing long waves is derived from the depth-integrated and time-averaged conservation equations of momentum and mass. For the case of longshore uniform ($\partial / \partial y = 0$), inviscid conditions, equation (3.7) of Schaffer (1993) becomes

$$\frac{\partial E}{\partial t} + \frac{\partial F}{\partial x} + U \frac{\partial S_{xx}}{\partial x} = 0 \qquad (4.2)$$

where S_{xx} is the cross-shore radiation stress, and the IG total energy E and cross-shore energy flux F are given by

$$E = \frac{1}{2}\rho(h+\zeta)U^2 + \frac{1}{2}\rho g\zeta^2 \tag{4.3a}$$

$$F = U(h+\zeta)(\frac{1}{2}\rho U^2 + \rho g\zeta) \tag{4.3b}$$

where g is the acceleration due to gravity. The last term in equation (4.2) is the conversion of energy between the high frequency SS motions and the LF waves. Dissipation is neglected in equation 4.2.

A similar long wave energy equation was derived by Henderson and Bowen (2002) and Henderson *et al*. (2006) in the frequency domain. A scale separation is not invoked and the energy equation is derived from the Fourier representation of the conservation equations yielding

$$\frac{\partial E(f)}{\partial t} + \frac{\partial F(f)}{\partial x} + W(f) + D(f) = 0 \tag{4.4}$$

where $E(f)$ and $F(f)$ are the total energy and the energy flux at frequency f, $W(f)$ is the nonlinear transfer of energy to f from other frequencies, and $D(f)$ is the rate of dissipation at f. For a longshore homogeneous, weakly nonlinear waves, Henderson *et al*. (2006) found,

$$E(f) = \frac{\rho}{2} S_{U,U}(f) + \frac{\rho g}{2h} S_{\zeta,\zeta}(f) \tag{4.5a}$$

$$F(f) = hC_{g\zeta,U}(f) + C_{g\zeta,M}(f) \tag{4.5b}$$

$$W(f) = C_{U,\partial S_{xx}/\partial x}(f) \tag{4.5c}$$

where $S_{X,X}(f)$ is the auto-spectrum of X at frequency f, and $C_{X,Y}(f)$ is the co-spectrum between X and Y. $M = \overline{\eta' u'}$ is the SS mass flux. With this convention, consistent with the notation used by Battjes *et al*. (2004) and Henderson and Bowen (2002), the nonlinear transfer term W (equation 4.5c) may be interpreted as the depth-integrated rate of work of the short wave radiation stress gradient on the LF water motion at frequency f.

The time series of η and surface currents are band-pass filtered over the SS frequency band to compute η', u' and M. Time series of terms quantifying the wave energetics are computed over 3-hour time spans. The cross-shore component of the radiation stress tensor (S_{xx}) is estimated for each ADP from (A4.4), where the SS energy, $E = 1/2\rho g A^2$, is calculated from the SS wave amplitude (A) following Battjes *et al*. (2004). The amplitude envelope of the SS waves, A, is computed from the Hilbert transform of the SS surface elevation time series (Janssen *et al*. 2003). The phase-averaged rate of energy transfer (equation 4.5c) between adjacent sensor locations j and $j-1$ is estimated from the co-spectrum of the radiation stress gradient, calculated using a finite difference between sensors, and a cross-shore component. The finite difference estimate will be evaluated in section 4.4.5.

Spectral quantities for E, F, and W (equation 4.5) are estimated from auto- and cross-spectral estimates involving ζ, U, M and S_{xx} based on Fourier transforms of detrended 3-hour data segments and band averaged using a Parzen spectral window yielding approximately 22 degrees of freedom and a spectral bandwidth of 0.0008 Hz. Phase spectra are considered when the coherence exceeds the 95% significance level of 0.5.

The LF dissipative term, $D(f)$ in equation 4.4, is calculated using the bottom friction parameterization of Thornton and Guza (1983),

$$< \varepsilon_f >= \rho C_f \frac{1}{16\sqrt{\pi}} \left(\frac{2\pi \overline{f}}{\sinh kh} \right)^3 H_{rms}^3 \qquad (4.6)$$

where h is the water depth, $\overline{f}$ is the peak frequency of the random wave field, k is the wave number associated with $\overline{f}$ given the water depth, and H_{rms} = 0.71 H_s is the root mean square LF wave height. The SS friction coefficients obtained in chapter 2 are used to specify the LF friction coefficients. On the fore reef (between sensors 10 and 9) the SS friction coefficient C_f = 0.2, and on the reef flat (between sensors 6 and 2) C_f = 0.06. Comparison of SS and LF frictional dissipation on the reef flat is discussed in section 4.4.5 with the choice of LF friction coefficient values.

Following Sheremet *et al*. (2002), shoreward (incoming) and seaward (outgoing) propagating LF waves are separated, with incoming (+ superscript) and outgoing (-) sea surface elevation and cross-shore velocity components estimated as

$$\eta^{\pm} = \frac{1}{2}(\eta \pm u\sqrt{h/g} \tag{4.7a}$$

$$u^{\pm} = \frac{1}{2}(\eta\sqrt{g/h} \pm u). \tag{4.7b}$$

This decomposition assumes shallow water waves and normal incidence, the validity of which will be discussed in section 4.4. The corresponding onshore and offshore energy flux densities at frequency *f* are

$$F^{\pm}(f,x_j) = \frac{1}{4}c_g(f,x_j)\left(S_{\eta,\eta}(f,x_j) + (h/g)S_{u,u}(f,x_j) \pm 2\sqrt{h/g}C_{\eta,u}(f,x_j)\right) \tag{4.8}$$

where $c_g(f,x_j)$ is the local group velocity.

The radiation stress gradient occurs in the nonlinear transfer term of Henderson *et al*. (2006) and equation (4.5c) and warrants further discussion. The radiation stress is proportional to and in phase with the short wave energy envelope (A4.4) and, in water of constant depth, the radiation gradient resulting from the SS wave group also is in phase with the SS wave group envelope and the resulting bound wave (equation 4.1) is 180° out of phase with the short wave group (Figure 4.1). The formulation of the nonlinear transfer term (4.5c) explains how the phase shift between forced bound waves and the SS wave group on a sloping bottom allows for energy transfer. A small departure from the 180° phase makes *W* non-zero and negative, and energy is transferred from the low frequencies to the SS frequency band. The decomposition of the long waves into an incoming and an outgoing signal (equation 4.7) allows the consideration of progressive

waves. The transfer term (equation 4.5c) is defined in terms of cross-shore velocity of the long waves which, for progressive waves is in phase with η. Hence, the sign of the transfer term (equation 4.5c) depends on the phase of the radiation stress gradient with the incoming or outgoing sea surface elevation, and energy is transferred when the phase of the cross-shore velocity or the sea surface elevation with the radiation stress gradient departs from 180^o.

Herbers and Burton (1997) examined the shoaling of surface gravity waves on a gently sloping beach and derived a second-order stochastic formulation of the Boussinesq wave equations for directionally spread shoaling waves. With the assumption that coupling between quartets is weak, they derived the cross-shore evolution of the frequency and alongshore wave number spectrum and bispectrum and demonstrated how energy flux divergence is related to the imaginary part of the sea surface elevation bispectrum. If the primary wave directional spreading is negligible (Norheim and Herbers, 1998), and energy flux may be written as $F = c_g E$ where $c_g = \sqrt{gh}$ is the shallow water wave group velocity, and $E(f) = \rho g S_{\eta,\eta}(f)$, this relationship is expressed by

$$\frac{d}{dx}F(f) = \frac{3\pi f}{h}\rho g \int_{=\infty}^{\infty} \mathrm{Im}\{B(f', f - f')\}df' \tag{4.9}$$

Next, we present the LF waves across Ipan reef in terms of the energy flux balance. The cross-shore changes in energy flux are related to the sea surface bispectrum in section 4.4.3.

4.4 Results

4.4.1 LF and SS wave energy across the reef

Wave energy transformation across Ipan reef is strongly frequency dependent (Figure 2.4). Between the fore reef (sensor 9) and the reef flat (sensors 2, 4, 6), SS energy is reduced by 90 to 97%, mostly due to wave breaking at the reef crest with some loss due to bottom friction (Péquignet *et al.* 2011). In addition the LF energy increases across the reef flat, particularly in the fIG band (Figure 4.6). The increase in the relative importance of LF compared to SS energy on the reef flat is similar to previous reef observations (e.g., Hardy and Young 1996, Péquignet *et al.* 2009, Péquignet *et al.* 2011), as well as to observations in the inner surf zone of dissipative sandy beaches (e.g., Raubenheimer *et al.* 1996, Ruggiero *et al.* 2004).

Frequency band averaged energy across the fIG, IG, and SS bands are compared at the fore reef (sensor 10) and inner reef (sensor 2) (Figure 4.7). The incident SS energy (Figure 4.7a) is almost one order of magnitude higher than the LF energy on the fore reef (Figure 4.7b) and reef flat (Figure 4.7c). The IG band averaged energy levels are 2 times higher at the fore reef than at the inner reef; however, the fIG levels are 4 times higher at the inner reef than at the fore reef (Figure 4.7b,c). Thus, even though the frequency averaged LF energy at the fore reef is comparable to the inner reef flat, IG energy dominates the fore reef while fIG energy dominates the inner reef flat.

Across the reef, both IG and fIG significant wave heights correlate with incident SS significant wave height (Figure 4.8). On the fore reef, IG wave heights increase nearly quadratically ($\sim Hs^{1.62\pm0.05}$) with incident SS wave height ($r^2=0.93$, $p<0.0001$) whereas fIG

wave heights increase linearly. The quadratic dependence in the IG band suggests the presence of bound wave energy resulting from second-order non linear interactions (Hasselmann 1962, Longuet-Higgins and Stewart 1962). Neither band shows wave height modulations due to tidal variations (Figure 4.8a,b). On the reef flat, both IG and fIG energies increase linearly with incident SS wave height (r^2_{IG}=0.85 r^2_{fIG}=0.74, $p<0.0001$) and the IG band displays weak variations at tidal frequencies (Figure 4.8c).

We consider the fIG and IG bands separately because of their distinct cross-shore variations (Figure 4.9). The shoreward growth of IG total energy (equation 4.3a) on the fore reef is followed by a sharp decay at the reef crest, where SS wave breaking occurs (Péquignet *et al*. 2011), and moderate decay on the reef flat (Figure 4.9). The shoreward growth of fIG total energy is less pronounced over the fore reef than the increase of IG total energy; however in contrast to the IG energy, fIG energy increases throughout the surf zone. fIG energy decay is weak on the reef flat (between sensors 4 and 2). During the 14 September and 15 October events there is additional fIG decay between sensors 6 and 4 on the outer reef. Bottom friction dissipation largely accounts for the decay of SS waves on the reef flat (Péquignet *et al*. 2011, Lowe *et al*. 2005). We will consider the corresponding frictional decay of LF energy in section 4.4.5.

Following Elgar *et al*. (1992) and Ruessink (1998), we consider whether observed changes in IG and fIG energy with depth are indicative of freely propagating or bound LF waves. We consider the ratios of total energy in the IG and fIG bands on the fore reef at 5.5m depth (sensor 9) divided by the energy at 8.2m depth (sensor 10). For freely propagating waves that conserve energy flux, the energy ratio is proportional to

$\left(h_9/h_{10}\right)^{-1/2}$ (Green 1837). For forced waves bound to shoaling unidirectional, normally incident shoaling SS waves, the theoretical energy ratio is proportional to $\left(h_9/h_{10}\right)^{-5}$ (Longuet-Higgins and Stewart 1962).

We consider incoming (+) and outgoing (-) energy ratios over the fore reef between sensors 10 and 9. In all cases, the observed ratios are closer to the free wave than the bound wave limit (Figure 4.10a). The incoming IG energy stands apart, however, with a dependence that is significantly higher than the free wave limit with a power law dependence of k = -1.94±0.04 (error represents the 95% confidence interval). Thus, the IG energy increase with decreasing depth is larger than expected for free wave shoaling but less than the theoretical maximum rate for bound wave shoaling (Figure 4.10a). We interpret this as the existence of a combination of incident free and bound IG waves over the fore reef, and that bound waves dominate the incident energy for IG waves but not for fIG waves.

4.4.2 LF energy flux across the reef

We next examine the nature of the LF energy across the reef. As shown in Figure 4.6, LF energy on the fore reef (sensors 9 and 10) peaks in the IG band, whereas energy on the reef flat (sensors 2 to 6) peaks in the fIG band. The distinction between the fIG and IG bands was introduced by Oltman-Shay *et al*. (1989) to differentiate between shear waves in the fIG band, caused by instabilities of longshore current shear, and gravity waves in the IG band. It is unlikely that the observed fIG energy on the reef flat is due to shear instabilities. The mean longshore current component is weak (< 0.05 m/s) on the reef flat

and fore reef at Ipan with little indication of strong horizontal current shears linked to wave events. As a further test of whether shear waves are important at Ipan, we estimate the ratio between velocity and pressure variances in the fIG and IG energy bands. According to Lippmann *et al*. (1999), for shear waves with little sea surface expression, the ratio should be much greater than g/h. The ratio is ~ g/h during the three main wave events in both frequency bands, consistent with the observed variability resulting from gravity waves rather than shear waves.

In contrast to waves in the SS band at Ipan, which appear to dissipate on the reef with little reflected energy (Péquignet *et al*. 2011), outgoing wave energy is detected in the IG and fIG bands. On the fore reef (sensors 9 and 10), the phase between the cross-shore velocity and sea surface elevation at low frequencies is between 0 and 90°, suggesting the presence of partially standing waves (Figure 4.11a and b). On the reef flat, strong reflection and standing wave patterns only are observed at the shore, resulting in near zero net energy flux (Figure 4.11 c). In contrast, in the middle of the reef flat and near the reef crest, the phasing between sea surface elevation and cross-shore velocity suggests a dominant incoming cross-shore energy flux of waves at low frequencies.

The importance of outgoing LF wave energy also is apparent in the estimated band averaged energy fluxes across the reef (Figure 4.12). In general, integrated incoming energy fluxes are greater than or equal to the integrated outgoing energy fluxes at all locations for the three main events. At the shoreline, incoming and outgoing fluxes are equal, consistent with reflection at the boundary. In the IG band (Figure 4.12a), the incoming flux increases over the fore reef at sensor 9. The incident IG flux then decreases rapidly in the surf zone (sensors 9 to 6), and more slowly over the reef flat

(sensors 6 to 2). Upon reflection at the shoreline, the outgoing IG flux continues to decay over the reef flat. Growth of IG energy flux across the reef crest results in a peak of outgoing IG energy flux on the fore reef (sensor 9) followed by a slight decay to sensor 10. This large outgoing flux appears to be due to reflection of incident energy and/or generation of outgoing IG energy on the fore reef.

In the fIG band, the incident energy flux increases across the fore reef and reef crest, peaking at sensor 6 just shoreward of the surfzone during the 14 Sep and 14 Oct events, and at sensor 4 during the more energetic 2 Oct event. It appears that fIG energy flux increases across the surfzone, presumably because the surfzone extends past sensor 6 for the 2 Oct event. The incident fIG flux decays over the reef flat between sensors 4 and 2. The outgoing flux is large across the reef during the 2 Oct event, with a weak maximum at sensor 6 just shoreward of the reef crest. The outgoing fIG flux shows weak maximum at sensor 6 during the 14 Oct event, and at sensor 10 during the 14 Sept event.

We compute the ratio of offshore to onshore energy flux $R^2(f,x_j) = F^-(f,x_j)/F^+(f,x_j)$ at each ADP during times when all sensors on the reef are submerged. At the most offshore sensor (Figure 4.13b), this ratio is ≥ 1 in the fIG band, decreases with increasing frequency from ~ 1 to 0.2 across the IG band, and is $\leq$ 0.1 in the SS band. The outgoing LF energy flux increases offshore of the surf zone and reef crest (Figure 4.12), suggesting the importance of local generation of LF energy and offshore radiation, as well as the reflection of incident LF energy at the fore reef. Theoretical considerations suggest that long wave reflection on an idealized smooth step topography (Kajiura 1961), in this case on the fore reef (Figure 4.13a), should increase with decreasing frequencies, in general agreement with the observed R^2 values. When

R^2 is interpreted as an estimate of reflected wave energy, a positive bias error results due to departures from normal incidence. In addition, as shown by Huntley *et al*. (1999), the possible error introduced by noise in the data and the subsequent decrease of coherence between sea surface elevation and velocity also will introduce a positive bias in this estimate. R^2 values that significantly exceed the theoretical curve may indicate frequencies where local generation of fIG and IG energy occurs. The spectral dependence of the reflection coefficient (Figure 4.12) is similar to previous results reported at Duck, North Carolina in 13m of water (Elgar *et al*. 1994).

We have described the LF energy over the Ipan reef primarily in terms of cross-shore fluxes, which are 4 times larger than longshore flux components. Observations on the fore reef (sensor 9) and on the reef flat (sensors 6, 4 and 2) at Ipan show that the phase relationship between ζ and U is consistent with the presence of partial standing waves in the cross-shore (Figure 4.11). In particular, we see little indication for coherent edge wave variability in either the fIG or IG bands. The lack of significant coherence between ζ and V, both on the fore reef and the reef flat (not shown), suggests that edge waves are weak. We conclude that the LF energy is comprised primarily of cross-shore waves, similar to leaky gravity modes (Oltman-Shay and Guza 1987).

Because forced IG waves vary with the incoming SS group (assuming narrow directional spread), spectral estimates of the envelope of the SS sea surface elevation on the fore reef (sensor 10) and the LF sea surface elevation on the fore reef (10) and inner reef flat (2) are compared (Figure 4.14). The auto spectrum of the SS envelope, S_{env}, is energetic in both the fIG and low frequency portion of the IG bands (Figure 4.14a). The high coherence (Figure 4.14b) and the nearly 180° phase difference (Figure 4.14c)

between the SS envelope and the sea surface elevation in the IG band provides further evidence that IG motions are primarily bound waves (Figure 4.14). In contrast on the reef flat, the energetic fIG variability is not significantly coherent with the reef flat SS envelope, suggesting that the LF oscillations are not bound waves. Bispectral analysis is next used to distinguish between free and forced LF waves.

4.4.3 Forced and free waves

Bispectral estimates have been used to demonstrate the existence of forced IG (bound) waves in pressure (Hasselmann *et al*. 1963) and sea surface elevation (Herbers *et al*. 1994) observations. Herbers *et al*. (1994) showed that bound waves (and harmonics of the primary waves) may be observed with biphase of 180° (0°), consistent with the theoretical phase locking of difference (and sum) interactions. A review of bispectral analysis is presented in appendix B. Here, we compute bispectra of the sea surface elevation for the array of pressure sensors deployed in Ipan for the 2 October 2009 event to assess the forced wave contributions in the LF bands. The bispectra for the two other energetic wave events (14 September and 14 October, not shown) exhibit similar patterns of bicoherence and biphase as the 2 October event. Hence, we consider the 2 October results to be representative of an energetic winter swell event at Ipan. Monte Carlo tests are used to evaluate the significance of the real and imaginary part of the bispectrum relative to signal with randomized phase. We consider bispectral amplitudes to be significant if they exceed the randomized phase bispectrum by 3 standard deviations.

At the most offshore sensor (10), both sum and difference-frequency interactions are detected from the real part of the bispectrum of sea surface elevation (Figure 4.15,

difference interactions zone B, sum interactions zone A). The difference-frequency interactions, with ~180° biphase, are observed for frequencies $f_1 \sim$ 0.075Hz and $f_3 = f_1 + f_2 \sim$ 0.087Hz, close to the SS band energy peak during the 2 October 2009 event, and $f_2 \sim$ 0.012Hz in the IG band. Sum interactions, with near 0° biphase, are observed for frequencies f_1 and f_2 close to the peak SS frequency (Figure 4.15 zone B), and $f_3 = f_1 + f_2 \sim$ 0.162 Hz near the first harmonic of the main SS peak visible in the power spectral density (Figure 4.15d). Difference interactions between SS harmonics ($f_1 \sim$ 0.15Hz and $f_3 = f_1 + f_2 \sim$ 0.162 Hz) and the forced IG waves ($f_2 \sim$ 0.012Hz) also contribute to the IG peak in the spectrum (Figure 4.15 zone C). The imaginary part of the bispectrum (Figure 4.15b) is related to the deviation of the biphase from 0/180° and is linked to the growth or decay of energy flux due to triad interactions (Norheim and Herbers, 1998), At sensor 10, the imaginary part of the bispectrum of the sum interaction is negative and consistent with decay of the harmonics on the fore reef. Bispectral results at sensor 9 are similar to sensor 10 (not shown).

Using equations (B4.5) and (B4.6) and the bispectral results in Figure 4.15, we estimate that the difference frequency interactions with nearly 180° biphase account for a significant fraction of the total energy in the IG band at sensor 10 (Figure 4.16). This implies that the IG energy is predominantly due to forced bound waves. A similar correspondence between estimated bound wave spectral energy and the observed IG band spectra occurs at sensor 9 (not shown). Difference interactions account for significantly less energy in the fIG band than the IG band, suggesting that fIG energy on the fore reef is not the result of nonlinear wave-wave interactions of the incident SS waves. Weak

bound wave energy in the fIG band also was reported by Herbers *et al*. (1995a) for observations at Duck, North Carolina.

For bound waves, the theoretical biphase for SS difference interactions over a flat bottom is 180°. For bottom pressure data in 13 m of water on the shelf of North Carolina, Herbers *et al*. (1994) attributed the observed scatter about 180° to noise in the bispectral estimate. For our observations in 8 to 5m, the deviation from 180° may also be the result of the shoaling process (equation 4.9). At sensors 9 and 10, the deviation of the biphase from 180° and the positive sign of the imaginary part of the bispectrum in the difference interaction domain (Figure 4.15 zone A) suggest that the IG energy flux increases over the fore reef due to the difference interactions (equation 4.9), consistent with Figure 4.12, presumably due to shoaling of the swell and bound IG waves. This increase was also noted in the change in total energy between 10 and 9 (Figure 4.10a).

On the reef flat at sensor 6 (inshore of the reef crest and main surf zone), the harmonics of the SS peak are no longer present in the sea surface elevation spectrum (Figure 4.17d), which we attribute to the strong SS dissipation through the surf zone. Given the weak SS energy levels, the bispectrum is much weaker on the reef flat than on the fore reef. The difference between the bispectrum of sea surface elevation at sensor 6 (Figure 4.17) and the bispectrum of a randomized phase signal is only twice the standard deviation of the randomized phase signal bispectrum (appendix B). The peak of the real part of the bispectrum at sensor 6 in zone A (Figure (4.17a) is lower frequency than the peak in the fore reef bispectra (Figure 4.15a). The interactions between components in the swell, IG and fIG peaks have a near zero biphase (Zone A on Figure 4.17), which we interpret as a weak remnant (i.e., SS energy is strongly dissipated at 6) of direct forcing

of LF energy in the surf zone, primarily in the fIG band, by SS wave groups, similar to a varying breakpoint forcing (Symonds *et al*. 1982, Symonds and Bowen 1984, Schaffer 1993). In contrast to the fore reef, where bound IG waves with biphase estimates of 180° are observed, difference interactions do not account for the fIG motions at sensor 6 (Figure 4.17c). We also note that the imaginary part of the bispectrum is negative in zone A at sensor 6, in contrast to the positive values in this zone on the fore reef (Figure 4.15b). This suggests energy decay in the fIG band at sensor 6, consistent with the decay of fIG energy over the reef flat onshore of sensor 6.

4.4.4 Generation and dissipation of LF wave energy

We next consider the energy equation (4.4) to assess IG and fIG energy generation and dissipation across the reef for two hour time series every three hours. We neglect the time derivative of total energy ($\partial E/\partial t$), which is estimated to be less than 0.01% of the energy flux divergence ($\partial F/\partial x$) term on the fore reef and the reef flat. The energy flux divergence, frictional dissipation (D), and nonlinear energy transfer (W) terms are estimated following the discussion of section 4.3.

Friction coefficients were estimated across Ipan reef for waves in the SS frequency band (Péquignet *et al*. 2011). Friction coefficient for the LF waves may differ from the SS values (Lowe *et al.* 2005). To assess how SS friction coefficients relate to the dissipation of LF waves, least squares estimates of the wave friction factor, C_f, on the reef flat based on the decrease in IG and fIG energy flux are compared to the estimate made in Chapter 2 for SS waves (Figure 4.18) on the reef flat between sensors 4 and 2 where the transfer term is found to be negligible (< 1% of $\partial F/\partial x$). The IG value $C_f = 0.065 \pm 0.004$

(95% confidence interval) is similar to the SS value of C_f = 0.06 ±0.02. Errors are estimated assuming independent measurements every 6 hours. The fIG estimate C_f = 0.027±0.002 is significantly smaller than the SS and IG band factors. In general, friction factor is expected to decrease with decreasing wave frequency given a constant roughness scale. The large IG friction coefficient, comparable to the SS friction coefficient on the reef flat, suggests that the dissipation of longer waves may result from the roughness at larger scale. Indeed on reefs, a single roughness scale is not representative of the roughness range and complexity observed (Zawada *et al* 2010, Nunes and Pawlak 2008, Jaramillo and Pawlak 2011). Although empirical relationships between roughness length and friction coefficient (i.e. Swart 1974) are unlikely to extend to the large scale of the low frequency waves considered here, estimation of a roughness scale associated with the LF friction coefficients predicted using these relations can suggest the scales that contribute to the dissipation of low frequency waves. For the IG band on the reef flat (sensors 4 and 6), drag coefficients would require length scales of 2-4m, comparable to, or greater than the depth. The decrease in friction coefficient for the longer fIG waves may indicate that roughness scales becomes limited at some point.

Based on the comparison of SS and LF friction factors on the reef flat, in the evaluation of the energy balance (equation 4.4) on the fore reef, we use the SS friction coefficients derived by Péquignet *et al*. (2011) for the IG band, and reduce the SS friction coefficients by a factor of two for the fIG band. Péquignet *et al*. (2011) did not estimate the SS friction factor for the reef crest, but based on visual estimates of the cross-shore changes in reef roughness, we consider the friction factor at the reef crest to be the

average of the values on the fore reef and on the reef flat, i.e., $C_f = 0.13$ for the IG band and 0.065 for the fIG band.

The energy equation 4.4 considers the balance between energy flux divergence, which can be positive or negative (Figure 4.12), dissipation which is always negative, and the transfer of energy between the SS and LF bands which can be positive or negative. The transfer term is measured by the co-spectrum of the radiation stress gradient and the LF cross-shore velocity (equation 4.5c). There is some subjectivity involved in specifying the cross-shore velocity due to appreciable changes in the LF velocity on the fore reef and across the reef crest. On the fore reef, the transfer term is estimated using the cross-shore velocity at sensor 9, which is more energetic than the velocity at sensor 10 as the LF waves shoal and which presumably has a higher signal to noise ratio. Similar results are obtained, however, using the average of the sensors 9 and 10 velocities. Across the reef crest, the energy flux increases between sensor 9 and 6 in the fIG band but decreases in the IG band. We use the observed fIG velocity at sensor 6 to compute the transfer term, because fIG energy largely is generated in the surf zone so that the sensor 6 provides a measure of the locally generated fIG wave energy. For the IG band across the reef crest, we use the IG velocity at sensor 9 to estimate the transfer term associated with the incident bound wave.

We next compare energy flux divergences to the transfer term and the frictional dissipation in an attempt to balance the energy equation in the IG and fIG bands (Figure 4.19). The frictional dissipation is estimated from equation 4.9 using the variable wave friction coefficient (C_f) across the reef (Figure 4.18). On the fore reef, a positive IG

energy flux divergence (increase in onshore flux between 9 and 10) is comparable to the transfer term, with dissipation playing a minor role (Figure 4.19a). Hence the increase in IG energy is drawn from the incident SS waves. The energy flux divergence is an order of magnitude weaker in the fIG than in the IG band, and about half as large as the transfer term (Figure 4.19c). Frictional dissipation accounts for at most a quarter of the difference between the flux divergence and transfer terms. The larger energy flux divergence in the IG compared to the fIG band is attributed to shoaling of incident bound wave energy at IG frequencies and of free waves in the fIG band.

Over the reef crest and through the surf zone, the negative IG flux divergence is balanced primarily by the transfer term (i.e., breaking swell working against the IG waves) and to a lesser extent by bottom friction (Figure 4.19b). The positive IG flux divergence over the fore reef is approximately equal to the negative flux divergence over the reef crest. For the fIG band, a weak, positive flux divergence is observed over the reef crest (similar to over the fore reef), and a strong positive transfer term is offset by frictional dissipation (Figure 4.19d). In summary, both IG and fIG energy fluxes experience growth on the fore reef. In the surfzone, across the reef crest, only the energy flux in fIG continues to grow while in the IG band it is reduced. The transfer of energy from low frequency to the SS band contributes significantly to the trends in energy flux divergence.

We examine the energy balances on the fore reef and reef crest further by considering the incoming and outgoing waves separately. Based on the estimated flux divergence across the reef (Figure 4.12), we assume that a portion of the incoming energy flux at sensor 9 reflects on the steep fore reef before reaching sensor 6. To account for

this loss of energy flux when evaluating incoming and outgoing energy flux balances separately, the theoretical solution of Kajiura is used to specify the reflected energy flux as $R^2_{theor}(f)F^+_{10}(f)$. This value is subtracted from incoming and outgoing fluxes at sensor 9 when evaluating equation 4.4 over the reef crest.

For the IG band, the energy flux divergence for incoming waves largely balances and is highly correlated with the combined transfer and dissipation terms on the fore reef ($r^2 = 0.98$, slope = 1.09, $p < 0.0001$) (Figure 4.20a) and on the reef crest ($r^2 = 0.91$, slope = 1.25, $p < 0.0001$) (Figure 4.20b). Likewise the outgoing energy flux divergence nearly balances the work and dissipation terms on the fore reef ($r^2 = 0.94$, slope = 1.33, $p < 0.0001$) (Figure 4.20c); however, a weak increase in outgoing energy over the reef crest is poorly balanced by an expected net energy loss due to the work and dissipation terms ($r^2 = -0.13$, slope = -0.26, $p = 0.37$) (Figure 4.20d).

For the fIG band, the energy flux divergence for incoming waves correlates with the combined work and dissipation terms on the fore reef ($r^2 = 0.93$, slope = 3.00, $p < 0.0001$) (Figure 4.21a) and on the reef crest ($r^2 = 0.96$, slope = 2.43, $p < 0.0001$) (Figure 4.21b). However, in both cases the fIG flux divergence is weaker than the work and dissipation estimates (slopes>1). The balances for the outgoing fIG wave energy are not conclusive over the reef crest ($r^2 = 0.38$, slope = 1.16, $p = 0.0028$) and fore reef ($r^2 =$ -0.27, slope = -0.03, $p = 0.079$) (Figure 4.21 c,d). The high uncertainty is due in part to the small number of frequency components used in the frequency integration for the fIG band compared to the IG band.

In general, we find the energy balance results for the total energy (Figure 4.19) and the incident energy (Figures 4.20 a,b and 4.21 a,b) encouraging given the number of

assumptions involved in the assessment. The results are less conclusive for the outgoing energy fluxes, which may result from the combination of local generation and reflection near the reef crest (Baldock *et al*. 2000). Consistent with laboratory experiments (Battjes *et al*. 2004), both forcing and dissipation of outgoing LF waves are observed in the surfzone (Figure 4.20 and 4.21) and the sign of the energy flux divergence varies with both frequency and cross-shore locations. The evaluation of the energy flux equation over large cross-shore intervals may not be adequate to represent these variations. Additional errors may be attributed in part to the assumptions made in our estimates of the transfer term (specification of LF cross-shore velocity), as well as the estimates of the energy fluxes and radiation stress across the steep reef crest. The energy flux balance equation (4.6) results from slowly varying, depth averaged equations (Longuet-Higgins and Stewart 1962, Henderson *et al*. 2006) and as discussed in Sheremet *et al*. (2011), the validity of these equations is questionable on a steep slope such as the fore reef at Ipan. In addition, the steep slope is a cavernous and porous spur and groove reef face, which may lead to energy flux dissipation that is not well-represented by the frictional estimates.

4.4.5 Comparison with conditions during tropical storm Man-Yi

During tropical storm Man-Yi, fIG cross-shore standing modes were observed on Ipan reef, which appear to have been resonantly forced by low frequency modulations of breaking waves during the peak of the swell event (Chapter 3, Péquignet *et al.* 2009). One measure of the standing pattern is the comparable fIG energy flux levels at the outer reef flat (sensor 6) of the incoming and outgoing waves, suggesting nearly complete

reflection and little energy loss as seen in Figure 4.22d. The standing modes are observed only in the fIG frequency band and during Man-Yi in the IG band, the incoming energy flux is more than a factor of two larger than the outgoing flux (Figure 4.22b). In contrast during the winter 2009 swell events, the amount of outgoing fIG and IG energy fluxes at the outer reef are more than a factor of 2 lower than the incoming fluxes (Figure 4.22 a,c). A standing wave pattern is not apparent.

The quasi-standing wave pattern during Man-Yi was in part due to high water level over the reef flat compared to the winter 2009 events. At the peak of Man-Yi, the total water depth on the reef flat was almost 0.5m deeper than at the peak of the largest winter 2009 event, due to large wave setup (Vetter *et al.* 2010) and tidal elevation. The peaks of the winter 2009 events tended to occur during low tides (Figure 4.3a,e). The 0.5m increase in reef flat water depth decreases the frictional dissipation by 50% during Man-Yi compared to the other wave events (see equation 4.6).

The increase in water depth during Man-Yi also leads to an increase in the normal mode frequencies of the reef flat. As the frequencies increase, they tend to fall into a more energetic part of the SS group forcing spectrum. For example, the high water depth during Man-Yi enabled excitation of the gravest standing mode (quarter wavelength), whereas the lower water levels during the 2 October 2009 event led to the excitation of the first mode (Figure 4.23 a,b). In addition, bottom friction is parametrized based on the resistance of a rough bottom to an oscillatory flow characterized by its orbital velocity. The fundamental mode has a node of velocity (antinode of surface elevation Figure 3.2) at the shore and has its greater velocities near the reef crest. In contrast, mode 1 has an antinode of velocity on the reef flat, hence frictional dissipation is expected to be higher

for mode 1 than mode 0. This would result in more fIG energy decay across the reef during the 2 October 2009 event (mode 1 dominant) relative to during Man-Yi (mode 0 dominant).

In general, the importance of normal mode generation in the fIG frequency band is evident in Figure 4.23. During the 2 October 2009 event, the transfer function between the SS envelope and the sea surface elevation near the shore (sensor 2) is large near mode 0; however the SS envelope energy is not particularly energetic at this frequency and so the nearshore elevation response is not maximum at the mode 0 frequency (Figure 4.23a). The SS envelope forcing and the nearshore sea surface elevation both peak near mode 1 (Figure 4.23a); however, the transfer of energy is less efficient than at mode 0 (Figure 4.23c). We attribute this to frequency dependent frictional dissipation during the event, due to relatively low water levels over the reef. In contrast, during Man-Yi the near resonant forcing and high water level led to mode zero generation (Figure 4.23b), which dominated the LF response on the reef. In the IG band, higher frequency normal modes exist, which presumably are inefficiently generated at Ipan due to the shallow depths and high frictional dissipation. The modal response in the fIG band further distinguishes it from the IG band. Both frictional dissipation and work of bound waves against the breakpoint forced waves favor the forcing of fIG rather than IG waves.

The resonant forcing of normal modes does not necessarily imply the largest sea surface elevation near the shore, which ultimately we are trying to assess as part of the PILOT goal of predicting wave-driven inundation. The LF elevation amplitudes at sensor 2 were slightly larger during the 2 October 2009 event than during the peak of

Man-Yi. The lower reef flat water level during 2 October 2009 event results in lower normal modes frequencies than during Man-Yi, with the two first modes falling in the fIG band in which bound waves contribution is negligible. In contrast during Man-Yi, the transfer of energy to modes with higher frequencies involves a larger contribution from bound waves and therefore a less efficient transfer of LF energy from the incoming SS envelope to the shoreline energy. Quantitative prediction of the LF water level response at the shore requires a more comprehensive modeling approach than considered here, which takes into account variable break-point forcing, incident bound IG energy, and frictional dissipation that varies with water level, frequency, and cross-shore position.

4.5 Summary and Conclusions

The first detailed field observations of long wave transformation across a fringing reef are used to examine forcing and dissipation of LF energy in the IG and fIG frequency bands. Nonlinear processes drive the low frequency oscillations observed at the Ipan shoreline, similar to the processes that result in the low frequency swash zone oscillations on sloping sandy beaches (e.g., Raubenheimer and Guza, 1996; Ruggiero *et al*. 2004). Bound IG waves (Longuet-Higgins et Stewart 1962), forced by nonlinear interactions between SS waves, dominate the low frequency spectrum seaward of the breakpoint. The evidence for bound waves includes: i) the quadratic dependence of the IG significant wave height on the incident SS significant wave height (Figure 4.8a), ii)

the higher rate of energy growth on the fore reef than predicted by shoaling free waves (Figure 10a), iii) the 180° phase relationship between IG band surface elevation and the envelope of the SS band energy (Figure 4.14), and iv) bispectral estimates on the fore reef that link IG energy with SS energy with 180° biphase (Figure 4.15), and that account for a significant fraction of the IG peak energy (Figure 4.16).

At the deepest sensor on the fore reef (sensor 10), separation of incoming and outgoing waves suggests an appreciable amount of outgoing energy flux (Figure 4.13). Theoretical reflection coefficients based on Kajiura (1961) are in reasonable agreement with observed ratio of outgoing to incident flux with values between 50-90%. The outgoing flux exceeds the incoming flux in the fIG band, and also is high in the IG band relative to the theoretical estimate, indicating that locally generated energy also radiates seaward from the reef.

Across the surfzone (at the reef crest), a strong radiation stress gradient results from the breaking of SS waves. The breakpoint at Ipan is confined near the reef crest (between sensors 9 and 6) (Péquignet *et al*. 2011) due to the steep topography of the fore reef. Breakpoint forcing at Ipan is characterized by temporal variations associated with the amplitude changes of the wave group. The surf zone is limited in width, typically located seaward of sensor 6, although during energetic swell events the zone may extend past sensor 6 (Figure 4.12).

The temporal variations of the radiation stress gradient generated by the breaking of SS wave groups across the reef crest work against the incoming bound IG waves, resulting in a decrease in IG energy flux (Figure 4.20a). This results in a net transfer of IG energy to SS frequencies with some energy dissipation due to bottom friction. A

similar energy transfer to high frequencies has been reported for sandy beaches (Henderson *et al*. 2006, Thomson *et al*. 2006). In the fIG frequency band, which exhibits little indication of bound wave energy, the time varying break point appears to generate the free fIG oscillations (Figure 4.21b) which dominate the spectrum on the reef flat (Figure 4.6). There also is fIG energy gain over the fore reef prior to breaking (Figure 4.21a), which we attribute to wave-wave interactions during the shoaling process. fIG motions tend to be prominent at the lowest normal mode frequencies for the shallow, wide Ipan reef flat.

Alternatively, the loss of IG energy flux across the reef crest may be understood following the time varying breakpoint hypothesis of Symonds *et al*. (1982). The incident bound waves result due to nonlinear difference interactions within the SS frequency band and the IG band, which generates phase-locked IG motions that are nearly 180° out of phase with the SS group as the waves approach the fore reef (Figure 4.24). Break point forcing may be interpreted as dynamic setup that generates fIG waves in phase with the SS wave group. Incoming bound waves and locally generated (by the time varying breakpoint) oscillations are near 180° out of phase, thus reducing the incident IG energy flux over the reef flat. While bound waves at fIG frequencies are weak at our most offshore sensor (Figure 4.16) fIG energy is observed in the SS envelope spectrum (Figure 4.23a). Breaking waves appear to directly force fIG oscillations on the reef flat through the modulation of the breaking wave heights (Figure 4.24)

The LF energy generated through breaking of SS waves at the reef crest results in some reflected energy at the shoreline, however, the outgoing energy flux at the outer reef flat is weak (Figure 4.12). The loss of energy flux across the reef flat, both incident

and outgoing (Figure 4.12), is attributed to frictional dissipation. Depending on the water level, frictional dissipation of 85 to 100% (50 to 100%) of the IG (fIG) energy flux is observed between sensor 6 and sensor 2. For the IG band, the inferred frictional wave factor is similar to that estimated from SS wave decay on the reef (Péquignet *et al*. 2011). In the fIG band, the frictional factor is reduced by a factor of two.

Observations of long wave transformation on reefs from laboratory studies also have shown the predominance of normal modes on the reef flat (Demirbilek *et al*. 2007, Nwogu and Demirbilek 2010). The forcing of the normal modes is reproduced by numerical models (Nwogu and Demirbilek 2010, Roeber and Cheung 2012), but the Boussinesq models appear to preferentially force the fundamental mode even when mode one dominates the energy spectrum in field data (Roeber and Cheung 2012). The correspondence of the frequency of the spectral energy on the reef flat and the peak frequency of the wave group is mentioned by Nwogu and Demirbilek (2010), but the forcing of modes higher than the gravest mode zero is not considered. Nonlinear triad interactions are investigated in Sheremet *et al*. (2011) based on laboratory experiments of long waves on steep reefs. They show that existing nonlinear (triad) spectral models may be used on the steep slopes of reef environments to reproduce both the growth and decay pattern observed in the IG band. These models will prove particularly useful to balance the energy flux equations at the reef crest where sensor resolution is strongly limited by the rough environment.

As a result of the reduction of bound IG energy and generation of fIG waves in the surfzone, LF energy at the Ipan shoreline has a spectral peak in the fIG band (Figure 4.6). The amplitude of IG on the reef flat is nearly linearly related to the incident wave height, with weaker amplitudes during lower tidal elevations, presumably due to enhanced frictional dissipation at low tides (Figure 4.8c). The dependence of fIG significant wave heights at the shore with incident wave height and water level shows more scatter than in the IG band (Figure 4.8c). The amplitude of the LF shoreline response depends not only on the SS envelope forcing amplitude but also its spectral structure and how it matches the normal mode frequencies. The shoreline IG energy may be predicted from the offshore SS wave height and the water level on the reef, which is given by the tide and the SS wave setup. However, without the detailed knowledge of the SS wave group spectrum, and correspondence with the normal modes frequency of the reef, only an upper estimate may be computed for the shoreline fIG energy.

The observations of excitation of the fundamental normal mode during tropical storm Man-Yi (Péquignet *et al*. 2009) and of a partially standing mode 1 during winter storms show the balance of the forcing of normal reef modes by short wave groups and the frictional dissipation on the reef. This balance is controlled by water depth on the reef and the projected increase of global sea level both will decrease frictional dissipation and favor the excitation of lower modes on fringing reefs like Ipan.

Appendix A: Radiation stress forcing

The concept of radiation stress was introduced by Longuet-Higgins and Stewart (1962, 1963, 1964) in analogy to electromagnetic waves and the "radiation pressure" they induce on surfaces. The radiation stress defines the excess of momentum flux due to the presence of waves.

For an undisturbed body of water of depth h and density ρ, the hydrostatic pressure p_0 is given at any point of vertical distance from the surface $(z=0)$ by $p_0 = -\rho g z$, where g is the acceleration due to gravity. The total flux of horizontal momentum across a vertical plane x=constant, between surface and bottom is $\int_{-h}^{0} p_0 dz$.

In the presence of a progressive, monochromatic, gravity wave with surface elevation $\eta = a\cos(kx + ly - \omega t)$ about the undisturbed surface z = 0 and corresponding horizontal velocity u, the total flux of horizontal momentum across the x=constant plane is given by $\int_{-h}^{\eta} (p + \rho u^2) dz$. The principal component (in the direction of wave propagation) of the radiation stress S_{xx} is defined as the mean value of the horizontal momentum flux associated with the wave minus the mean flux in the absence of the wave

$$S_{xx} = \overline{\int_{-h}^{\eta} (p + \rho u^2) dz} - \int_{-h}^{0} p_0 dz \qquad \text{(A4.1)}$$

where the overbar signifies a time average over a wave period. Similarly the transverse component of the radiation stress S_{yy} is defined from the y-momentum (momentum parallel to the wave crest) across a y=constant plane as

$$S_{yy} = \overline{\int_{-h}^{\eta} (p + \rho v^2) dz} - \int_{-h}^{0} p_0 dz \tag{A4.2}$$

where v is the transverse component of the velocity. The flux of x momentum across a y = constant plane, or equivalently y momentum across a x = constant plane ($S_{xy} = S_{yx}$) is

$$S_{xy} = \overline{\int_{-h}^{\eta} \rho uv dz} \,. \tag{A4.3}$$

For progressive linear waves, Longuet-Higgins and Stewart (1962) showed that the radiation stress tensor S is

$$S = E \begin{pmatrix} \dfrac{2kh}{\sinh 2kh} + \dfrac{1}{2} & 0 \\ 0 & \dfrac{kh}{\sinh 2kh} \end{pmatrix} \tag{A4.4}$$

where E is the SS total energy density.

Appendix B: Bispectral analysis applied to surface waves

Nonlinear energy exchange due to phased-coupled surface wave triads may be investigated through bispectral analysis. The following discussion follows Herbers *et al*. (1994).

A real, stationary signal *a (t)* with zero mean may be represented in Fourier-Stieljes form as

$$a(t) = \int_{-\infty}^{\infty} dA(f) e^{i 2\pi f t} \tag{B4.1}$$

where f is frequency, and t is time. The second-order power spectrum of the signal is defined as

$$S_{a,a}(f) = 2E[dA(f) dA(-f)] \tag{B4.2}$$

where $E[]$ is the expected value and $S_{a,a}(f)$ represents the contribution of the component A at frequency f to the variance of a. Similarly, the third-order bispectrum of x is defined as

$$B(f_1, f_2) = 2E[dA(f_1) dA(f_2) dA(-f_1 - f_2)] \tag{B4.3}$$

which provides a statistical measure of the phase coupling in triad interactions. If three waves at frequencies f_1, f_2 and $f_1 + f_2$ are statistically independent, the total phase of the three waves will be randomly distributed and averaging (denoted by the expected value) will result in a vanishing bispectrum. If the three components are nonlinearly coupled to each other, the sum phase is not random and statistical averaging will result in a nonzero bispectrum. Noting that $dA(f) = dA(-f)^*$, where * represents complex conjugation, equation (B4.3) shows that the bispectrum satisfies the following symmetry relations

$$B(f_1, f_2) = B(f_2, f_1) = B(-f_1, f_2)^* = B(-f_1 - f_2, f_2) = B(f_1, -f_1 - f_2) \qquad \text{(B4.4)}$$

With the Nyquist frequency (f_N) limit and the symmetry relations (B4.4), it may be shown that the non-redundant information in the bispectrum is restricted to the region defined by $0 \le l \le q/2$ and $l \le k \le q\text{-}l$ where q is the elemental bandwidth $q = f_N / \Delta f$

Bispectral estimates have large statistical uncertainties (Herbers and Sebert 1989, Herbers *et al*. 1994) and weak nonlinear coupling results in noisy bispectrum with biphase that is randomly distributed between -180° and 180°. High degrees of freedom and/or large nonlinear coupling are required to decrease the uncertainties and to have a stable biphase. In this chapter, the variance of the bispectral estimates is computed with a Monte Carlo simulation of the bispectrum of surrogate data computed from the original time series by the addition of a random phase. The bispectrum of the sea surface elevation is estimated for large wave events, following equation (B4.3), using averages over 50% overlapping segments (Subba Rao and Gabr 1984, Nikias and Raghuveer 1987).

Following Herbers *et al*. (1994) the forced wave spectral density $E_{forced}(\Delta f)$ is estimated from the integration of the bispectrum over all pairs with difference frequency Δf

$$b_i(\Delta f) = \frac{2\int_{\Delta f}^{\infty} df B(f, \Delta f)}{\left[2\int_{\Delta f}^{\infty} df E(f + \Delta f) E(f) E(\Delta f)\right]^{1/2}} \qquad \text{(B4.5)}$$

$$\frac{E_{forced}(\Delta f)}{E(\Delta f)} \approx \left| b_i(\Delta f) \right|^2 \qquad \text{(B4.6)}$$

References

Aagaard, T., and B. Greenwood (1995), Longshore and cross-shore suspended sediment transport at far infragravity frequencies in a barred environment, *Cont. Shelf Res*., 15, 1235-1249.

Aagaard, T., and B. Greenwood (2008), Infragravity wave contribution to surf zone sediment transport - the role of advection, *Mar. Geol*., 251, 1–14.

Baldock, T. E., D. A. Huntley, P. A. D. Birdand, T. J. O'Hare, and G. N. Bullock (2000), Breakpoint generated surf beat induced by bichromatic wave groups, *Coast. Eng*., 39, 213–242.

Baldock, T. E. (2012), Dissipation of incident forced long waves in the surf zone-Implications for the concept of "bound" wave release at short wave breaking, Coast. Eng. 60, 276-285, DOI: 10.1016/j.coastaleng.2011.11.002.

Battjes, J. A., H. J. Bakkenes, T. T. Janssen, and A. R. van Dongeren (2004), Shoaling of subharmonic gravity waves, *J. Geophys. Res*., 109, C02009, doi: 10.1029/2003JC001863.

Beach, R. A., and R. W. Sternberg (1987), The influence of infragravity motions on suspended sediment transport in the inner surf zone of a highly dissipative beach, In *Proceedings of the 14th international conference on Coastal Sediments*, 913–928, ASCE.

Biesel, F. (1952), Equations generales au second ordre de la houle irreguliere, *Houille Blanche*, 5, 372–376.

Bowen, A. J., and R. T. Guza (1978), Edge waves and surf beat, *J. Geophys. Res*., 83, 1913–1920.

Bricker, J. D., S. Munger, C. Péquignet, J. R. Wells, G. Pawlak, and K. F. Cheung, (2007), ADCP observations of edge waves off Oahu in the wake of the November 2006 Kuril Islands tsunami, *Geophys. Res. Lett*., 34, L23617, doi:10.1029/2007GL032015.

Bromirski, P. D., and P. Gerstoft (2009), Dominant source regions of the earth's hum are coastal, *Geophys. Res. Lett*., 36(L13303).

Bromirski, P. D., O. V. Sergienko, and D. R. MacAyeal (2010), Transoceanic infragravity waves impacting Antarctic ice shelves, *Geophys. Res. Lett*., 37(L02502).

Bruun, P. (1954), Coast erosion and the development of beach profiles, Technical Memorandum No. 44, Beach Erosion Board, US Army Corps of Engineers.

Bryan, K. R., and A. J. Bowen (1996), Edge wave trapping and amplification on barred beaches, *J. Geophys. Res*., 101, C3, doi:10.1029.95JC03627.

Dean, R. G. (1977), Equilibrium beach profiles: US Atlantic and Gulf coasts, Department of Civil Engineering, *Ocean Engineering Report* No. 12, University of Delaware, Newark, DE.

Dean, R. G. (1990), Equilibrium beach profiles: characteristics and applications. Report UFL/COEL-90/001, Coastal and Oceanographic Department, U. of Florida, Gainesville, FL.

Demirbilek, Z., O. G. Nwogu, and D. L. Ward (2007), Laboratory study of wind effect on runup over fringing reefs. Report 1: Data Report. ERDC/CHL TR-07-4. Coastal and Hydraulics Laboratory.

Elgar, S., and R. T. Guza (1985), Observations of bispectra of shoaling surface gravity waves, *J. Fluid Mech*., 161, 425–448.

Elgar, S., T. H. C. Herbers, and R. T. Guza (1994), Reflection of ocean surface gravity waves from natural beaches, *J. Phys. Oceanogr*., 24, 1503–1511.

Elgar, S., T. H. C. Herbers, M. Okihiro, J. Oltman-Shay, and R. T. Guza (1992), Observations of infragravity waves, *J. Geophys. Res*., 97(C10), 15573-15577.

Emery, W. J., and R. E. Thomson (1998), *Data Analysis Methods in Physical Oceanography*. Pergamon Elsevier Science, 400p.

Filloux, J. H., D. S. Luther, and A. D. Chave (1991), Long-term seafloor measurements of water pressure: Normal modes and infragravity waves, In *Proceedings XXth General Assembly, IUGG*, Vienna, Austria. IUGG.

Gourlay, M. R., (1996a), Wave set-up on coral reefs.1. set-up and wave-generated flow on an idealised two dimensional horizontal reef, *Coast. Eng*., 27(3-4), 161-193.

Gourlay, M. R., (1996b), Wave set-up on coral reefs. 2. set-up on reefs with various profiles, *Coastal Eng*., 28(1-4), 17-55.

Gourlay, M. R., and G. Colleter (2005), Wave-generated flow on coral reefs - an analysis for two-dimensional horizontal reef-tops with steep faces, *Coast. Eng*., 52(4):353-387.

Green, G. (1837), On the motion of waves in a variable canal of small depth and width, *Trans. Cambridge Philos.Soc*., 6, 457-462.

Guza, R. T., and E. B. Thornton (1982), Swash oscillations on a natural beach, *J. Geophys. Res.*, 87(NC1), 483–491.

Guza, R. T., and E. B. Thornton (1985), Observations of surf beat, *J. Geophys. Res.,* 90, 3161–3172.

Hardy, T. A., and I. R. Young (1996), Field study of wave attenuation on an offshore coral reef, *J. Geophys. Res*., 101, C6, doi:10.1029/96JC00202.

Harkins, G. S., and M. J. Briggs (1994), Resonant forcing of harbors by infragravity waves, In (editor Billy L. Edge, editor, Proceedings, International Conference on Coastal Engineering, pages 806–820, ASCE, New York NY.

Hasselmann, K., (1962), On the non-linear energy transfer in a gravity-wave spectrum, 1, general theory, *J. Fluid Mech*., 12, 481–500.

Hasselmann, K., W. Munk, and G. MacDonald (1963), Bispectra of ocean waves. In: Rosenblatt M. (Ed.) Times series analysis. Wiley, New York, 125-139.

Hearn, C. J. (1999), Wave-breaking hydrodynamics within coral reef systems and the effect of changing relative sea level, *J. Geophys. Res*., 104, C12, doi:10.1029/1999JC900262.

Henderson, S. M., and A. J. Bowen (2002), Observations of surf beat forcing and dissipation, *J. Geophys. Res*., 107(C11).

Henderson, S. M., R. T. Guza, S. Elgar, T. H. C. Herbers, and A. J. Bowen (2006), Nonlinear generation and loss of infragravity wave energy, *J. Geophys. Res.*, 111(C12007).

Herbers, T. H. C., S. Elgar, and R. T. Guza (1994), Infragravity-frequency (0.005-0.05 Hz) motions on the shelf: Part 1 : Forced waves, *J. Phys. Oceanogr*., 24, 917–927.

Herbers, T. H. C., S. Elgar, and R. T. Guza (1995a), Generation and propagation of infragravity waves, *J. Geophys. Res*., 100(C12), 24,863–24,872.

Herbers, T. H. C., S. Elgar, and R. T. Guza (1995b), Infragravity-frequency (0.005- 0.05 Hz) motions on the shelf. Part 2 : Free waves, *J. Phys. Oceanogr*., 25, 1063–1079.

Herbers, T. H. C., and M. C. Burton (1997), Nonlinear shoaling of directionally spread waves on a beach, *J. Geophys. Res*., 102, 21,101–21,114.

Janssen, T. T., J. A. Battjes, and A. R. van Dongeren (2003), Long waves induced by short-wave groups over a sloping bottom, *J. Geophys. Res.,* 108, 3252, doi:10.1029/2002JC001515.

Jaramillo S. and G. Pawlak (2011), Coral reef hydrodynamics: AUV-based bed-roughness mapping over a tropical reef, Coral Reefs, doi:10.1007/s00338-011-0731-9.

Kajiura K. (1961) On the partial reflection of water waves passing over a bottom of variable depth, *Proc. Tsunami Meetings 10th Pacific Science Congress, IUGG*, 24, 206-234.

Karunarathna, H., and K. Tanimoto (1995), Numerical experiments on low- frequency fluctuations on a submerged coastal reef, *Coastal Eng*., 26, 271–289.

Karunarathna, H., and K. Tanimoto (1996), Long-period water surface fluctuations on a horizontal coastal shelf with a steep seaward face, *Coast. Eng.,* 29, 123-147.

List, J. H. (1992), A model for the generation of two-dimensional surf beat, *J. Geophys. Res.*, 97(C4), 5623–5635.

Longuet-Higgins, A. S., and R. W. Stewart (1962), Radiation stress and mass transport in gravity waves, with application to ”surf beats”, *J. Fluid Mech*., 13, 481–504.

Lowe, R. J., J. L. Falter, M. D. Bandet, G. Pawlak, M. J. Atkinson, S. G. Monismith, and J. R. Koseff (2005), Spectral wave dissipation over a barrier reef, *J. Geophys. Res*., 110(C04001).

Lugo-Fernandez, A., H. H. Roberts, and J. N. Suhayda (1998a), Wave transformations across a Caribbean fringing-barrier coral reef, *Cont. Shelf Res*., 18(10), 1099–1124.

Lugo-Fernandez, A., H. H. Roberts, W. J. Wiseman, and B. L. Carter (1998b), Water level and currents of tidal and infragravity periods at Tague Reef, St. Croix (USVI), *Coral Reefs,* 17(4), 343–349.

Luick, J. L., and J. B. Hinwood (2008), Water levels in a dual-basin harbour in response to infragravity and edge waves, *Progr. Oceanogr.,* 77, 367-375.

Massel, S. R., and M. R. Gourlay (2000), On the modelling of wave breaking and set-up on coral reefs, *Coast. Eng*., 39, 1–27.

Masselink, G. (1995), Group bound long waves as a source of infragravity energy in the surfzone, *Cont. Shelf Res*., 15(13), 1525–1547.

Munk, W. H. (1949), Surf beat, *Eos Trans.* AGU, 30, 849–854.

Nakaza, E., and M. Hino (1991), Bore-like surf beat in a reef zone caused by wave groups of incident short period waves, *Fluid Dynamics Research*, 7(2), 89-100.

Nelson, R. C. (1996), Hydraulic roughness of coral reef platforms, *Appl. Ocean Res.*, 18, 265-274.

Norheim, C. A., and T. H. C. Herbers (1998), Nonlinear evolution of surface wave spectra on a beach, *J. Phys. Oceanogr*., 28, 1534-1551.

Nunes, V., and G. Pawlak (2008), Observations of bed roughness of a coral reef, *J. Coast. Res.*, 24(2B), 39-50.

Nwogu, O., and Z. Demirbilek (2010), Infragravity wave motions and runup over shallow fringing reefs, *J. Waterw. Port Coastal Ocean Eng*., 136(6), 295-305.

Okihiro, M., R. T. Guza, and R. J. Seymour (1993), Excitation of seiche observed in a small harbour, *J. Geophys. Res*., 98(C10), 18,201–18,211.

Oltman-Shay, J., and R. T. Guza (1987), Infragravity edge wave observations on two California beaches, *J. Phys. Oceanogr*., 17, 644–663.

Péquignet, A. C. N., J. M. Becker, M. A. Merrifield, and J. Aucan (2009), Forcing of resonant modes on a fringing reef during tropical storm Man-Yi, *Geophys. Res. Lett*., 36(L03607).

Péquignet A. C. N., J. M. Becker, M. A. Merrifield, and S. Boc (2011), The dissipation of wind wave energy across a fringing reef at Ipan, Guam, *Coral Reefs*, 30, 71–82, doi 10.1007/s00338-011-0719-5

Raubenheimer, R., and R. T. Guza (1996), Observations and predictions of run-up, *J. Geophys. Res*., 101(C11), 25575–25587.

Roeber, V., K.F. Cheung, (2012). Boussinesq-type model for energetic breaking waves and its application to fringing reef environment. *Coast. Eng*., accepted.

Ruessink, B. G. (1998a), Bound and free infragravity waves in the nearshore zone under breaking and nonbreaking conditions, *J. Geophys. Res*., 103(C6):12,795–12,805.

Ruessink, B. G. (1998b), The temporal and spatial variability of infragravity energy in a barred nearshore zone, *Cont. Shelf Res*., 18, 585–605.

Ruggiero, P., R. A. Holman, and R. A. Beach (2004), Wave run-up on a high-energy dissipative beach, *J. Geophys. Res*., 109(C06025).

Schaffer, H. A. (1993), Infragravity waves induced by short-wave groups, *J. Fluid Mech*., 247, 551–588.

Sheremet, A., R. T. Guza, S. Elgar, and T. H. C. Herbers (2002), Observations of nearshore infragravity waves: Seaward and shoreward propagating components, *J. Geophys. Res*. 107, doi: 10:1029/2001JC000970.

Sheremet, A., J. M. Kaihatu, S. -F. Su, E. R. Smith, and J. M. Smith (2011), Modeling of nonlinear wave propagation over fringing reefs, *Coast. Eng.*, 58(12), 1125-1137, doi:0.1016/j.coastaleng.2011.06.007.

Stockdon, H. F., R. A. Holman, P. A. Howd, and A. H. Sallenger (2006), Empirical parameterization of setup, swash, and runup, *Coast. Eng*., 53(7), 573–588.

Suhayda, J. M. (1974), Standing waves on beaches, *J. Geophys. Res*., 79, 3065-3071.

Swart D. (1974), Offshore sediment transport and equilibrium beach profiles. Technical report 131, Delft Hydraulic Laboratory, Netherlands.

Symonds, G., K. P. Black, and I. R. Young (1995), Wave-driven flow over shallow reefs, *J. Geophys. Res*. 100, C2, doi:10.1029/94JC02736.

Symonds, G., D. A. Huntley, and A. J. Bowen (1982), Two-dimensional surf beat: long wave generation by a time-varying breakpoint, *J. Geophys. Res*., 87(C1), 492–498.

Taebi, S., R. J. Lowe, C. B. Pattiaratchi, G. N. Ivey, G. Symonds, and R. Brinkman (2011), Nearshore circulation in a tropical fringing reef system, *J. Geophys. Res*., 116(C02016).

Tait, R. J. (1972), Wave setup on coral reefs, *J. Geophys. Res*., 77(C10), 2207–2211.

Thomson, J., S. Elgar, B. Raubenheimer, T. H. C. Herbers, and R. T. Guza (2006), Tidal modulation of infragravity waves via nonlinear energy losses in the surfzone, *Geophys. Res. Lett.*, 33(L05601).

Tucker, M. J. (1950), Surf beats: sea waves of 1 to 5 min. period, *Proc. Roy. Soc. London Ser. A*, 214, 79-98.

Uchiyama, Y., and J. C. McWilliams (2008), Infragravity waves in the deep ocean: Generation, propagation, and seismic hum excitation. *J. Geophys. Res*., 113, C07029, doi:10.1029/2007JC004562.

van Dongeren, A., A. Reniers, J. Battjes, and I. Svendsen (2003), Numerical modeling of infragravity wave response during Delilah, *J. Geophys. Res*., 96(C9), 2723–2736.

van Dongeren. A. R., J. A. Battjes, T. T. Janssen, J. van Noorloos, K. Steenhauer, G. Steenbergen, and A. Reniers (2007), Shoaling and shoreline dissipation of low-frequency waves, *J. Geophys. Res.,* 112, C02011, doi:10.1029/2006JC003701.

Vetter, O. J., J. M. Becker, M. A. Merrifield, A. C. Péquignet, J. Aucan, S. J. Boc, and C. E. Pollock (2010), Wave setup over a Pacific island fringing reef, *J. Geophys. Res*., 115, C12066, doi:10.1029/2010JC006455.

Young, I. R. (1989), Wave transformations on coral reefs, *J. Geophys. Res.,* 94(C7), 9779-9789.

Zawada, D. G., G. A. Piniak, and C. J. Hearn (2010), Topographic complexity and roughness of a tropical benthic seascape, *Geophys. Res. Lett.*, 37, L14604, doi:10.1029/2010GL043789.

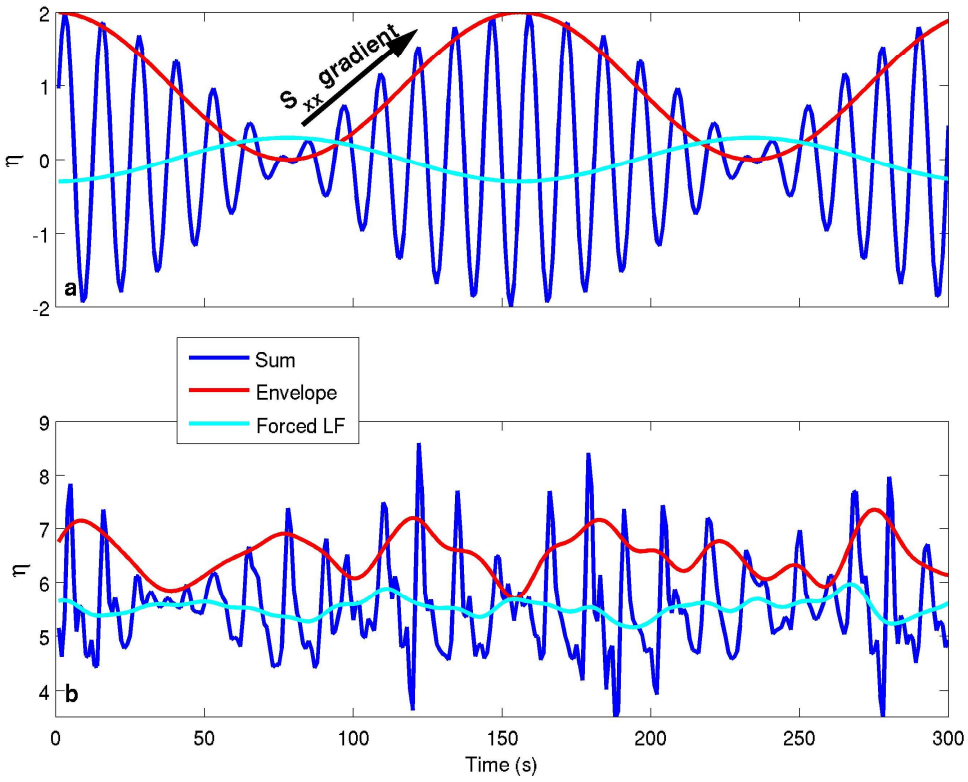

Figure 4.1: Schematic of a SS wave group and the LF bound wave. a) An idealized wave group is formed by summing two SS waves with similar frequencies (0.0833 and 0.0769 Hz, blue curve). The envelope of the group (red) has a frequency of $\Delta f = 0.0064$ Hz. The theoretical bound wave (cyan, equation 4.1), in balance with the radiation stress gradient associated with the group, has a trough under the maxima of the group and a peak under the minima. b) A similar pattern as depicted in (a) is observed on the fore reef at Ipan. The low frequency surface elevation (cyan) is nearly 180° out of phase with the envelope of the SS waves (red), estimated using a Hilbert transform and low-pass filter (from sensor 9, 17:00Z, 2 October 2009).

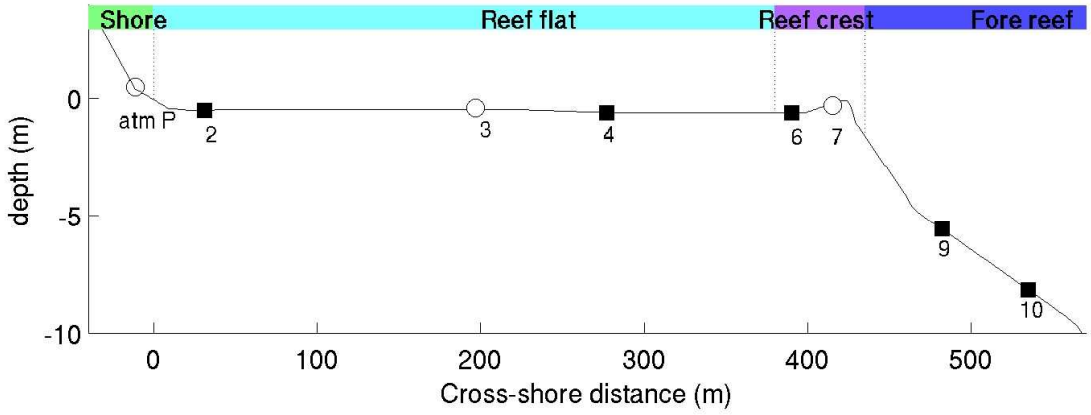

Figure 4.2: Cross-shore bathymetry of Ipan reef from SHOALS data and definition of the different sections of the reef. Open circles indicate the SBE26plus pressure sensors. Black squares indicate collocated pressure sensors and current-meters (Nortek ADP) used in this study. The sensor labeled 'atm P' is a single SBE26plus pressure sensor deployed above sea level to measure atmospheric pressure.

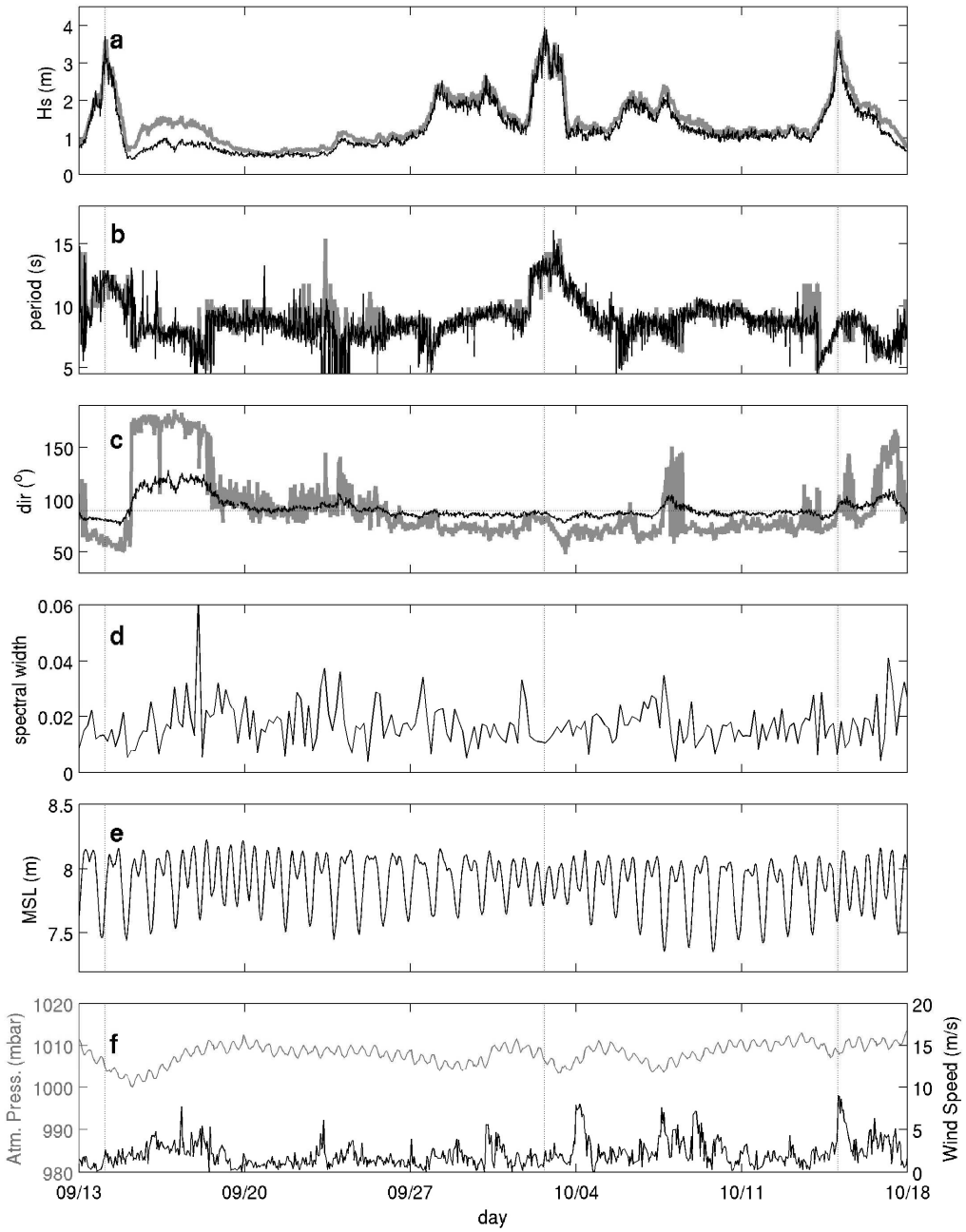

Figure 4.3: Wave and water level conditions at the fore reef, including a) sea and swell (SS) band significant wave height, b) the peak SS wave period, c) the incident SS wave angle (relative to magnetic north), d) the half-power spectral width of the SS spectrum from the most offshore sensor (sensor 10, black line), and from the CDIP wave buoy (thick grey line) and e) water level. f) Atmospheric pressure and wind speed observed at the NOAA CO-OPS tide gauge station at Pago Bay. The vertical dotted lines show the time of the peak of the three main wave events on 14 September 2009, 2 October 2009 and 14 October 2009.

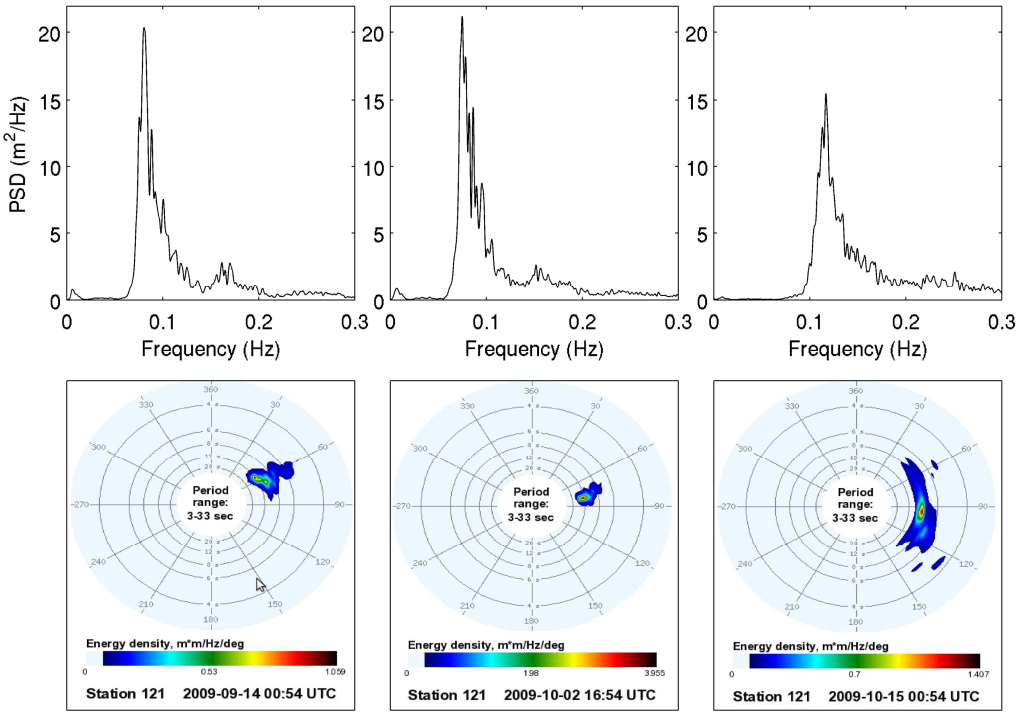

Figure 4.4: Power spectral density of 3 hour time series of sea surface elevation at the most offshore sensor (sensor 10, upper panels) and 30 minute directional spectra at the offshore wave buoy (lower panels) for the three main wave events: 14 September 2009, 01:30 Z (left), 2 October 2009, 17:30 Z (middle) and 15 October 2009, 01:30 Z (right).

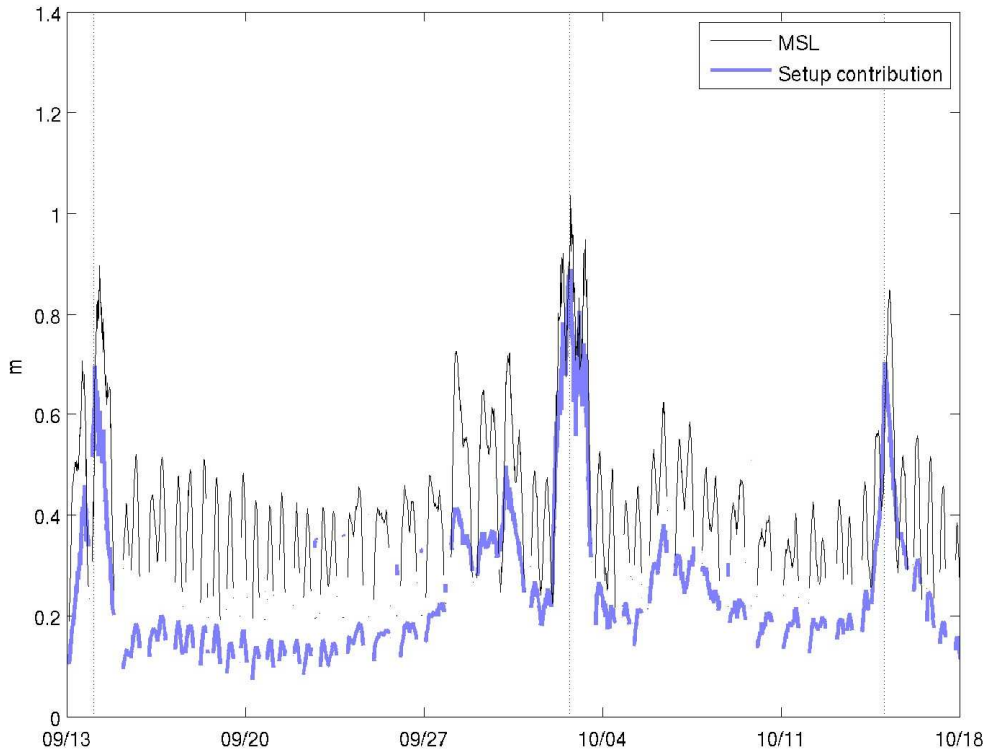

Figure 4.5: Mean sea level (MSL) and estimated setup (computed following Vetter *et al*. 2010) at the most inshore sensor (sensor 2) during the September/October 2009 deployment. The dashed lines indicated the peak of the three wave events.

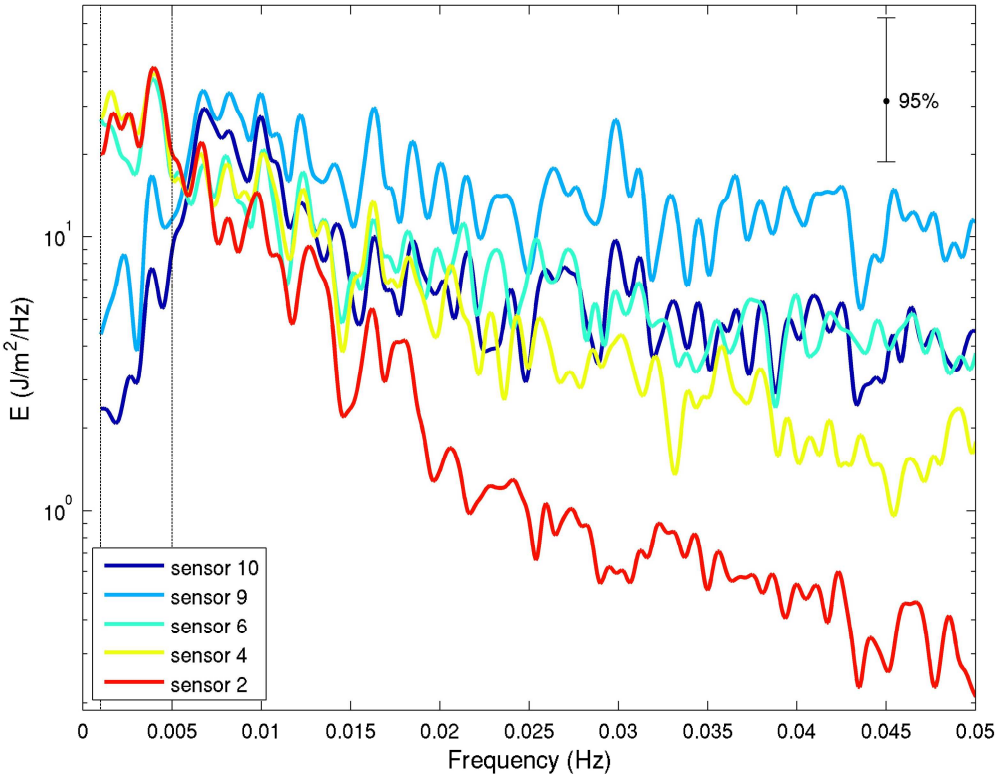

Figure 4.6: Spectral estimates of total energy at the 5 current-meter locations across Ipan reef for the wave event of 2 October 2009 (16:00 to 19:00 Z). The dotted lines show the limits of the far infragravity frequency band.

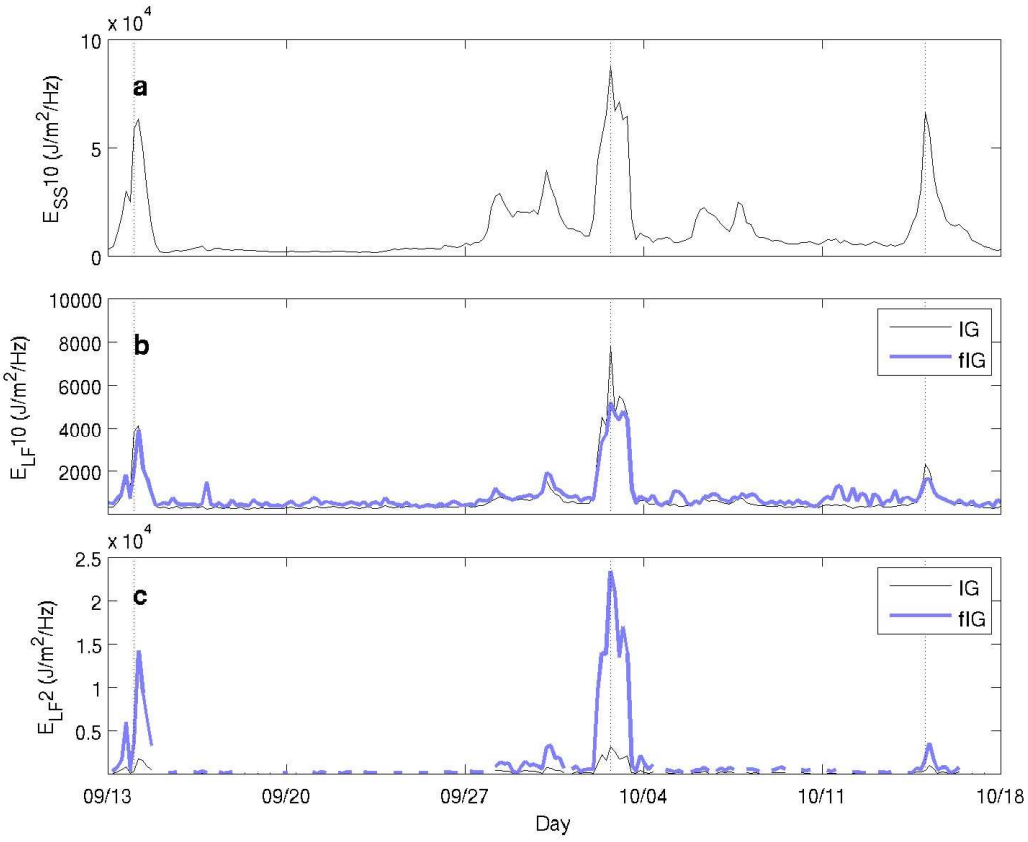

Figure 4.7: Time series of frequency band averaged total energy density over 3-hr intervals for a) the SS frequency band (0.05 Hz < f < 0.5 Hz) for the most offshore sensor (10), b) the LF band (IG, 0.005 < f < 0.05 Hz, and fIG, 0.001 < f < 0.005 Hz) for the most offshore sensor (10), and c) the LF band for the most inshore sensor (2). The vertical dotted lines show the main wave events.

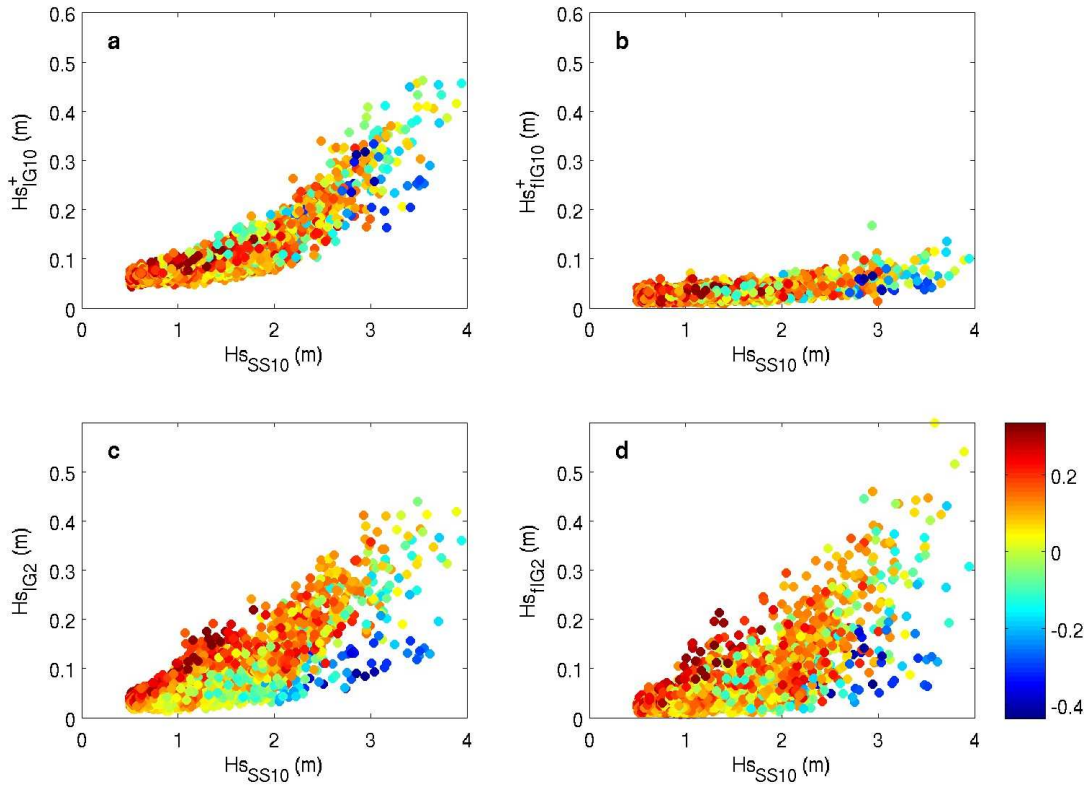

Figure 4.8: Incoming sensor 10 (a and b) and incoming+outgoing=net sensor 2 (c and d) IG (a and c) and fIG (b and d) significant wave heights over 3-hr intervals plotted as a function of $H_{SS10,}$ the incident SS significant wave height at sensor 10. The colored dots denote tidal level elevation at sensor 10.

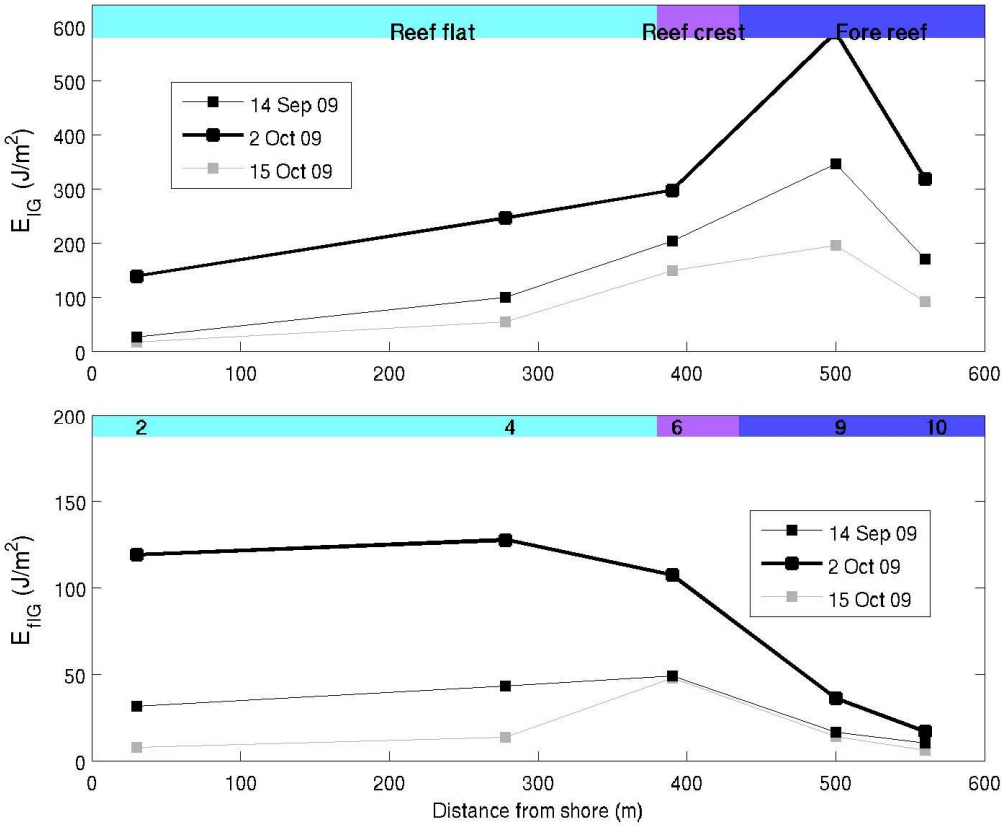

Figure 4.9: Cross-shore variation of integrated total energy over the IG (top) and fIG (bottom) frequency bands for the three main wave events: 14 September 2009, 00:00 to 03:00 Z (thin black line), 2 October 2009, 16:00 to 19:00 Z (thick black line) and 14 October 2009, 00:00 to 03:00 Z (grey line). Colorbar shows the different sections of the reef and the sensor numbers.

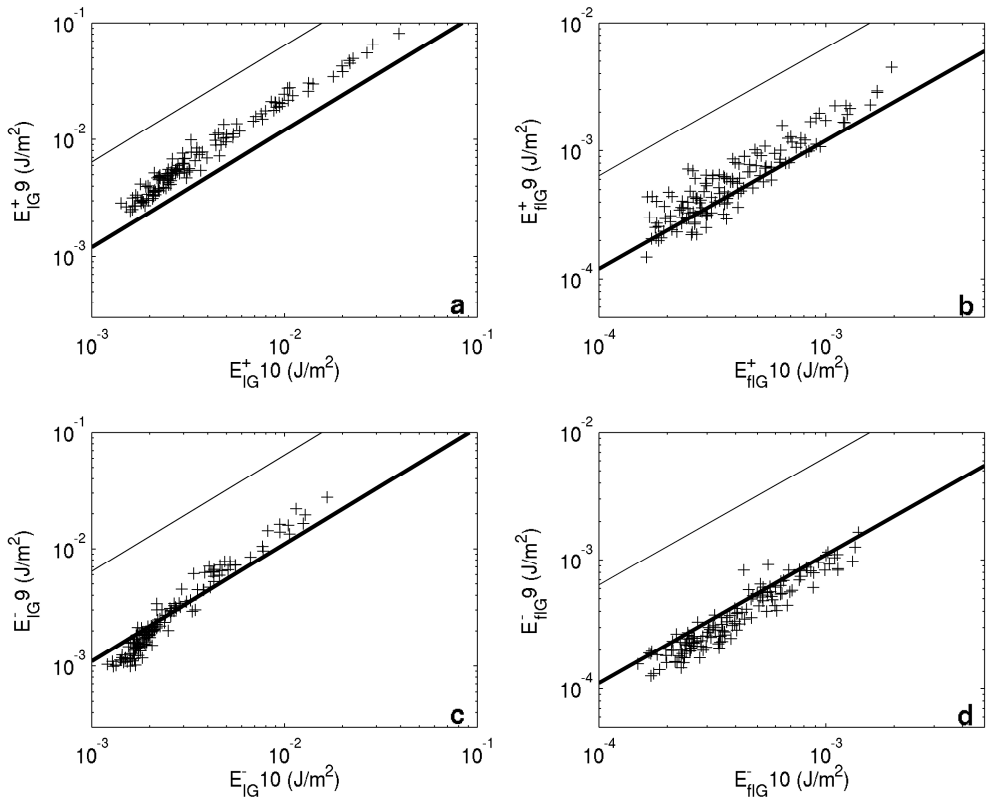

Figure 4.10: Comparison of energy growth rate and theoretical rates of shoaling of free and bound waves on the fore reef. Integrated total energy over the IG (a and c) and fIG (b and d) bands at sensors 9 and 10 is plotted for the incoming (a and b) and the outgoing (c and d) signals.

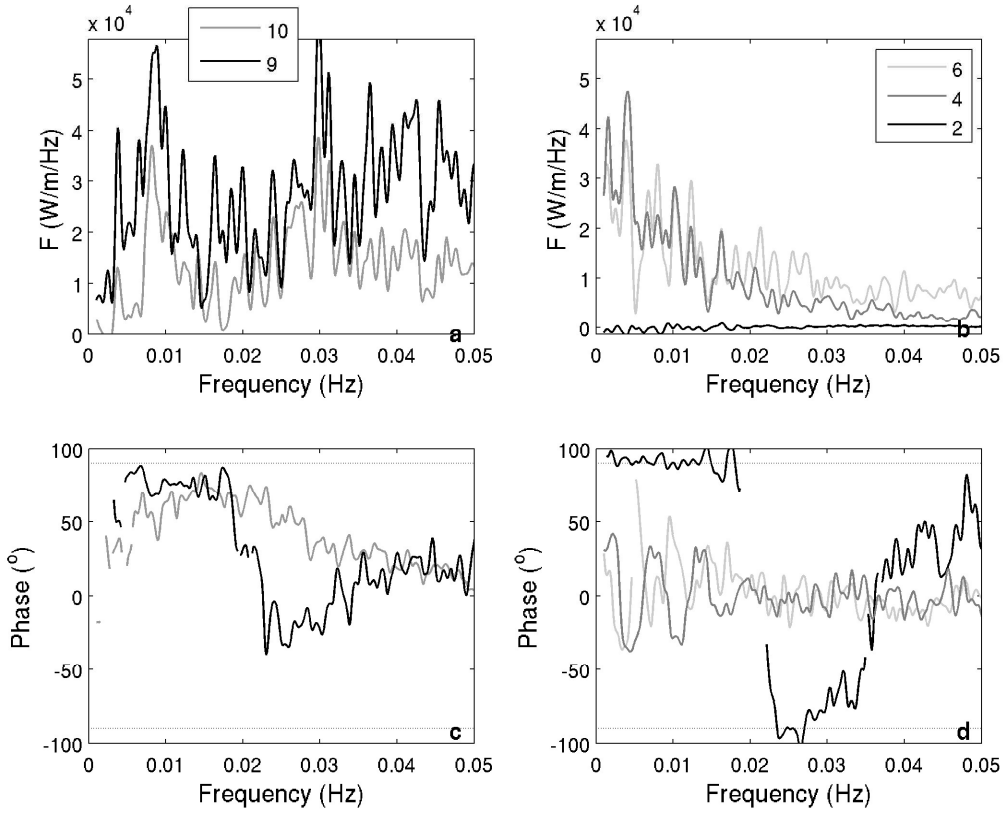

Figure 4.11: Spectral cross-shore energy flux estimates for 2 October 2009 (16:00 to 19:00 Z) using equation 4.5c (a and b) and phase between the sea surface elevation and the cross-shore velocity used for the cross-shore energy flux estimate (c and d), for two current meters on the fore reef (a and c) and three current meters on the reef flat (b and d).

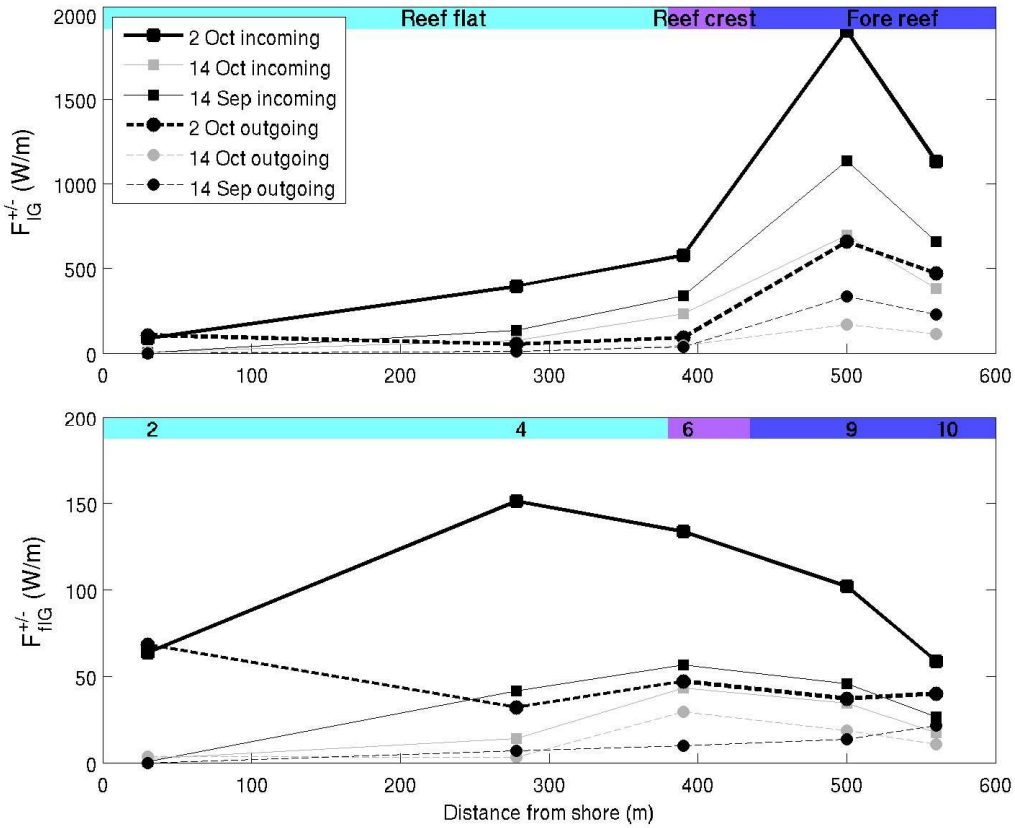

Figure 4.12: Cross-shore variation of integrated energy flux over the IG (top) and fIG (bottom) frequency bands for the three main wave events: 14 September 2009 (thin black line), 2 October 2009 (thick black line) and 14 October 2009 (grey line). Solid lines show the incoming fluxes, dotted lines show the outgoing fluxes.

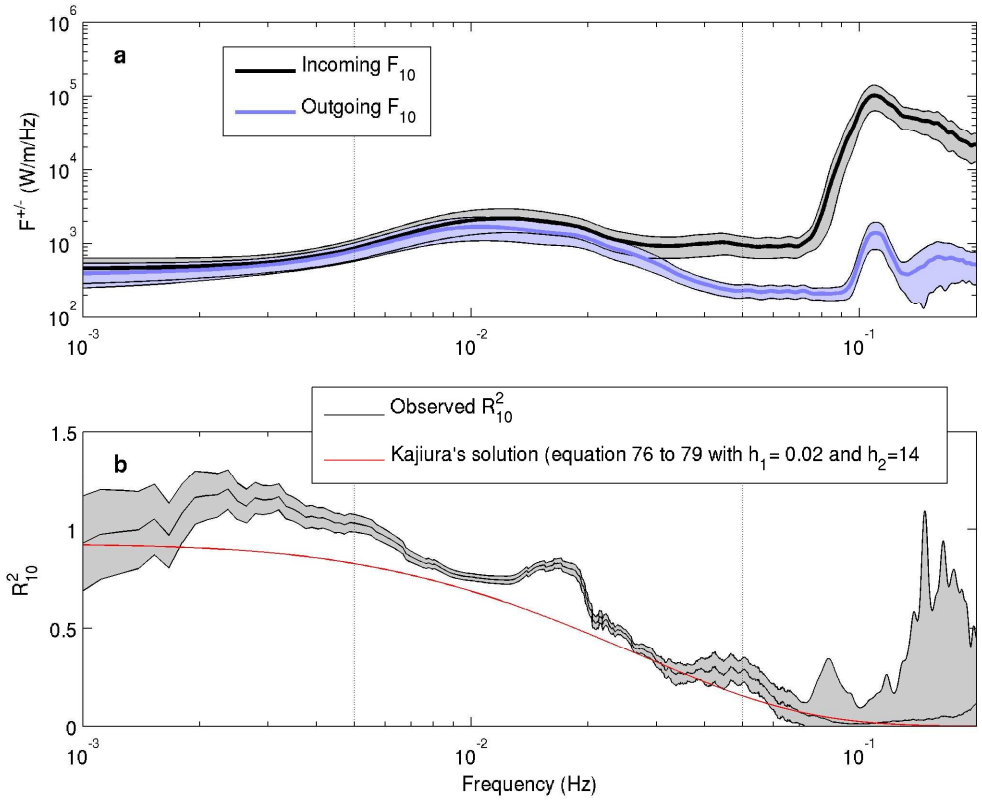

Figure 4.13: a) Mean incoming and outgoing spectral energy flux at sensor 10. Standard deviation is shown with the shaded area estimated for 3 hour time series when the reef is submerged. b) The ratio of outgoing energy flux to incoming energy flux at sensor 10. The ratio of the energy flux is estimated for 3 hour time series when the reef is submerged. The shaded area shows the standard deviation associated with the mean reflection coefficient estimates. The red line is the theoretical solution for an idealized tanh cross-shore profile (Kajiura 1961, equation 76 with h_1=0.02 and h_2=14 and n=0.03) calculated following Kajiura (1961) equation 79.

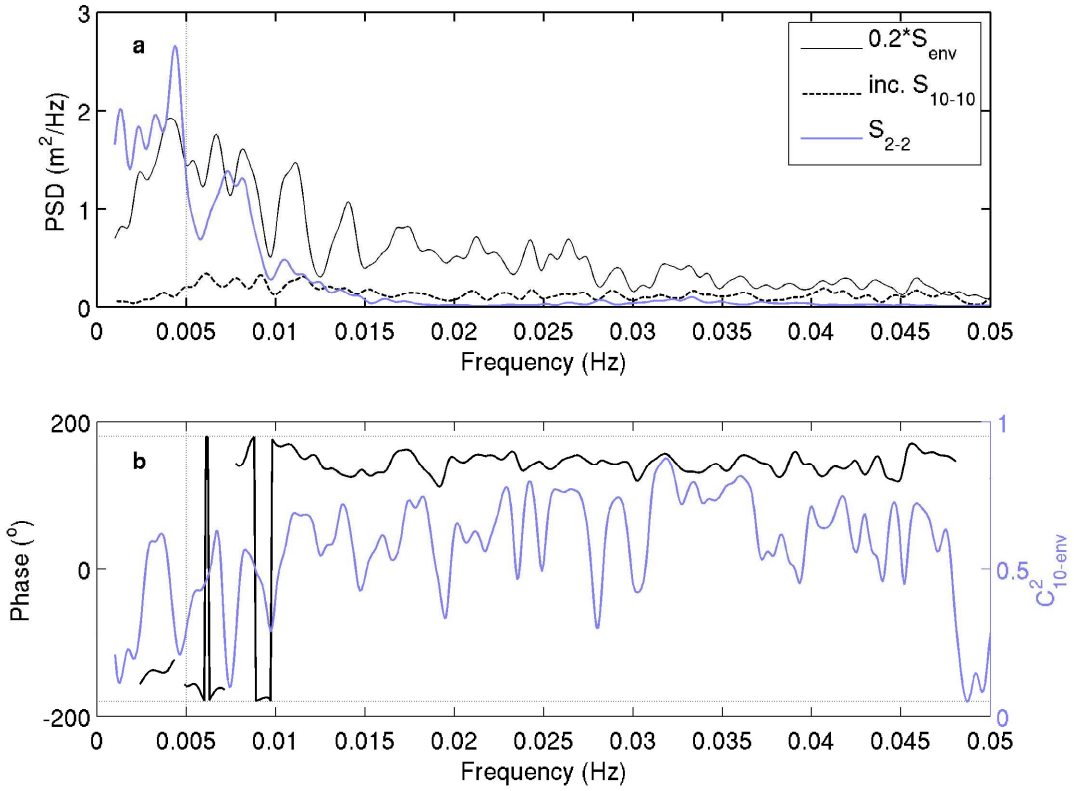

Figure 4.14: a) Power spectral density of incoming sea surface elevation at sensor 10 (thick black line), the total sea surface elevation at sensor 2 (blue) , and the SS envelope at sensor 10 (scale by 0.1, thin black). b) Coherence squared (black) and phase (blue) between the SS envelope and the sea surface elevation at sensor 10. Spectra are estimated from a 3 hour time series starting at 16:00 Z on 2 October 2009.

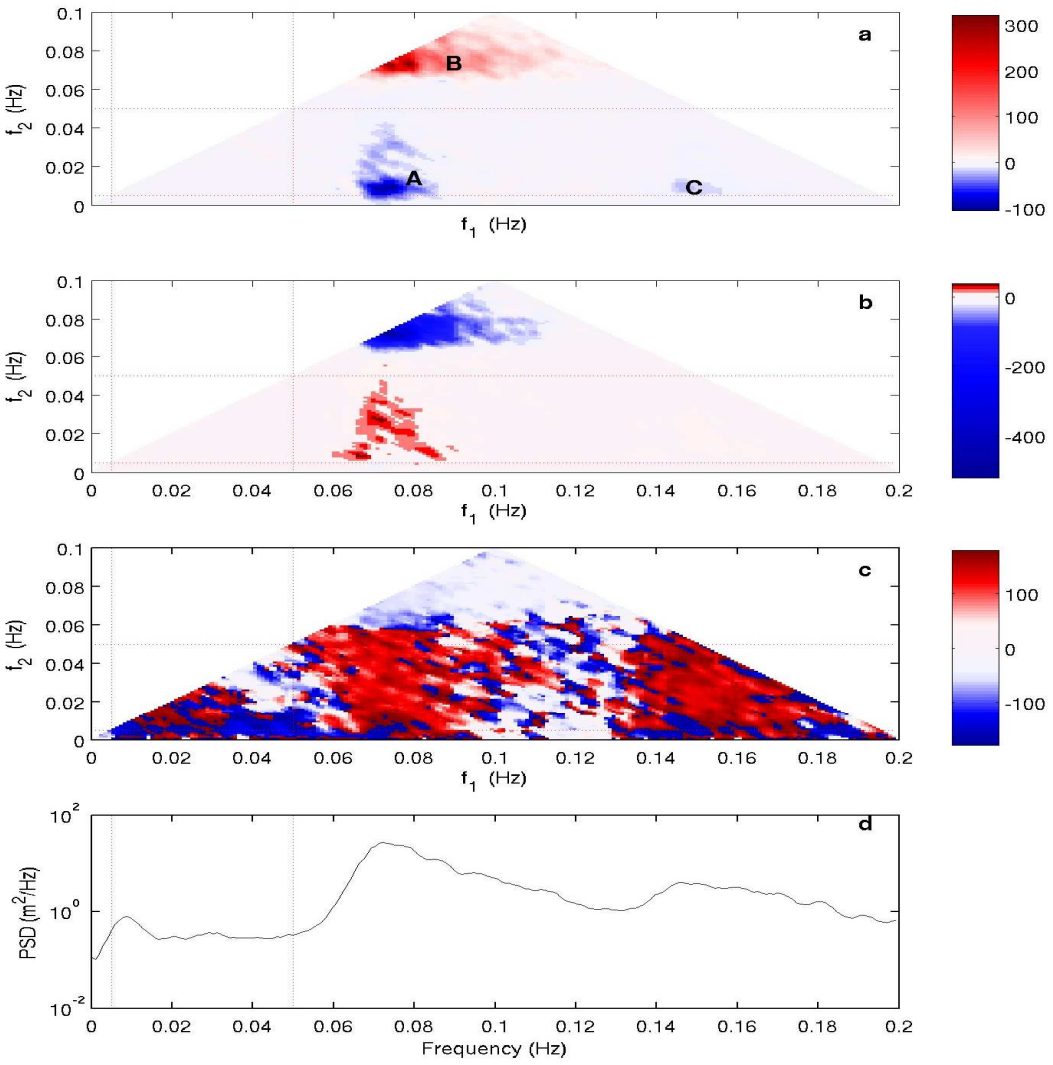

Figure 4.15: Bispectral estimate of the sea surface elevation of the 2 October 2009 16:00 to 19:00 Z event at sensor 10. a) The real and b) imaginary parts of the bispectrum (B4.3) and c) the biphase are shown with d) the corresponding power spectral density. Dotted lines show the limits of the fIG and IG bands. **A** identifies the range of frequencies where difference interactions (biphase ~ 180°) between energetic SS waves and IG wave energy are significant (greater than two standard deviation separation relative to random noise, see appendix B). **B** identifies the range of frequencies where sum interactions (biphase ~ 0°) between SS waves and SS harmonics are significant. **C** identifies the range of frequencies where difference interactions (biphase ~ 180°) between SS harmonic waves and IG waves are significant.

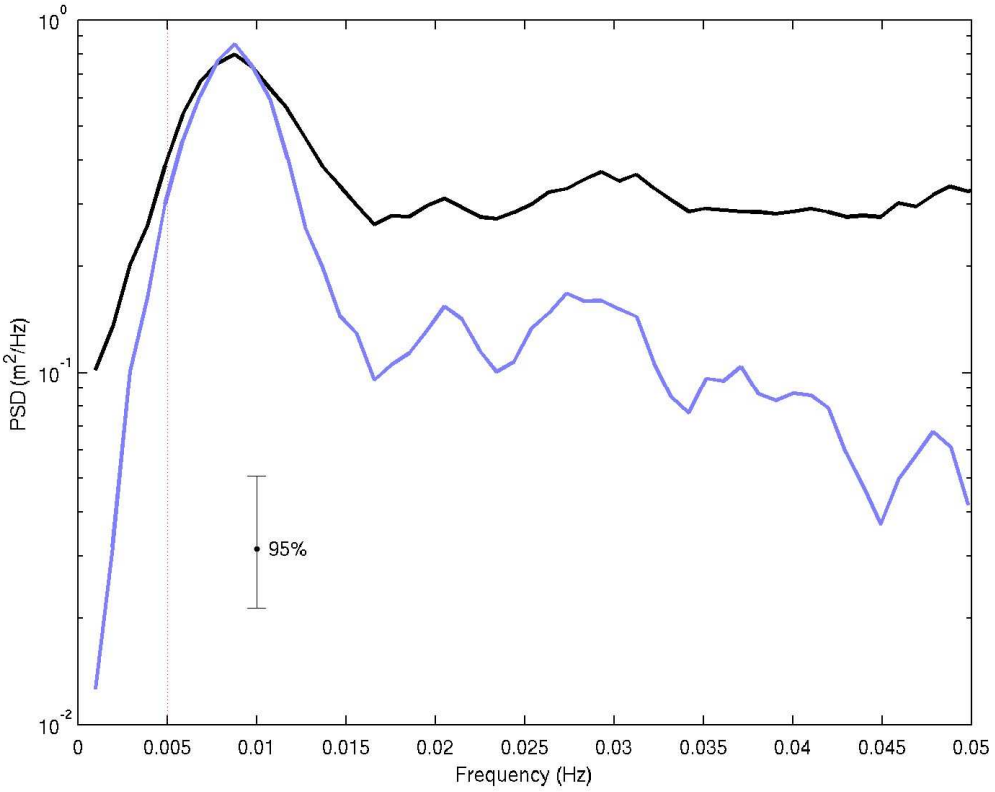

Figure 4.16: Power spectral density of sea surface elevation at sensor 10 (black line) and estimated power spectral density of forced IG waves (blue line) estimated from equation (B4.6) for the 2 October 2009 event (16:00 to 19:00 Z).

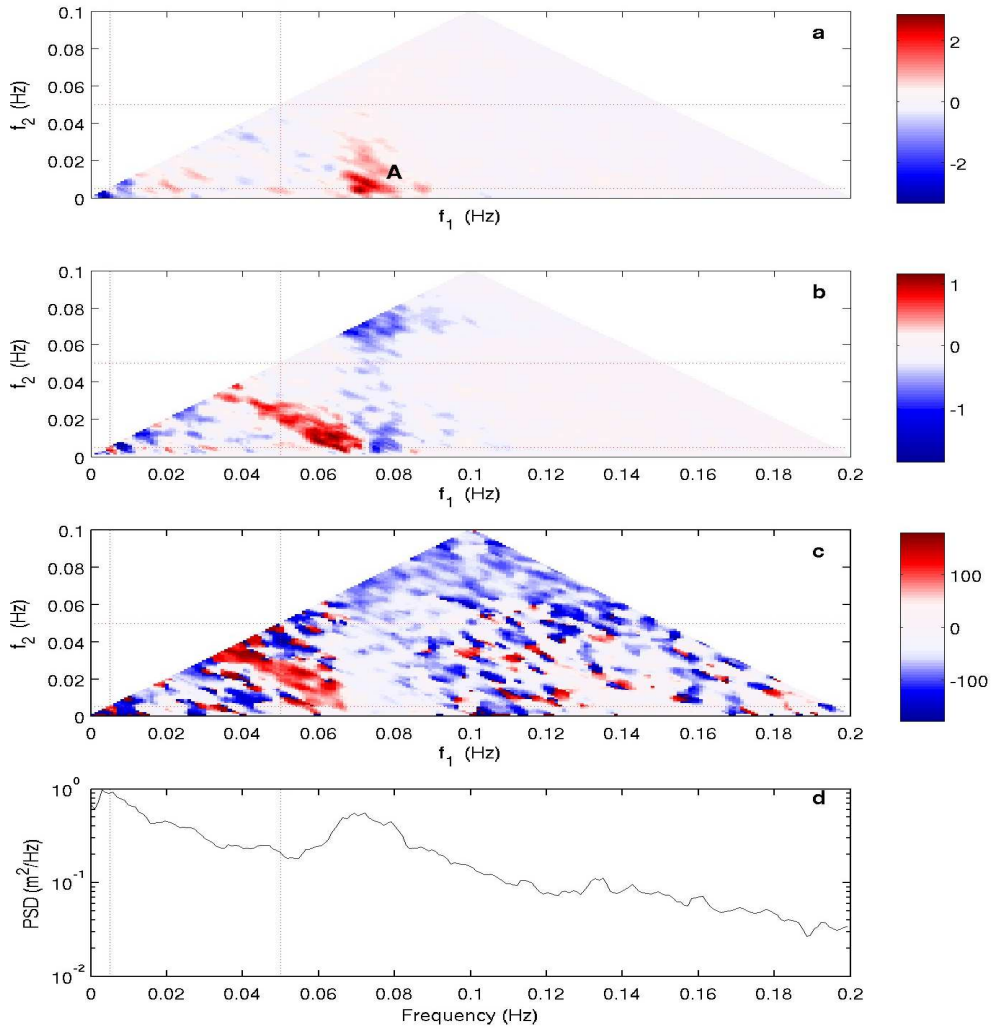

Figure 4.17: Bispectral estimate of the sea surface elevation of the 2 October 2009 16:00 to 19:00 Z event at sensor 6. a) The real and b) imaginary parts of the bispectrum (B4.3) and c) the biphase are shown with d) the corresponding power spectral density. Dotted lines show the limits of the fIG and IG bands. At this location, sum interactions occur in zone A (biphase ~ 0° (c), difference interactions occurred in zone A on the fore reef), and real part of the bispectrum (a) is weak compared to the fore reef bispectra in zones B and C (Figure 4.15a). The imaginary part of the bispectrum is negative in zone A (c) in contrast to the fore reef where it is positive (Figures 4.15b).

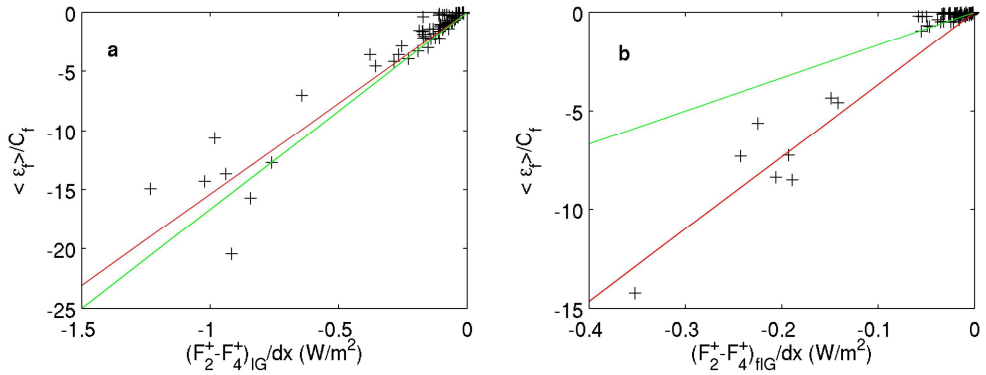

Figure 4.18: Comparison between a) IG and b) fIG cross-shore energy flux divergence and IG frictional dissipation parameterization $<\varepsilon_f/C_f>$ estimated from equation (4.6). The red line shows the least squares fit of the data to estimate the IG and fIG friction coefficient on the reef flat. The green line shows the dissipation estimated from the SS friction coefficient.

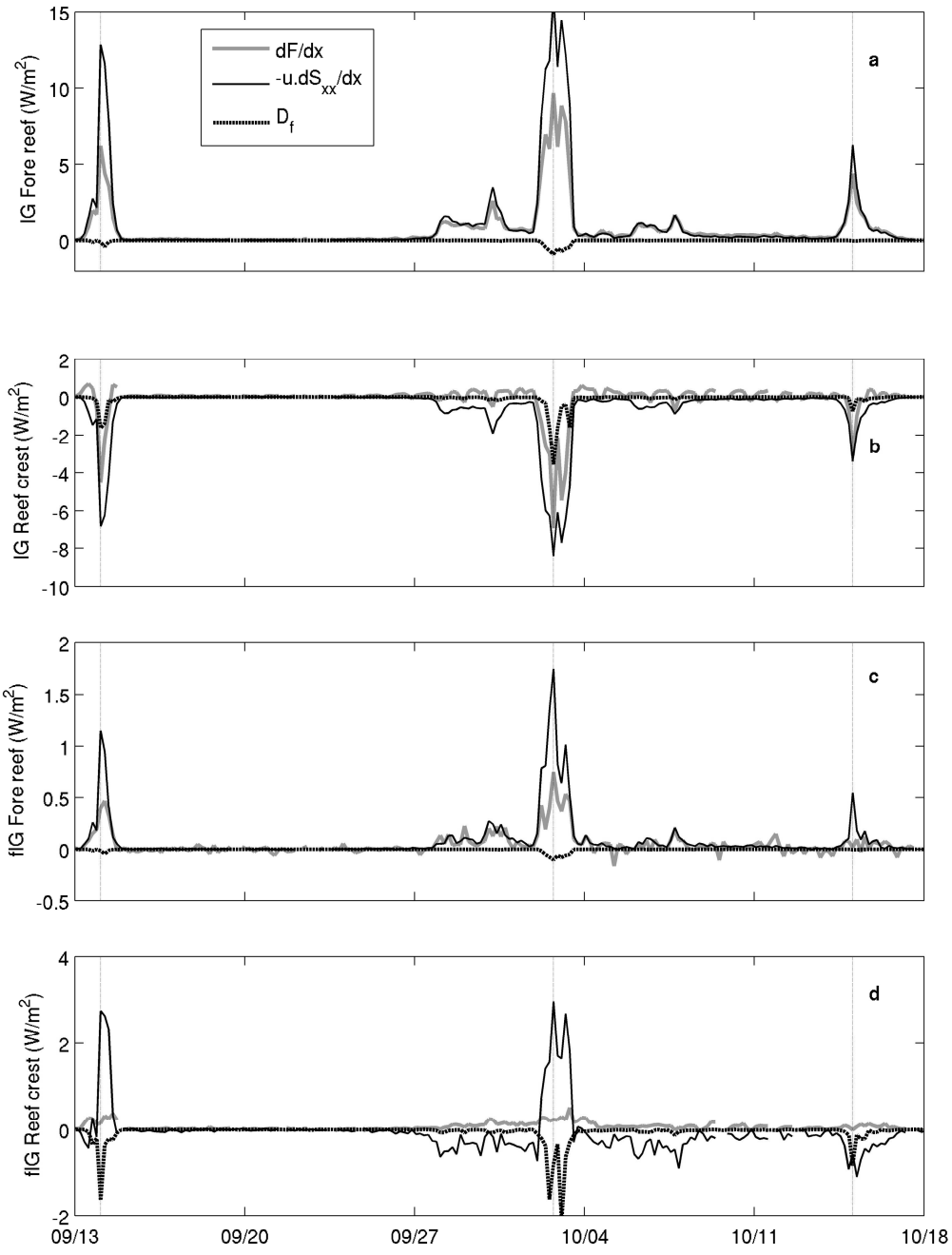

Figure 4.19: Time series of the three main terms $\frac{\partial F(f)}{\partial x}$, $W(f)$ and $D(f)$ in equation 4.4 integrated in the IG and fIG bands and across the fore reef (sensor 10 to sensor 9) and across the reef crest (sensor 9 to sensor 6).

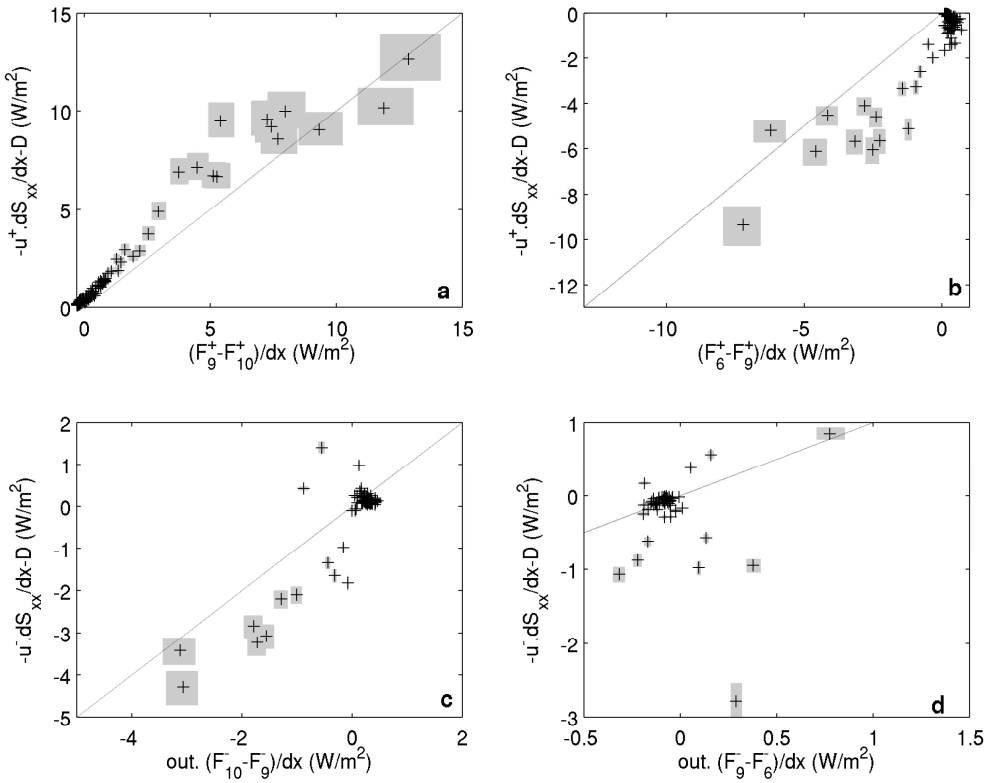

Figure 4.20: IG energy flux balance: Comparison between incoming (a and b) and outgoing (c and d) cross-shore IG energy flux divergence and nonlinear transfer of energy to the IG frequency band (0.005 to 0.05 Hz) minus the frictional dissipation, between sensor 10 and 9 (a and c) and sensor 9 and 6 (b and d). The 1:1 ratio is shown as a dotted line. Grey shading shows the 95% confidence intervals of the frequency integrated spectral estimates.

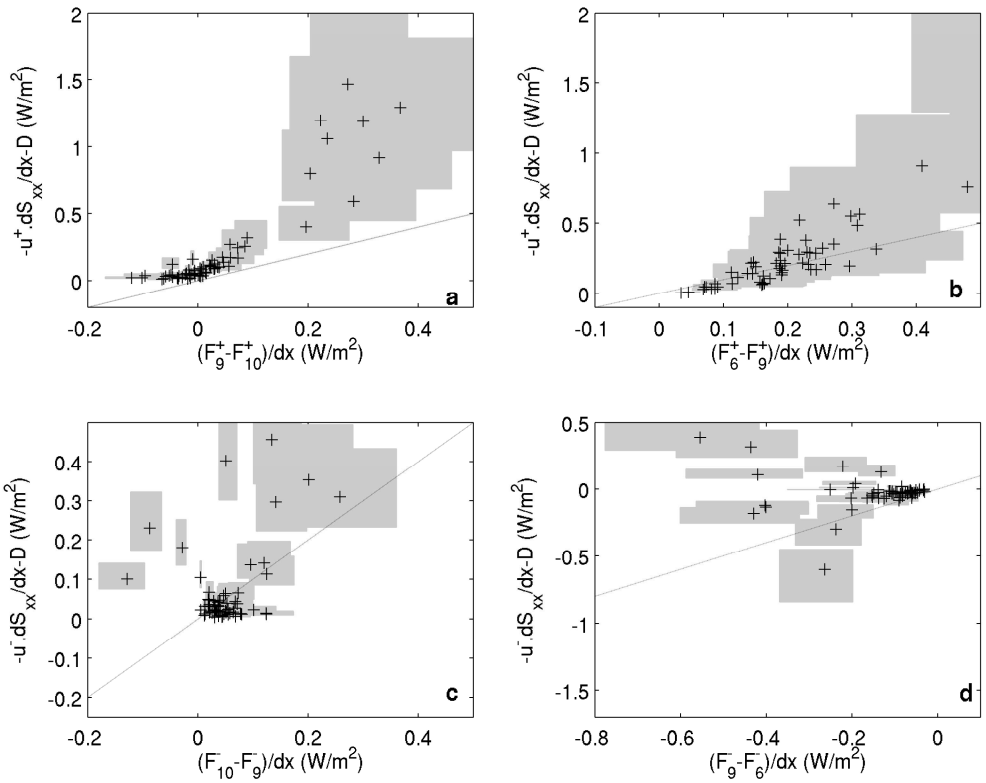

Figure 4.21: fIG energy flux balance: Comparison between incoming (a and b) and outgoing (c and d) cross-shore fIG energy flux divergence and nonlinear transfer of energy to the fIG frequency band (0.001 to 0.005 Hz) minus the frictional dissipation, between sensor 10 and 9 (a and c) and sensor 9 and 6 (b and d). The 1:1 ratio is shown as a dotted line. Grey shading shows the 95% confidence intervals of the frequency integrated spectral estimates.

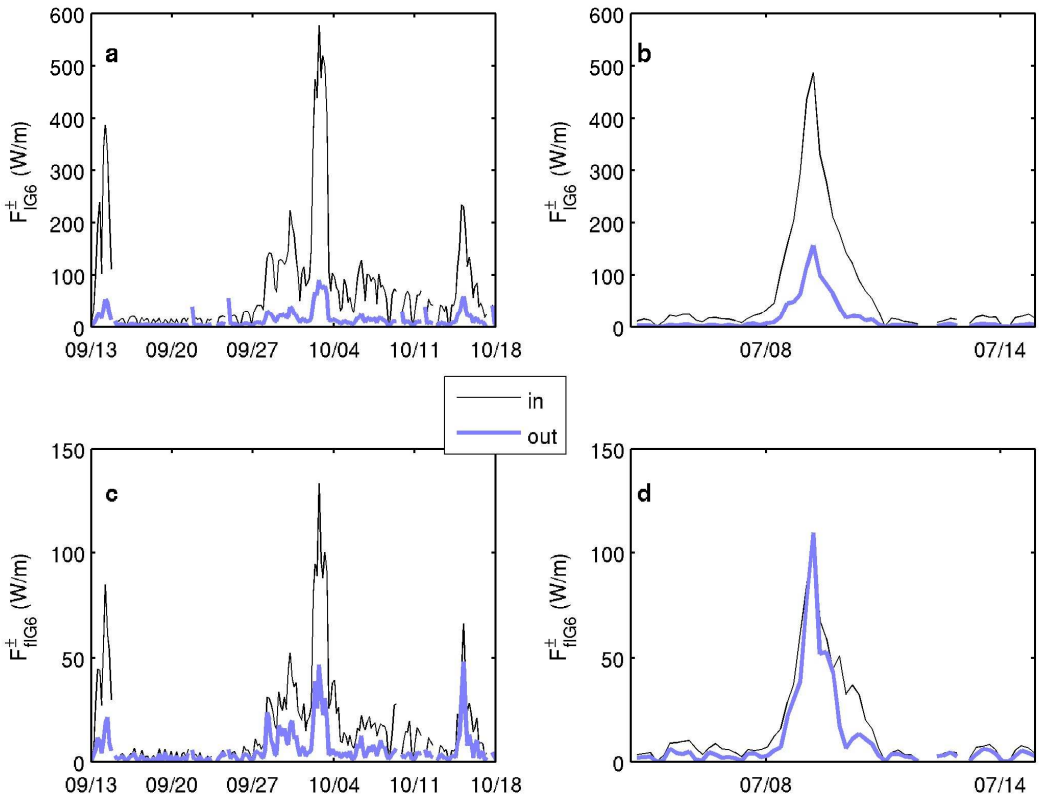

Figure 4.22: Time series of incoming and outgoing energy flux in the IG (a and b) and fIG (c and d) frequency bands for the winter 2009 deployment (a and c), and the deployment of tropical storm Man-Yi, described in chapter 3 (b and d).

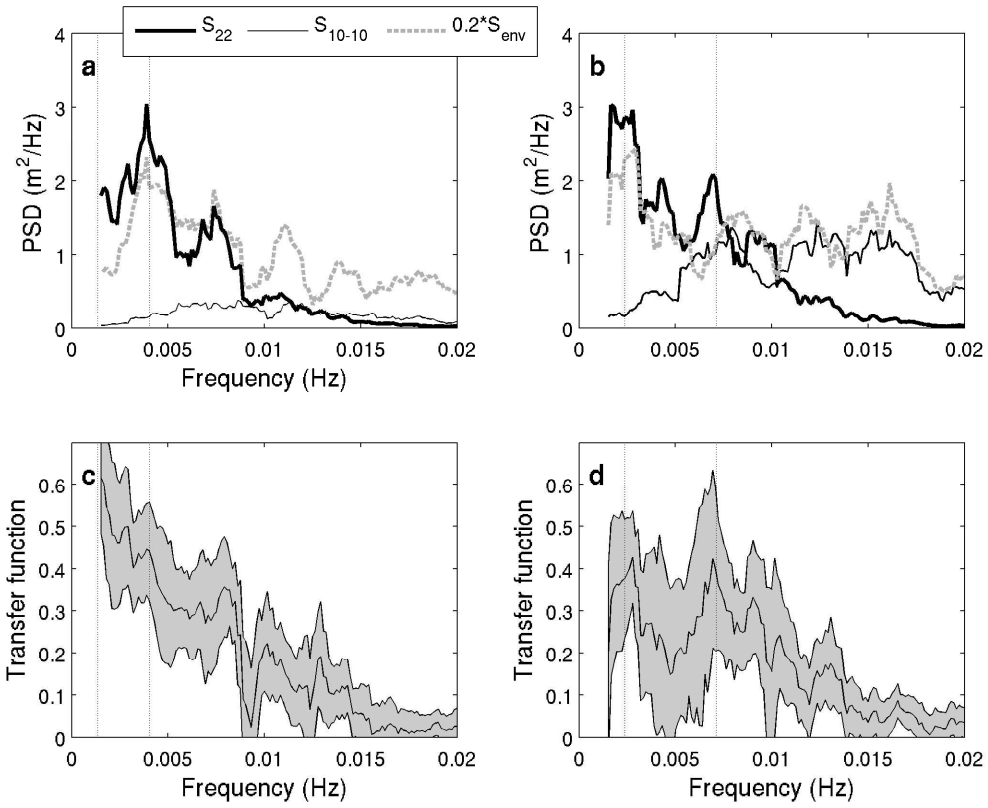

Figure 4.23: A comparison of auto and cross-spectra in the fIG and IG frequency bands during the 2 October 2009 event (a and c) and the peak of tropical storm Man-Yi (b and d). a) and b) Auto-spectra of sea surface elevation at the most inshore sensor (S_{22}), the most offshore sensor ($S_{10\text{-}10}$) and the envelope of the swell band energy at sensor 10 (S_{env}). c) and d) transfer function between sea surface elevation at the sensor 2 and the envelope of sea surface elevation at sensor 10. The vertical dotted lines show the first 2 theoretical resonant frequencies. Shaded area shows the 95% confidence interval.

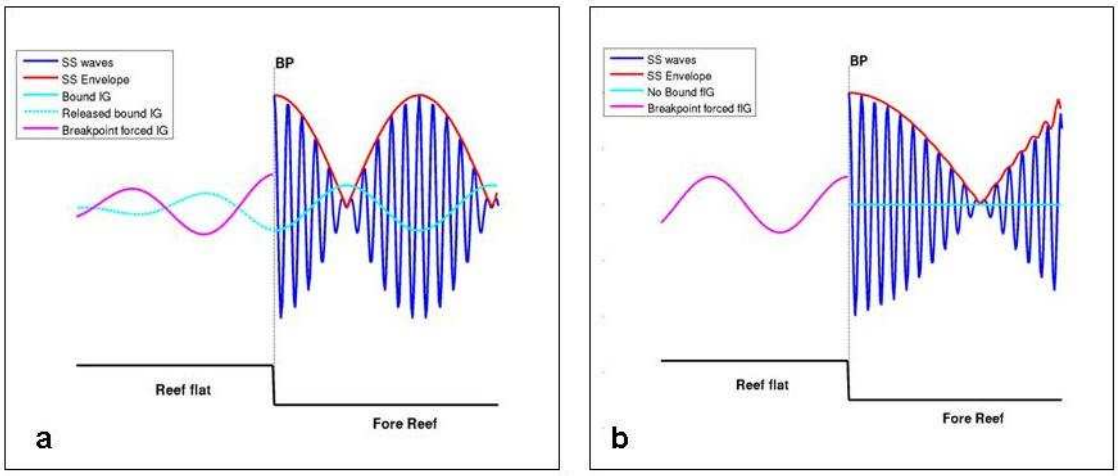

Figure 4.24: Schematic of the surfzone dynamics of a) incoming IG and b) fIG energy at Ipan, Guam. a) Forced bound waves at IG frequencies are released by breaking of the incident SS waves at the breakpoint (BP). The radiation stress gradient provided by the varying breakpoint at IG frequencies generates waves which opposes the released bound waves inshore of the breakpoint and results in loss of IG energy flux at the reef crest. b) Because of the lack of bound waves at fIG frequencies, fIG oscillations, forced by the varying breakpoint radiation stress gradient, grow unopposed resulting in growth of fIG energy flux at the reef crest.

Chapter 5

Conclusions

5.1 Summary

The analysis of pressure sensor and current-meter data collected across Ipan reef during large wave events has allowed us to determine the suite of processes that result in wave-driven inundation on a reef-fringed shore. Generally, the transformation of waves across Ipan reef is characterized by an offshore energy spectrum dominated by SS waves, and a reef flat spectrum dominated by LF oscillations.

The dominance of LF waves on the reef flat is partially the result of the strong dissipation of SS wave energy across Ipan reef, Guam, which results in ~ 97% reduction of the incident SS wave height over ~500 m. Depth-limited breaking at the reef crest accounts for ~80% of the SS dissipation, with the remaining dissipation attributed to bottom friction. The non linear transfer of energy between SS and LF bands is negligible in the SS energy balance. We estimate that less than 5% of the incident SS energy flux is reflected at the fore reef. Wave energy in the SS band on the reef flat is strongly depth-

limited and controlled by the reef submergence level. At Ipan, due to the small tidal range, the reef flat submergence level is largely controlled by breaking wave setup.

The LF spectrum on the fore reef consists predominantly of bound waves at IG frequencies, while the reef flat spectrum consists of free fIG oscillations, which are particularly energetic at standing mode frequencies. As a result of the breaking of SS waves, strong radiation stress gradients exist across the reef crest and vary on the time scale of wave groups. The low frequency oscillations of the radiation stress gradient associated with the SS wave group are nearly in phase with the SS wave envelope. This time-varying radiation stress gradient opposes the bound wave released through breaking, and forces free oscillations at fIG frequencies. These oscillations travel across the reef flat where frictional IG dissipation is estimated to be approximately twice as large as fIG dissipation. These long waves then are reflected at the shoreline and set up partially standing waves across the reef flat.

Standing modes have been observed across Ipan reef flat during the large wave conditions of tropical storm Man-Yi due to the large increase in water depth on the reef flat from wave setup. The increase in water depth on the reef flat promoted the establishment of the normal modes across the reef both by decreasing the frictional dissipation on the reef flat and increasing the frequency of the fundamental mode. The reduced friction on the reef flat allowed the shoreline-reflected breakpoint-generated fIG energy flux to return to the reef crest with enough outgoing flux to maintain the standing wave structure. At the peak of tropical storm Man-Yi, oscillations of the SS wave group near the frequency of the fundamental mode resulted in forcing of fIG oscillations with

amplitudes exceeding a meter on the reef flat. In contrast, the large wave events of September and October 2009 occurred during low tide. The low water levels observed on the reef were responsible for significant dissipation of LF waves and only partially standing waves developed at the normal modes frequencies. In addition, the frequency of the fundamental mode fell below the frequency of the energetic part of the SS envelope and mode 1 was preferentially generated.

5.2 Significance and implications for prediction of inundation in Guam

5.2.1 Significance for nearshore dynamics

The strong SS dissipation that leads to the dominance of low frequency motions near the shore is similar to the dynamics observed on dissipative sandy shores (e.g. Ruessink 1998, Ruggiero *et al*. 2004). Loss of IG energy to SS waves by triad interactions has been observed on sandy beaches (Thomson *et al*. 2006, Henderson *et al*. 2006). On sloping beaches, a steep normalized bed slope has been shown to promote breakpoint forced waves whereas a gentle slope favors the release of bound waves (Battjes *et al*. 2004). The co-existence of both processes has been considered theoretically (Schaffer 1993), but few observational studies have considered the competition between bound waves and breakpoint forcing that results in growth/loss of fIG/IG energy. Here, the time-varying radiation stress gradient is provided by the time-varying amplitude of the breaking waves, rather than the spatial oscillation of the moving breakpoint observed on

gently sloping beaches. The confinement of wave breaking to a narrow area around the reef crest is a distinct characteristic of wave transformation on fringing reefs such as Ipan. In that respect, localized wave breaking on a fringing reef tends to resemble the situation for a barred beach. Features of a fringing reef that set it apart from barred beaches include the existence of two distinct morphological sections (i.e. fore reef and reef flat/lagoon) with different dissipation mechanisms (breaking and bottom friction, respectively), and with low frequency wave reflections occurring both on the fore reef and at the shoreline. The hydrodynamics on fringing reefs are not simply a limiting case of sloping beaches.

Very low frequency (VLF) motions have been observed previously in the surfzone of sandy beaches (e.g. Oltman-Shay *et al*. 1989, MacMahan *et al*. 2004) but they were observed to be vortical motions with little surface expression resulting from either instability of longshore currents (Smith and Largier 1995) or rip currents (Haller and Dalrymple 2001). Here, the VLF oscillations observed on the reef flat are gravity waves at fIG frequencies with strong surface expressions. A common feature between reef fIG oscillations and VLF motions observed on beaches is that both have been linked to forcing by varying wave groups (Reniers *et al*. 2007).

5.2.2 Significance for fringing reefs

The transformation of SS waves on Ipan reef is typical of the dissipation observed across other fringing reefs with attenuation rates between 75 and 95% of the incident wave

energy reported over reef flats (e.g. Young 1989, Hardy and Young 1996, Lugo-Fernandez 1998b, Massel and Gourlay 2000, Brander *et al*. 2004). The strong dependence on water level is also a general characteristic of SS transformation on fringing reefs (e.g. Lugo-Fernandez *et al*. 1998a, Hearn 1999). As observed on other reefs, bottom friction significantly contributes to the dissipation of SS energy where breaking does not occur (Lowe *et al*. 2005) and the range of friction factors measured on Ipan reef is representative of the variety of substrate observed on other reefs (e.g. Gerritsen 1981, Nelson 1996, Hearn 1999, Lowe *et al*. 2005).

Low frequency oscillations have been reported previously on other reefs (Hardy and Young 1996, Lugo-Fernandez 1998a, Brander *et al*. 2004). The forcing and dissipation of low frequency waves on Ipan may not be representative of all fringing reefs. The important hydrodynamic parameters for fringing reefs include the length of the reef flat, the slope of the fore reef, the submergence depth over the reef flat, and the friction factors. The frequencies of normal modes of a given reef are functions of the reef flat length and the water depth (equation 3.2) and chapter 4 demonstrates how resonance conditions may affect the amplitude of low frequency oscillations on reef flats. Fringing reefs (examples in Figure 5.1) also produce a variety of breaking patterns which determine the forcing of low frequency motions. The results of the laboratory experiments of Karunarathna and Tanimoto (1995) suggest that an increase in water depth that prohibits wave breaking may lead to more IG energy on the reef flat from shoaling of the bound wave. The present work suggests that in the absence of breaking, fIG may not be generated, and the released bound IG wave may shoal onto the reef flat rather than compete with the locally generated breakpoint forced waves. In addition,

frictional effects have been shown to dominate the dynamics seaward of the surf zone and long and shallow reefs may prevent the establishment of well-developed standing modes.

5.2.3 Significance for Guam

The work presented in this dissertation analyzes data from two main deployments at Ipan, covering approximately 6 months, but a total of more than 6 years of data were collected at Ipan as part of the PILOT project. The large wave events recorded during winter 2009 are representative of the large winter wave events observed along the east coast of Guam (Figure 5.2). The largest event observed was when tropical storm Man-Yi passed to the South of Guam. SS energy at the shore is controlled by the total water depth which is largely due to wave setup as the tidal range at Ipan is small (~0.5m). Shoreline IG waves energy increases linearly with increasing incident SS energy, and weak tidal modulations are evident. Predicting the excitation of fIG motions on the reef flat appears to require the knowledge of the spectral structure of the incident wave envelope and is a topic of future research.

In Guam, flooding has been reported during typhoons, but the wave-driven inundation often is more significant than the predicted storm surge (Jaffe and Richmond 1992). When super typhoon Pongsona passed through Guam on 8 December 2002, causing wide spread destruction with wind gusts peaking at 278 km/h, only ~0.5m rise in sea level was observed at the Pago bay tide gauge on the exposed East coast of Guam. In contrast, the largest non-tidal sea levels observed at the same tide gauge correspond to

large incident wave events not associated with typhoons (Figure 5.2). All large wave events, however, do not result in high total water levels as tidal height is an important consideration. When large waves events correspond to high tides, significant inundation may be expected.

5.3 Future research

Laboratory experiments suggest that breakpoint forcing in the surfzone may be a source of outgoing LF energy (Battjes *et al*. 2004). Although reflection alone does not explain the observed ratio of outgoing to incoming fIG energy flux (R^2>1) on the fore reef (Figure 4.13), the present data do not conclusively show that breakpoint forcing of outgoing LF energy occurs in the surfzone of Ipan reef. A detailed study of the interference pattern between reflected and outgoing locally generated energy fluxes (Baldock and Huntley 2002) may be required to balance the outgoing LF energy flux budget across the reef crest. This may require a finer cross-shore sensor resolution to characterize the reflection of long waves on the fore reef. The importance of the tidal dependence of reflection and friction also needs to be carefully analyzed in the outgoing energy flux equation.

The use of a cross-shore array of sensors in this dissertation naturally raises the question of the longshore variability of the results observed at our array. A recent deployment of a longshore array on Ipan reef has shown significant longshore variations in wave setup associated with the presence of a cross-reef channel (Clark *et al*. 2012).

The strong depth dependence of the reef resonant modes, bottom friction and reflection on the reef flat suggests that longshore variations of these processes should also be observed. This longshore dependence of the hydrodynamics along with the changes in reef lengths may contribute to the longshore variability of inundation observed during Typhoon Russ (Jaffe and Richmond 1992).

The cavernous nature of the fore reefs and reef crests makes the deployment of instruments in these regions particularly perilous. For this reason, detailed observations of the break point and the immediate surfzone are lacking for Guam and for fringing reefs in general. Analyzing the data collected in Ipan, it is clear that finer cross-shore resolution around the reef crest is necessary to accurately assess energy transformation across the reef. To overcome the shortcomings of field measurements, numerical models may prove to be a particularly useful tool to investigate the strongly nonlinear nature of wave transformation on the steep reef face (Sheremet *et al*. 2011). Linear wave models predict well the evolution of total energy flux, significant wave height and other bulk wave parameters on reefs (Monismith 2007).

To date, most models of long wave transformation on reefs are validated using laboratory measurements (Nakaza and Hino 1991, Karunarathna and Tanimoto 1995, Nwogu and Demirbilek 2010, Sheremet *et al*. 2011). Recent numerical modelling works using a spectral model with quadratic (second-order) nonlinearities (Sheremet *et al*. 2011) and a Boussinesq model (Nwogu and Demirbilek 2010, Roeber and Cheung 2012) have reproduced well the nonlinear transformation across the smooth steep reef prototypes used in flume experiments (Demirbilek *et al*. 2007). Both the Boussinesq model and

laboratory experiments reproduce the low frequency shift of the wave spectrum observed across the reef, but for both, the fundamental normal mode of the reef dominates the low frequency energy (Nwogu and Demirbilek 2010). Although some nodal structure related to the reef normal modes was observed on Ipan, the conditions when full standing modes are excited appear to be exceptional (Péquignet *et al*. 2009) as friction on the reef flat appears to prohibit the establishment of normal modes. The importance of the normal modes in the laboratory experiment (Nwogu and Demirbilek 2010, Roeber and Cheung 2012) may result from unrealistic frictional dissipation. In addition to variable reef flat friction coefficients, real reefs offer significant dissipation from the rough spur and groove and porous structure of the reef crest, which smooth 2D cross-section and solid bottom topography models and flumes do not capture. The present work highlights the importance of frictional dissipation not only for SS waves but also for long waves and more realistic roughness in laboratory experiments or real reef data may be needed to validate numerical models in the future.

References

Baldock T. E. and D. A. Huntley (2002), Long-wave forcing by the breaking of random gravity waves on a beach, *Proc. R. Soc. Lond*. 458, 2177-2201, doi: 10.1098/rspa.2002.0962.

Battjes J. A., H. J Bakkenes, T. T. Janssen and A. R. van Dongeren (2004), Shoaling of subharmonic gravity waves, *J. Geophys. Res*.,109, C02009, doi: 10.1029/2003JC001863.

Brander, R.W.**,** Kench, P.S. and Hart, D. (2004), Spatial and temporal variations in wave characteristics across a reef platform, Warraber Island, Torres Strait, Australia. *Marine Geology*, 207: 169-184.

Clark J. S., M. A. Merrifield and J. M. Becker (2012), The influence of a cross-reef channel on circulation over a fringing reef at Ipan, Guam. Abstract 12053 presented at 2012 Ocean Sciences Meeting, Salt Lake City Utah, 20-24 Feb.

Demirbilek, Z., O. G. Nwogu, and D. L. Ward (2007), Laboratory study of wind effect on runup over fringing reefs. Report 1: Data Report. ERDC/CHL TR-07-4. Coastal and Hydraulics Laboratory.

Gerritsen F. (1981), Wave attenuation and wave set-up on a coastal reef. Technical report. Look Lab, Univ. Hawaii, Honolulu.

Haller, M.C., and D.A. Dalrymple (2001) Current instabilities, *J. Fluid Mech.*, 433,161-192.

Hardy T. A., and I. R. Young (1996), Field study of wave attenuation on an offshore coral reef, *J. Geophys. Res*., 101, C6, doi:10.1029/96JC00202.

Hearn C. J. (1999), Wave-breaking hydrodynamics within coral reef systems and the effect of changing relative sea level, *J. Geophys. Res*.104(C12), 30007–30019.

Hearn C. J. (2011), Perspectives in coral reef hydrodynamics. *Coral Reefs*, 30(1), 1-9, doi: 10.1007/s00338-011-0752-4

Henderson S. M., R. T. Guza, S. Elgar, T. H. C. Herbers, and A. J. Bowen (2006), Nonlinear generation and loss of infragravity wave energy, *J. Geophys. Res.*, 111(C12007).

Herbers T. H. C., S. Elgar, and R. T. Guza (1995), Generation and propagation of infragravity waves, *J. Geophys. Res.*,100(C12), 24,863-24,872.

Jaffe B. E., B. M. Richmond (1993), Overwash variability on the shoreline of Guam during Typhoon Russ. *Proc 7th Int Coral Reef Symp* 1, 257–264.

Karunarathna H., and K. Tanimoto (1995), Numerical experiments on low-frequency fluctuations on a submerged coastal reef, *Coastal Eng*., 26, 271–289.

Lowe R. J., Falter J. L., Bandet M. D., Pawlak G., Atkinson M. J, Monismith S. G., Koseff J. R. (2005), Spectral wave dissipation over a barrier reef, *J. Geophys. Res*.110(C04001). doi:10.1029/2004JC002711.

Lugo-Fernandez A. , H. H. Roberts, W. J. Wiseman, and B. L. Carter (1998a), Water level and currents of tidal and infragravity periods at Tague Reef, St. Croix (USVI), *Coral Reefs,* 17(4), 343–349.

Lugo-Fernandez A., H. H. Roberts, J. N. Suhayda (1998b), Wave transformations across a Caribbean fringing-barrier coral reef. *Cont. Shelf Res.*18(10), 1099–1124.

MacMahan, J. H., A. J. H. M. Reniers, E. B. Thornton, and T. P. Stanton (2004), Surf zone eddies coupled with rip current morphology, *J. Geophys. Res.*, 109, C07004, doi:10.1029/2003JC002083.

Massel S. R., M. R. Gourlay (2000), On the modelling of wave breaking and set-up on coral reefs. *Coast. Eng.* 39, 1–27.

Monismith S. (2007), Hydrodynamics of coral reefs. *Annu. Rev. Fluid Mech.* 39: 37-55.

Nelson R. C. (1996), Hydraulic roughness of coral reef platforms. *Appl. Ocean Res.* 18, 265–274.

Nakaza, E. and M. Hino (1991), Bore-like surf beat in a reef zone caused by wave groups of incident short period waves, *Fluid Dynamics Research*, 7(2), 89-100.

Nwogu O., and Z. Demirbilek (2010), Infragravity wave motions and runup over shallow fringing reefs, *J. Waterw. Port Coastal Ocean Eng*., 136(6), 295-305.

Oltman-Shay, J., P.A. Howd, and W.A. Birkemeier (1989), Shear instabilities of mean longshore current. 2. Field observations, *J. Geophys. Res.,* 94, 18031-18042.

Péquignet A. C. N., J. M. Becker, M. A. Merrifield, and J. Aucan (2009), Forcing of resonant modes on a fringing reef during tropical storm Man-Yi, *Geophys. Res. Lett*., 36(L03607).

Reniers A. J. H. M., J. H. MacMahan, E. B. Thornton, and T. P. Stanton (2007), Modeling of very low frequency motions during RIPEX, *J. Geophys. Res.*, 112, C07013, doi:10.1029/2005JC003122.

Roeber, V., K.F. Cheung, (2012). Boussinesq-type model for energetic breaking waves and its application to fringing reef environment. *Coast. Eng*., accepted.

Ruessink B. G. (1998), The temporal and spatial variability of infragravity energy in a barred nearshore zone. *Cont. Shelf Res*., 18, 585–605.

Ruggiero P., R.A. Holman, and R.A. Beach (2004), Wave run-up on a high-energy dissipative beach, *J. Geophys. Res*., 109(C06025).

Schaffer H. A., (1993), Infragravity waves induced by short-wave groups, *J. Fluid Mech*., 247, 551–588.

Sheremet A., J. M Kaihatu S. -F. Su, E. R. Smith and J. M. Smith (2011), Modeling of nonlinear wave propagation over fringing reefs. *Coast. Eng.*, 58(12), 1125-1137, doi:0.1016/j.coastaleng.2011.06.007.

Smith, J.A. and J.L. Largier, (1995), Observations of nearshore circulation: rip currents, *J. Geophys. Res.*, 100, 10967-10975.

Thomson J. , S. Elgar, B. Raubenheimer, T. H. C. Herbers, and R. T. Guza (2006), Tidal modulation of infragravity waves via nonlinear energy losses in the surfzone, *Geophys. Res. Lett.*, 33(L05601).

Vetter O. J., J. M. Becker, M. A. Merrifield, A. C. Péquignet, J. Aucan, S. J. Boc, C. E. Pollock (2010), Wave setup over a pacific island fringing reef. *J . Geophys. Res*., 115, C12066, doi:10.1029/2010JC006455.

Webb, S. C., X. Zhang, and W. Crawford (1991), Infragravity Waves in the Deep Ocean, *J. Geophys. Res*., 96(C2), 2723–2736, doi:10.1029/90JC02212.

Young I. R., (1989), Wave transformations on coral reefs, *J. Geophys. Res*. 94(C7), 9779-9789.

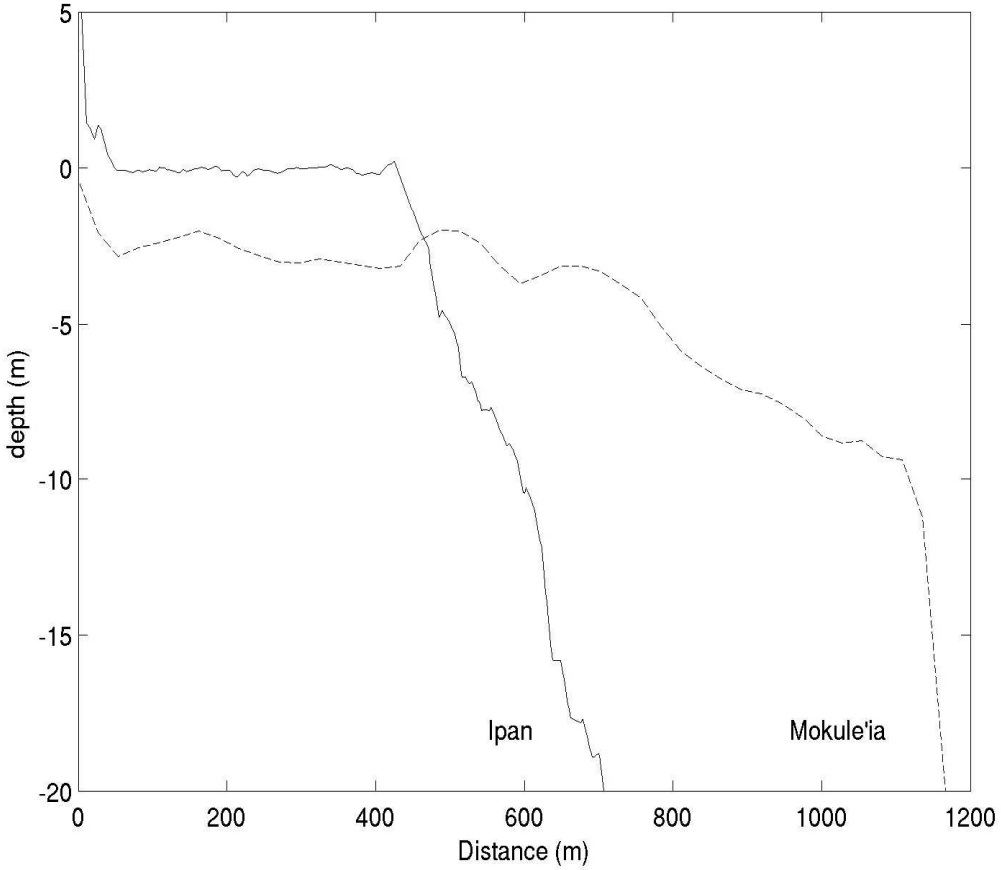

Figure 5.1: Cross-shore reef topography for Ipan, Guam and Mokulei'a, Hawaii.

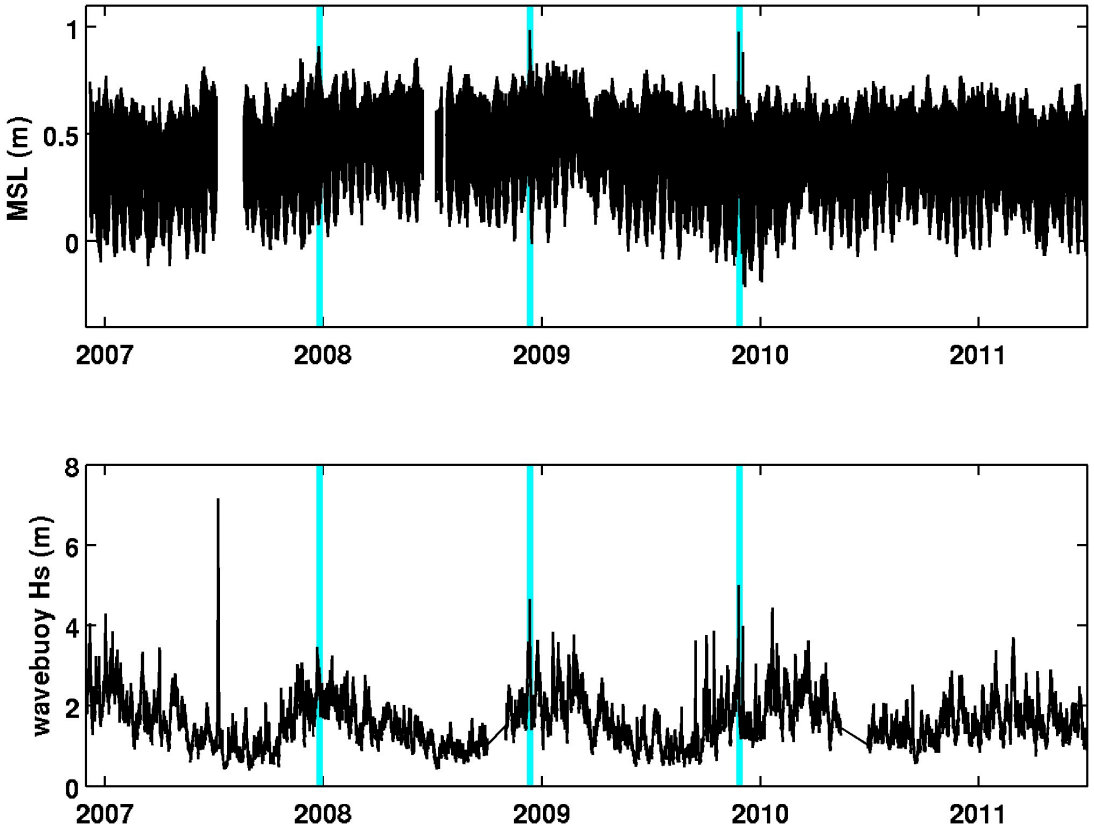

Figure 5.2: Mean sea level at Pago Bay and significant wave height at the Ipan wave buoy. Highlighted in cyan are events when the largest sea levels observed in Pago Bay correspond to peaks in wave height at the buoy.